Achievement of High Resolution Nuclear Study Using a Magnetic Spectrograph System

Yoshitaka Fujita

Research Center for Nuclear Physics, Osaka University

Ibaraki, Osaka 567, JAPAN

CONTENTS

Chapter 1

General Introduction

High resolution spectrographs have made a great progress in the last decade in their size, large acceptance angle as well as in their high resolving power. In order to perform a high resolution experiment using a spectrograph many problems should be settled. Of course most basic one is the stable operation of hardware systems which includes magnet systems, power supplies for them, scattering chamber system, vacuum system, cooling system, control system and so on. Following these is the establishment of operational parameters of the spectrograph and also the data taking systems including focal plane counter systems. These problems may be called "problems of software".

At the Research Center for Nuclear Physics, Osaka University, an AVF cyclotron[1-1] has been constructed and provides beams of protons ($\leq$70 MeV), deuterons ($\leq$60 MeV), alpha particles ($\leq$120 MeV), ^{3}He ions ($\leq$150 MeV) and some light ions ($\leq 120\ Z^2/A$ MeV) with energy stabilities of around 10 . Since this machine was expected to be capable of producing rather large beam current, it was considered feasible to obtain a beam resolution of around 10^4 for moderate intensities of the beams at the target of G course in the W experimental area[1-2] (see Fig. (1-1)). To match this advanced cyclotron and the beam line system, a hybrid type high resolution spectrograph named "RAIDEN"[1-3] has

been constructed and the basic layout is given in Fig. 1-2. It is designed to have a resolution of $p/\Delta p = 2\times10^4$ and the solid angle of $\geq$10 msr and a large momentum dispersion of 27 m. In order to fully use these properties of the spectrograph the "problems of software" become quite important.

First problem, that is, the determination of the operational condition is strongly connected with the correction of the kinematic broadening effect. As is well known the outgoing energy of the reaction products decreases as the scattering angle increases and the amount of decrease is dependent on the kind of reaction as well as on the mean scattering angle. Since a particle with less energy has a smaller turning radius in a magnetic field, the difference of the outgoing energy is directly connected with the difference of the focussing condition and this effect is large in a spectrograph with a large acceptance angle and a large dispersion. The compensation of the focussing properties for the different kinematic conditions of the reaction, therefore, is a quite serious problem for the achievement of high resolution in the operation of a spectrograph.

Another important problem is connected with the choice of the data taking system including the construction of a focal plane counter. Usually a high resolution spectrograph has a large dispersion and an inclined focal line and that is the case for "RAIDEN" also. Associated with the large dispersion is a long focal line of 1.8 m in length and the

inclined incidence angle of 55 degrees to the normal. The focal plane counter system should have a length of at least more than one meter and the gas counter is very popular for such a long counter. In this case, important is the property that it should have a good position resolution even for the non-normal incidence of the particles in the region near to the minimum ionization, because the energy loss of a lightly ionizing particle fluctuates along the particle trajectory in the counter, which will deteriorate the position resolution. Enduring the high counting rate of incident particles and the background due to the high energy, large intensity beam is also important for the counter to work well. In spite of these requirements, the associated electronic circuits and the data acquisition should not be too complicated. These everything should be settled for the efficient use of the spectrograph.

In this parper for the better use of the spectrograph the answers, though it may not be complete, are presented to the above problems. In Chapter 2, the importance of the kinematic correction is discussed and the determination procedure of the operational parameters for the spectrograph "RAIDEN" and the obtained results are presented. In Chapter 3, a new type of focal plane counter system developed for a hybrid-type, high resolution spectrograph is described. In spite of the simplicity of the system, the data acquisition system is powerful enough at present. Chapter 4 treats some of the experimental results using the determined operational

parameters and the counter system. One is about the new collective excitation found in ^{90}Zr and the other is about the spin flip single particle excitation found in ^{48}Ca. The high resolution experiments were indispensable to obtain the good results in both experiments.

References

1-1 M. Kondo, I. Miura, T. Yamazaki, H. Ejiri, A. Shimizu, M. Inoue, K. Hosono, T. Saito, Y. Nagai, H. Sakai, N. Matsuoka and S. Yamabe, Proc. Int. Conf. on Cyclotrons and their Applications, Zürich, 1975, ed. W. Joho (Birkhäuser Verlag, Basel and Stuttgart, 1975) p. 95.

1-2 H. Ikegami, I. Katayama, M. Fujiwara, S. Morinobu, Y. Fujita and H. Ogata, Annual Report of RCNP, Osaka Univ. (1976) p. 76.

1-3 H. Ikegami, S. Morinobu, I. Katayama, M. Fujiwara and S. Yamabe, Nucl. Instr. and Meth. 175 (1980) 335.

Figure captions

Fig. 1-1. Facilities at RCNP.

Fig. 1-2. The basic layout of the spectrograph "RAIDEN".

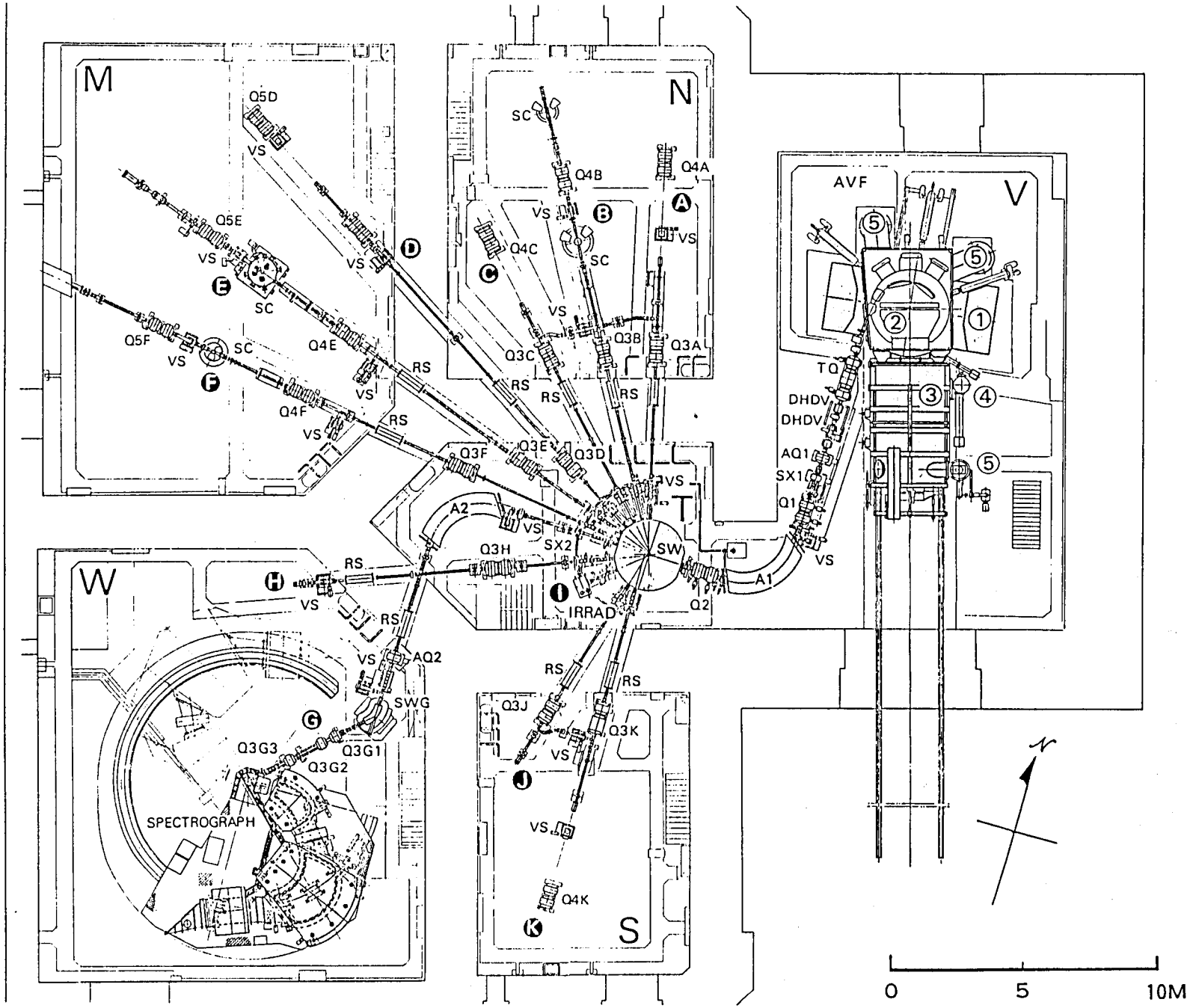
M
N
V
W
S
T
AVF
Q5D
Q5E
Q5F
Q4E
Q4F
Q4B
Q4A
Q4C
Q3B
Q3A
Q3C
Q3F
Q3E
Q3D
A2
Q3H
SX2
SW
A1
Q2
IRRAD
AQ2
SWG
Q3G3
Q3G2
Q3G1
SPECTROGRAPH
Q3J
Q3K
Q4K
TQ
DHDV
DHDV
AQ1
SX1
Q1
SC
VS
RS
A
B
C
D
E
F
G
H
I
J
K
1
2
3
4
5
N
0
5
10M

Fig. 1-1.

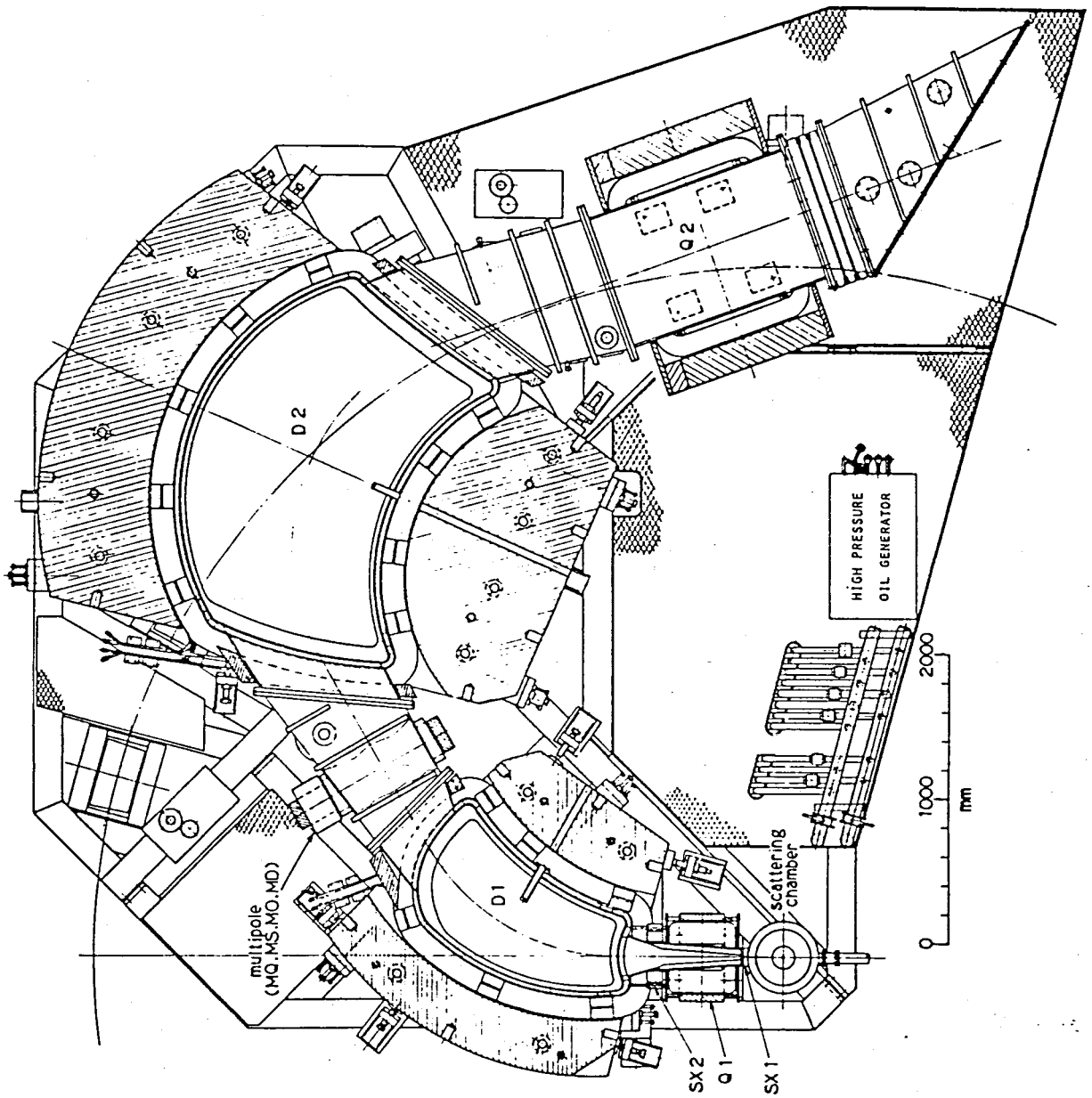
Q2
D2
HIGH PRESSURE
OIL GENERATOR
D1
multipole
(MQ.MS.MO.MD)
scattering
chamber
SX2
Q1
SX1
0
1000
2000
mm

Fig. 1-2.

Chapter 2

Experimental Ray Tracing for Kinematical Correction

1. Introduction

2. Kinematic effect and ion optical properties of a spectrograph

   2-1. Ion optical considerations

   2-2. Ion optics including kinematic effect

   2-3. Dynamic correction of the kinematic effect

3. Brief description of the spectrograph

4. Experimental ray tracing

   4-1. Outline of the procedure and the instrumentation

   4-2. Determination of focal line

   4-3. Experimental condition and the obtained data

   4-4. Search for best parameter

   4-5. Validity check of the parameter at various values of K_1

   4-6. Aberration in the vertical direction

5. Summary and discussion

Chapter 2

Kinematic Correction by Experimental Ray Tracing

Abstract

Magnetic spectrographs for the analysis of nuclear reaction particles can have a large solid angle as well as high resolution. To achieve these properties, it is necessary to correct the kinematic energy broadening caused by the difference of the outgoing energy of the particles depending on the scattered angle in the reaction. In this chapter the importance of the kinematic effect is discussed and the kinematic compensation procedure performed for the spectrograph "RAIDEN" using a multipole magnet is presented. The importance of the vertical kinematic aberration caused by the large acceptance angle in vertical direction is also argued. Although this effect is proportional to the second order in vertical acceptance angle, it can have fairly large influence on the resolution.

1. Introduction

Among the nuclear particle detectors, magnetic spectrographs have been used preferentially because of their high resolution, large solid angle and the possibility of achieving low background. The former two advantages over solid state detectors can mainly achieved by the capability of the spectrographs to correct the kinematic effects[2-1,2]. The kinematic line broadening of the image is caused by the energy difference depending on the scattering angle and can be serious for a spectrograph with a large dispersion and a large solid angle. This effect can be eliminated in the first order by two kinds of correction methods. One is by shifting the position of the focal plane detector system[2-1] and the other by controlling the focussing property of the spectrograph through some kind of corrective elements without change of the position of the detector system[2-2].

Recent development of new generation magnetic spectrographs is outstanding especially in those of hybrid-type[2-3], which consist of several dipole magnets and several quadrupole magnets. In these magnetic spectrographs large dispersion of as large as 20 cm/% is achieved. As a consequence, in the former way of kinematic correction an extremely large shift of the detector position of as large as several meters is expected among different reactions. Because of a large and sophisticated focal plane counter system which is hard to be moved with precise reliability, this way of kinematic correction is not practical any more. Besides this since

the vertical focussing point does not change its position, stigmatic focussing condition can not be achieved and a large vertical tolerence is required for the position counter system.

Kinematic correction by corrective elements became available with the development of high performance multipole magnet. This way of kinematic correction seems to be much easier and more reliable than the other, for the correction can be performed only by controlling the current strength of the magnet. Higher order aberrations which can not be compensated by the shift of the detector position can also be minimized by controlling higher order multipole component in addition to the quadrupole component of the multipole magnet. This way of kinematic correction by a multipole magnet in a spectrograph was first proposed by Enge, Kowalski, et al.[2-4 7] and corrections by other kind of field corrective elements are found in refs. 2-8 and 2-9. For the RCNP spectrograph "RAIDEN"[2-10,11], so called "current-sheet type" multipole magnet[2-12] is installed near the intermediate vertical cross-over point of the trajectories in the spectrograph. It can produce multipole fields of various order from quadrupole upto decapole and showing its power for the kinematic correction.

In the real operation up to now, the strength of the multipole element, mainly the strength of the quadrupole, have been adjusted empirically to minimize the line width of the image at the focal line depending on the kinematic

condition of the reaction[2-7]. This way of adjustment, however, was afraid to introduce the ambiguities caused by the finite target thickness, beam line energy resolution, finite beam spot size and so on. In addition best operational parameters for the higher order multipole components were far from being obtainable. In order to know the properties more precisely it was throught to be necessary to trace rays scattered to various directions in horizontal (θ) as well as vertical (ϕ) direction under various excitation strengths of the multipole elements. Experimental ray tracings up to now have been performed using α-particles from α-sources and more recently, to investigate the properties of a spectrograph at the region of larger magnetic rigidity, Cs ions accelerated with a voltage of around 40 keV[2-13]. Although these methods are convenient and useful for knowing the static properties of a spectrograph without kinematic broadening, they are no more effective for the investigation of more dynamic properties related to kinematic effects.

To overcome these difficulties, we decided to perform experimental ray tracing using elastically scattered beams from the cyclotron at some proper scattering angles. This way of investigation may seem to be far more time consuming, it is inevitable to know suitable strengths up to higher order multipole fields according to the change of the kinematic characteristics of the reaction products.

In this chapter, the experimental correction procedure of the kinematic effct using the multipole magnet is described for the case of spectrograph "RAIDEN". In Section 2, the importance of the kinematic effect in nuclear reaction study is summarized and short review of ion optical properties of the spectrograph is given in Section 3. In Section 4, the experimental procedure for the kinematic correction and the achieved performance is presented.

2. Kinematic effect and ion optical properties of a spectrograph

2-1. Ion optical considerations

Within the median plane, the deviation x_f and inclination angle θ_f of any ion trajectory from a reference central-trajectory can be expressed by a Taylor expansion in five initial values x, y, θ, ϕ and δ. Where x and y indicate the deviations of the object point, θ and ϕ the inclination angle of the trajectory with respect to the x- and y-axes, respectively and δ is the fractional momentum difference of a particle. For simplicity, assuming that the system is symmetric about the median plane, the deviation x_f may be written as:

$$\begin{aligned} x_f = {} & (x|x)x + (x|\theta)\theta + (x|\delta)\delta \\ & + (x|x^2)x^2 + (x|x\theta)x\theta + (x|x\delta)x\delta \\ & + (x|\theta^2)\theta^2 + (x|\theta\delta)\theta\delta + (x|\delta^2)\delta^2 \\ & + (x|y^2)y^2 + (x|y\phi)y\phi + (x|\phi^2)\phi^2 \\ & + \text{third and higher order terms.} \end{aligned} \qquad (2\text{-}1)$$

Similar expression is valid for the θ_f. Here the parentheses are symbols denoting the Taylor coefficients and called transfer coefficients. Because of the assumed symmetry about the median plane, no odd order terms in y and/or ϕ will appear in the expression. The first-order focussing point is defined as the place where the $(x|\theta) = 0$ is achieved. The term $(x|x)$ represents the magnification M_x of the system and $(x|\delta)$ is

the dispersion D which measures the displacement in the x-direction at the focussing point per unit change in δ.

Let us proceed to the second and higher order terms. As the deviations x and y are usually small, important aberration comes from the terms $(x|\theta^2)$, $(x|\phi^2)$, $(x|\theta^3)$, $(x|\theta\phi^2)$, ..., because they obscure the image. The term $(x|\theta\delta)$ is related with the inclination angle Ψ of the focal line by the relation

$$\tan\Psi = -\frac{D}{(x|\theta\delta)(x|x)} \quad . \tag{2-2}$$

As can be expected from the analogy, the term of the form $(x|\theta\delta^n)$ has a relation with the n-th order curvature of the focal line as well as those of $(x|\delta^n)$. The radius of the focal line, for example, may be expressed using $(x|\theta\delta^2)$ and other coefficients as,

$$R = \frac{(\dot{S}_\theta^{\,2}+\dot{X}_\theta^{\,2})^{3/2}}{\dot{S}_\theta\ddot{X}_\theta-\ddot{S}_\theta\dot{X}_\theta} \quad , \tag{2-3}$$

where

$$\dot{S}_\theta = -\frac{1}{(\theta|\theta)}(x|\theta\delta) = -(x|x)(x|\theta\delta) = -M_x(x|\theta\delta) \ ,$$
$$\ddot{S}_\theta = -2M_x\{(x|\theta\delta^2) + (\theta|\theta\delta)\dot{S}_\theta\} \ ,$$
$$\dot{X}_\theta = (x|\delta) = D,$$
$$\ddot{X}_\theta = 2\{(x|\delta^2) + (\theta|\delta)\dot{S}_\theta\} \ .$$

2-2. Ion optics including kinematic effect

When the spectrograph is used to detect nuclear reaction products, the momenta of particles change as a function of reaction angle Θ and ϕ (see Fig. 2-1). The momentum p of an arbitrary ray scattered around the mean reaction angle Θ_0 (often denoted as θ_{lab}) may be expanded as a Taylor expansion in terms of $\theta = \Theta - \Theta_0$, ϕ and δ as

$$\begin{aligned} p(\theta,\phi,\delta) &= p_0\Big(1 + \delta + \frac{1}{p_0}\Big[\frac{\partial p}{\partial \Theta}\Big]_{\Theta=\Theta_0}\theta + \frac{1}{2p_0}\Big[\frac{\partial^2 p}{\partial \Theta^2}\Big]_{\Theta=\Theta_0}\theta^2 \\ &\quad + \frac{1}{2p_0}\Big[\frac{\partial^2 p}{\partial \phi^2}\Big]_{\Theta=\Theta_0}\phi^2 + \frac{1}{p_0}\Big[\frac{\partial^2 p}{\partial \Theta\,\partial \delta}\Big]_{\Theta=\Theta_0}\theta\delta + \cdots\Big) \\ &= p_0(1+\delta+K_1\theta+K_2^{\theta}\theta^2+K_2^{\phi}\phi^2+K_2^{\theta\delta}\theta\delta+\cdots). \end{aligned} \tag{2-4}$$

The kinematic parameters K_1, K_2^{θ}, K_2^{ϕ} and $K_2^{\theta\delta}$ are determined by the masses of the reacting particles, the mean reaction angle Θ_0, and the Q-value of the reaction.

With the kinematic effect included, momentum difference δ should be replaced by

$$\delta \rightarrow \delta+K_1\theta+K_2^{\theta}\theta^2+K_2^{\phi}\phi^2+K_2^{\theta\delta}\theta\delta+\cdots . \tag{2-5}$$

Substituting eq.(2-5) into (2-1) we obtain

$$\begin{aligned} x_f = {} & (x|x)x+(x|\theta)\theta+(x|\delta)(\delta+K_1\theta+K_2^{\theta}\theta^2+K_2^{\phi}\phi^2+K_2^{\theta\delta}\theta\delta+\cdots) \\ & +(x|x^2)x^2+(x|x\theta)x\theta+(x|x\delta)x(\delta+K_1\theta+K_2^{\theta}\theta^2+K_2^{\phi}\phi^2+K_2^{\theta\delta}\theta\delta+\cdots) \\ & +(x|\theta^2)\theta^2+(x|\theta\delta)\theta(\delta+K_1\theta+K_2^{\theta}\theta^2+K_2^{\phi}\phi^2+K_2^{\theta\delta}\theta\delta+\cdots) \\ & +(x|\delta^2)(\delta+K_1\theta+K_2^{\theta}\theta^2+K_2^{\phi}\phi^2+K_2^{\theta\delta}\theta\delta+\cdots)^2 \\ & +(x|y^2)y^2+(x|y\theta)y\theta+(x|\phi^2)\phi^2 \\ & +\text{third and higher order terms.} \end{aligned}$$

$$
\begin{aligned}
= {} & (x|x)x+\{(x|\theta)+(x|\delta)K_1\}\theta+(x|\delta)\delta \\
& +(x|x^2)x^2+\{(x|x\theta)+(x|x\delta)K_1\}x\theta+(x|x\delta)x\delta \\
& +\{(x|\theta^2)+(x|\theta\delta)K_1+(x|\delta^2)K_1^2+(x|\delta)K_2^{\theta}\}\theta^2 \\
& +\{(x|\theta\delta)+2(x|\delta^2)K_1+(x|\delta)K_2^{\theta\delta}\}\theta\delta \\
& +(x|\delta^2)\delta^2 \\
& +(x|y^2)y^2+(x|y\phi)y\phi+\{(x|\phi^2)+(x|\delta)K_2^{\phi}\}\phi^2 \\
& +\text{third and higher order terms.} \qquad (2\text{-}6)
\end{aligned}
$$

As is clear from eq.(2-6), the first order focussing is achieved at the shifted point satisfying the condition

$$(x|\theta) + (x|\delta)K_1 = 0 \quad ,$$

or

$$(x|\theta) + DK_1 = 0 \quad . \qquad (2\text{-}7)$$

The shift of the focal line, therefore, is large in a spectrograph with large dispersion. For a spectrograph with a dispersion of 20 cm/%, this shift amounts to -120 cm for a reaction with $K_1 = -0.1$*1) compared with the case of $K_1 = 0$. Here it should be noted that vertical focussing condition $(y|\phi) = 0$ is not affected by the kinematic effect. Therefore the stigmatic condition of a spectrograph is far from being achieved at this first order horizontal focussing position.

Proceeding to the higher order terms in eq. (2-6), we note that the value of important aberration term concerning

---

*1) For example, the reaction $^{12}C(\alpha,\alpha_0)$, $E_\alpha = 70$ MeV, Θ_0 $(= \theta_{lab}) = 16°$ has the K_1 value of around -0.1.

to θ^2 changes according to the change of kinematic factors. In addition, since the coefficients for $\theta\delta^n$ change, the inclination angle and also the curvature of the focal line change by the kinematic effect.

Another important aberration comes form the term $(x|\delta)K_2^{\phi}\phi^2$. Here K_2^{ϕ} is known to be expressed [2-14] by

$$K_2^{\phi} = \frac{1}{2}K_1 \cot\Theta_0 \,. \qquad (2\text{-}8)$$

Since fairly large acceptance angle in ϕ direction is usually desired, this aberration can sometimes become a serious problem in a reaction with large K_1 value in a condition that large aberrations in θ derection are compensated.

2-3. Dynamic correction of the kinematic effect

From the above discussions, it is clear that the kinematic correction by means of a displacement of the counter position is far from being a solution for the correction of kinematic effect especially in the case of spectrographs with large dispersion.

Noting the fact that main part of the kinematic effect is strongly related with the transfer coefficients about θ, it is natural to think of putting some corrective element near the vertical focussing point, where the beam in vertical direction is narrow and vertical ion optical properties are less affected by the corrective element. The corrective element should generate quadrupole field for

compensating first order shift of the focussing position. Comparing the eqs. (2-1) and (2-6), it is necessary to employ sextupole field besides the quadrupole one to keep the inclination angle of the focal line unchanged and also to reduce the quadratic aberration in θ. The curvature of the focal line and the higher order aberrations in θ can be corrected by higher order components of the multipole field.

To illustrate the importance of the compensation, by means of a multipole field let us see the numerically calculated results*2) for the case of spectrograph "RAIDEN"(2-10). In Fig. 2-2, the inclination angle is plotted as a function of kinematic factor K_1. It is clear that the inclusion of higher order components, in addition to the MQ (quadrupole component of the multipole) is effective to keep the inclination angle Ψ of the focal line unchanged. Another important example is shown in Fig. 2-3, where the minimized kinematic broadenings are shown for the several cases sequentially adding higher order components of the multipole field. Though the MQ component reduced the kinematic effect nearly one order compared with the case of no-correction, MS (sextupole component of the multipole field), MO (octupole component of the multipole field) and also MD (decapole component of the multipole field) were found to be necessary for the complete compensation of the kinematic effect.

---

*2) The calculation was performed using a computer code RAYTRACE(2-15).

3. Brief description of the spectrograph

Although a general description of the QDMDQ magnetic spectrograph for nuclear reaction studies has been given in detail in refs. 2-10,11, we wish to review here only the ion optical aspects and the properties of the multipole magnet briefly.

The first-order parameters have been so determined as to achieve a resolution of $p/\Delta p > 2\times10^4$ for a source width of 1 mm, a momentum dispersion along the focal line to be about 27 cm/%, and a maximum solid angle of larger than 10 msr. The ion optical geometry thus determined is shown in Fig. 2-4 and the calculated beam profile in the spectrograph is shown in Fig. 2-5. The first-order properties are summarized in Table 2-1.

The spectrograph now consists of two dipole magnets, two quadrupole magnets, a multipole magnet and a sextupole magnets. Originally another sextupole was installed just behind the scattering chamber. This magnet, however, had to be removed to make space for the precision slit system to be installed. The first quadrupole magnet (Q1) is used with the horizontally defocussing mode. With this quadrupole Q1, virtually small image of the beam spot size is achieved for the horizontal direction. In addition a broader beam profile within the median plane in the following dipole fields is expected, which is known to increase the dispersion of the spectrograph. Both of these functions contribute largely to increase the first order momentum resolving power

defined by

$$R_p = D/\{2(x|x)x\}. \quad (2\text{-}9)$$

The quadrupole also has an auxiliary function to increase the acceptance angle in the vertical direction.

Two dipole magnets (D1 and D2) placed behind the first quadrupole Q1 act as dispersive elements. The main purpose of the separation of the dispersive element into two pieces is to provide dynamical kinematic focussing by placing a multipole magnet at the intermediate vertical focussing point (see Fig. 2-5). The pole boundaries of the dipole D1, D2 are shaped so as to minimize the aberrations. Pole boundaries nearest to the intermediate vertical focussing point are suited for the correction of the aberrations relevant to θ, while the pole boundaries away from the intermediate image are effective for the correction of the aberrations relating to ϕ.

Last quadrupole magnet (Q2) is used for the adjustment of the location of the vertical focussing point as well as the horizontal one. In our case, this quadrupole Q2 is used with a defocussing mode and the value of the dispersion $(x|\delta)$ is magnified to match the focal plane particle detectors. It also achieves a smaller vertical magnification, which is also important for the actual use of the spectrograph.

In additon to the above elements, a sextupole magnet (SX2) and a multipole magnet (MP) are installed for the correction of the aberrations. The sextupole SX2 is used for the reduction of the second order aberrations especially

relevant to ϕ, which are known to be difficult to be minimized by any change of the curvatures of the dipole magnets. The multipole magent is installed at the intermediate vertical focussing point between the two dipole D1, D2. As explained in the previous section, this location is suited for the dynamic control of the kinematic correction because the ion optical properties concerning to θ are selectively compensated without largely disturbing the vertical focussing properties. It should be noted that the aberrations caused in the process of manufacturing and assembling the spectrograph and those from possible irregularities of the field distribution of the magnets may also be compensated with this multipole magnet.

The multipole magnet can produce various multipole fields, i.e., quadrupole (MQ), sextupole (MS), octupole (MO) and decapole (MD) independently by exciting separately wound coils for each field. As the measured distribution (see Fig. 2-6) for each component shows, fairly ideal multipole field was found to be realized for the entire aperture of the magnet. The other important aspect of the magnet, i.e., excitation function was also measured and as a result, good linear response was observed in the usually used excitation range[2-10~12]. These features of the multipole magnet largely simplify the procedure of the kinematic correction, since the compensation can be performed fairly separately for the successive order of aberrations without regard to the excitation strength of the magnetic field.

4. Experimental ray tracing

4-1. Outline of the procedure and the instrumentation

The Figure 2-1 shows the fundamental geometrical values appearing in the ray tracing. The final goal is to minimize the value $\Delta X(\theta,\phi)$ which is defined as difference of the arrival position X along the focal line between an arbitrary ray scattered in θ and ϕ direction from a target placed at the object point and the reference ray scattered in $\theta = 0$ and $\phi = 0$ direction. To assure the broad range of the spectrograph, it is necessary that ΔX should be small on the determined focal line irrespective of the value of the mean orbital radius ρ which is defined as the magnetic rigidity of a particle divided by the strength of main dipole magnet B_D. As was mentioned, in the case of spectrograph "RAIDEN", the ion optical properties can be adjusted using the auxiliary magnets. The best focussing condition should be searched by adjusting the strengths of these magnetic fields.

The focussing condition largely depends on the value of the kinematic factor K's, especially on the first order factor K_1 which is determined by the masses of the reaction particles, Q-value and also by the mean scattering angle Θ_0. The best operating conditions of the auxiliary magnets, therefore, should be searched at several different kinematic conditions.

To perform the ray tracing, it is necessary to collimate the scattered beam corresponding to the desired direction of the acceptance angle in θ-ϕ plane. In our case mesh points with width of 5 mr and height of 10 mr was defined as shown in Fig. 2-7. For the definition of the beam direction, a

slit system shown in Fig. 2-8 was installed just after the scattering chamber. Each mesh point can be selected by adjusting the positions of the four jaws (left-right and upper-lower pairs) of the slit system by pulse motors. The position of a jaw is supposed to be reproduced with a precision of less than 0.025 mm ($\sim$0.1 mrad) for the whole range of 40 mm movement.

The rays defined by the slit were detected with a 1 m long induction wire position sensitive counter system, which is supposed to have a resolution of less than 1 mm. For the measurement of some of the vertical properties of the spectrograph, a 1.5 m long two dimensional position counter system was used. In both of the counter systems, the position of the ray was determined by the charge division method using a computer software and peak position (centroid) was directly displayed on a graphic terminal. Detailed description about the counter system can be found in Chapter 3.

4-2. Determination of focal line

Before going into the ray tracing, the position of the focal plane was decided experimentally. As was explained in Section 3, the position of the focal line can be adjusted by means of MQ and also by Q2 magnet. In all the measurements performed, however, Q2 strength relative to the strength of two dipole magnets was set to the value at which the ray trace calculation[2-10] predicted the best performance and

the correction for the position of the focal plane was performed by adjusting the strength of MQ magnet. The strengh of Q1 was also set at the calculated value.

It is expected that at the focussing point, first order focussing condition,

$$\left.\frac{\partial X(\theta,\phi)}{\partial\theta}\right|_{\theta=0}=0 \ , \qquad (2\text{-}10)$$

is satisfied. This means that little change of beam arrival position X is expected along the focal line irrespective of the small change of the inclination angle θ of emitted particles from the target at the angles around $\theta = 0$ ($\Theta = \theta_0$). The focal line can then be decided by tracing these focussing points at different value of ρ (or for particles with various δ-values). In the present way of using elastically scattered particles, focal line can be determined by tracing the points where first order focussing is performed with the same MQ strength normalized by the strength of dipole magnet (B_D) when B_D value is adjusted to simulate the various ρ values (see Fig. 2-9).

A 1 m long positon counter was placed at the expected "normal" position of the focal line in the first place. The protons elastically scattered from ^{50}Cr target at E_p = 65 MeV, Θ_0 (= θ_{lab}) = 12° was detected at three positions in the counter corresponding to ρ = 148 cm (ρ_{in}), 150 cm (ρ_{center}) and 152 cm (ρ_{out}). At each location of the counter, optimum strength of MQ was searched to satisfy the

first order focussing condition. Then the counter system was displaced 50 mm downstream from the "normal" position (see Fig. 2-9) and same measurement was performed. Using the difference of the optimum values of MQ strength at two positions, the points which are expected to give the same normalized optimum MQ value as that at the "normal", ρ_{center} point (F_c) were interporated along the beam trajectory at ρ_{in} and ρ_{out} (F_i and F_o). By tracing these three points, optimum value of the inclination angle of the focal line Ψ was decided to be 35.3 deg. This value is slightly smaller but fairly consistent with the value expected by the calculation (36 deg). At this stage, slight indication of curving of the focal line was observed. However, this was expected to be minimized by adjusting the third and higher order ion optical properties by employing the higher order components of the multipole.

4-3. Experimental condition and the obtained results

In an actual search of the best parameters for the auxiliary magnets, efforts were concentrated on the minimization of aberrations about the θ direction, because the aberration appearing from the term $(x|\phi^2)$, the remaining main term, was found to be compensated by taking the data two dimensionally as will be described in Chapter 3.

Three kinds of reactions representing different values of kinematic correction factor K_1 were selected as objects for ion optical search. They are $^{50}Cr(p,p_0)$, $^{27}Al(\alpha,\alpha_0)$ and

$^{12}C(\alpha,\alpha_0)$ and the kinematic properties of the scattered particles are summarized in Table 2-2. Up to now, "RAIDEN" is mainly used for the detection of light ions. The range of K_1 value examined here ($0.0 \geq K_1 \geq -0.1$) is sufficient in most cases.

At each value of K_1, the value ΔX was measured as a function of the strength of the corrective elements MQ, MS, MO, MD and SX2. The inclination angles θ selected were -30, -15, 0, +15 and +30 mr (see Fig. 2-7). In Fig. 2-10, part of the measured results are shown for the case of K_1 = -0.0045. This kind of response functions were measured at ρ = 148 cm (ρ_{in}), 150 cm (ρ_{center}) and 152 cm (ρ_{out}), respectively. As is seen from Fig. 2-10 it seems to be plausible to assume that ΔX changes linearly as a function of the strength of the current. This is consistent with the fact that the measured distributions of the various multipole fields were fairly ideal and the linear response of the field strength to the excitation current was realized in the range of the present measurement. If we make a fairly plausible assumption that each field component of the multipole can be simply superposed without any interference, the relative movement of each ray along the focal line referring to the beam emitted to θ = 0 can be expressed as

$$\Delta X_{\theta=\theta_i} = C_i^{Q}|MQ> + C_i^{S}|MS> + C_i^{O}|MO> + C_i^{D}|MD> + C_i^{SX2}|SX2> + C_i^{const.}, \qquad (2\text{-}11)$$

where $|\cdots>$ and C_i are the excitation strength of each component normalized by the strength of the main dipole magnet B_D and its coefficient, respectively and θ_i represents -30mr, -15 mr, +15 mr and +30 mr.

The procedure was repeated at three aforementioned point of the K_1 values to know the K_1-dependence of the ion optical properties. The measured coefficients are tabulated in Table 2-3 for each measured case.

4-4. Search for best parameter

Using the determined linear response function (eq. 2-11) expressing the movement of a ray as a function of strength of various multipole fields, the best configuration of the strengths of the multipole fields was searched at $K_1 = -0.0045$ and $K_1 = -0.0940$ by minimizing the function expressing the amount of aberration;

$$F = [\sum_{\theta}(\Delta X_\theta)^2]_{\rho=in} + [\sum_{\theta}(\Delta X_\theta)^2]_{\rho=center} + [\sum(\Delta X_\theta)^2]_{\rho=out} \quad (2\text{-}12)$$

As shown in Fig. 2-11a for the case of $K_1 = -0.0045$, excitation of MQ strength was expected to achieve the first order focussing and MS strength was expected to minimize the second order aberration as shown in Fig. 2-11b and it is seen that the remaining main term is coming from the third order aberration. By exciting also the MO component, best fit parameter minimizing the aberrations at $\theta = \pm 30$ mr as well as $\theta = \pm 15$ mr was searched and the obtained result is

shown in Fig. 2-11c. Same minimization procedure was performed for the case of K_1 = -0.0940. In all the procedure the strength of SX2 normalized by B_D was always put at a constant value. This is because of the premise that the kinematic correction in θ direction should be performed by the multipole element placed near the intermediate vertical focussing point of the spectrograph. The effect of MD strength was not clear except for the outermost and innermost rays. A small amount of excitation of this field component was found to reduce the aberration of the ray especially at θ = -30 mr, ρ=in, at the K_1 value of -0.0940. The obtained best fit parameters normalized by the strength of main dipole magnet is tabulated in Table 2-4.

Judging from the results of ray trace calculations (see Fig. 2-3b), it seems fairly good to assume that the best set of strengths of the various multipole fields change linearly as a function of K_1 value for the range of present interest. Therefore we put

$$|M_i> = a_i K_1 + b_i \ , \qquad (2\text{-}13)$$

where $|M_i>$ denotes the strength of the i-th multipole field (Q,S,O and D) normalized by the strength B_D of dipole D1 and D2. The constant values a_i and b_i were determined from the results obtained at K_1 = -0.0045 and K_1 = -0.0940 given in Table 2-4 and the values are summarized in Table 2-5.

In order to check whether this interpolation is valid or not, the strengths of multipole fields at K_1 = -0.0340 were calculated from eq. (2-13) and put into the eq. (2-11),

where the coefficients used are those summarized in Table 2-3. The reproduced tendency of the shift ΔX for each ray is shown in Fig. 2-12. The expected aberrations are fairly small for all the cases and the validity of the interporation seems to be assured.

4-5. Validity check of the parameter at various values of K_1

To check experimentally whether the determined parameters for each component of the multipole field were valid or not, the aberrations were measured at several values of K_1. The results of the measurements are shown in Fig. 2-13 for the cases of $K_1 = -0.0072$, $K_1 = -0.0340$, $K_1 = -0.0661$ and $K_1 = -0.0940$ and the properties of reactions used are summarized in Table 2-2. As shown in the figure the determined parameter set was found to give small aberration in the whole range of K_1 value for the $+30 \text{ mr} \geq \theta \geq -30 \text{ mr}$. Here it should be noted that the obtained aberration curve for the same value of ρ (or the same position of the focal line) is quite similar in spite of the large difference of the K_1 value measured here. This fact clearly indicates that in the range of K_1 value ($0 > K_1 > -0.1$) which are of interest in this search, the compensation of the kinematic effect is achieved well by changing every component of the multipole linearly with the K_1 value.

With the presence of these aberrations, the resolution is estimated to be $p/\Delta p \gtrsim 1\times10^4$ (image width 2.5 mm FWHM) for the full acceptance angle of $30 \geq \theta \geq -30$ mr. The

resolution is estimated to increase to more than 2×10^4 (image width 1.2 mm FWHM) by confining the acceptance angle to $15 \geq \theta \geq -15$ mr. This value is comparable or much smaller than the value summing in quadrature the broadening effects associated with finite beam spot size (1.0 $\sim$ 1.5 mm), beam line energy resolution (1.0 $\sim$ 1.8 mm), energy loss straggling effects in the target (>0.3 mm) and so on. In addition, the aberrations inherently associated with large acceptance angle in ϕ direction can not be ignored. Considering these surrounding conditions limitting the obtainable resolution, the results obtained here are fairly satisfactory.

4-6. Aberration in the vertical direction

As was stated in Section 2-2, effective increase of the scattering angle according to the increase of vertical scattering angle ϕ decreases the energy of the emitted particle which causes the aberration proportional to ϕ^2 and the associated coefficients K_2^{ϕ} is given by eq.(2-8). To see the expected effects, the relative arrival position ΔX of a beam scattered in various ϕ direction was measured for the cases of $^{50}Cr(p,p_0)$, E_p = 65 MeV, Θ_0 = 12°, $^{27}Al(\alpha,\alpha_0)$, E_α = 70 MeV, Θ_0 = 13° and $^{12}C(\alpha,\alpha_0)$, E_α = 70 MeV, Θ_0 = 16°. The results are shown in Fig. 2-14. As can be clearly seen, the aberration increases as the K_1 value of the reaction increases. It is of interest to see whether the observed value of aberration is explained in terms of the K_2^{ϕ} given in eq.(2-8). Simple kinematic calculation was performed to

obtain the amount of aberration according to the increase of vertical scattering angle ϕ. Obtained results are converted into channel numbers and summarized in Table 2-6. The calculated values are quite consistent with the results of experiment.

The kinematic coefficient K_2^{ϕ} which makes this vertical aberration is dependent on the scattering angle Θ_0 as well as the value of K_1. In the original design of the spectrograph, this aberration was supposed to be minimized using SX2 magnet and also the first sextupole magnet (SX1) just behind the scattering chamber. Since SX1 should be removed because of lack of space, the excitation of SX2 alone was afraid to be impossible to correct the aberration completely. Another reason of leaving ion optical control of this aberration is that experimental ion optical search should be performed as a function of Θ_0 as well as K_1 and this two dimensional search requires too much beam time to be performed.

In order to overcome this situation a two dimensional counter is constructed and placed at the focal line. In the presence of non-zero $(y|\phi)$ term, the image looks like a crescent when the aberration proportional to ϕ^2 exists. An example of two dimensional display is shown in Fig. 3-22 in Chapter 3. When the curved image is made straight by a software before projecting on the axis along the focal line, the expected deterioration of resolution caused by the aberration can be minimized. We believe that this way of

compensation of the vertical aberration is most efficient in the present system. More detailed discussions about the correction of the vertical aberration and software are given in Chapter 3, 4-3-2.

5. Summary and discussion

The kinematic broadening effect has shown to be compensated for the range of $0.0 \geq K_1 \geq -0.1$ by properly exciting each component of the multipole field installed at the position of vertical intermediate focussing point. In this region of K_1 value presented here, the broadening effects proportional to K_1^2 or K_2^θ are fairly small and, therefore, changing the strengths of multipole elements as a linear function of K_1 was effective enough for the compensation of the kinematic broadening.

It is of interest to compare the amount of change of the strengths of the multipole elements according to K_1 for the experimentally determined value and the result of calculation. The difference of strengths between $K_1 = 0$ and $K_1 = -0.1$ are calculated in terms of the integrated field strength along the magnet axis of the multipole using the coefficients listed in Table 2-5 to make a direct comparison with the calculated results in ref. 10. The results are tabulated in Table 2-7 together with the results from ref. 10. From the table it is clear that for the case of quadrupole strength fairly good agreement is obtained. On the other hand for the case of sextupole strength, large discrepancy of factor 2.5 is observed.

Sources of the discrepancy are seeked. One of the candidate is the inhomogeneity of magnetic field in the dipole magnets. This is an order of two or three times 10^{-4} [11], which is effective enough as a candidate. Optimum conditions

for the strengths of the multipole components were calculated at $K_1 = 0.0$ and $K_1 = -0.1$ for several field conditions simulating the inhomogeneity. Although the optimum value at each condition changes rather widely, the difference of the optimum values between $K_1 = 0.0$ and $K_1 = -0.1$ are found to be conserved.

Another possible candidate is the asymmetry of the field shape at the fringing field region of the multipole magnet. In the actual setting of the multipole magnet, the shape of the field clamp was forced to be set asymmetry because of lack of space around multipole manget. It has been well known that the geometry of the field clamp affects the strength of the field especially for a magnet with large gap and short axial length, like present case. Analytical calculations of the field distribution were performed for the two geometries of the field clamp assuming two dimensional model and infinite magnetic permeability. As the results shown in Fig. 2-15 indicate, the field integral along the trajectory differs about 40% depending on the geometry. Considering this result and the fact that the asymmetry of the quadrupole field in the x-direction mainly produce the sextupole field, it is found that the discrepancy in the sextupole strength can be ascribed to the asymmetry of the quadrupole strength. It should be noted that with this explanation, a larger amount of compensation by the sextupole element is needed for a larger value of K_1, because a stronger excitation of the quadrupole field is required at this region. This kind of

feature is, of course, true for the case of higher order components.

The aberration proportional to $K_2^{\phi}\phi^2$ makes another important source for the deterioration of resolution. In the present ion optical search, however, this aberration was paid little attention since it would not be compensated by a simple combination of multipole element. For the complete compensation, it is necessary to put a powerful sextupole element at some intermediate horizontal beam waist, which is impossible in the present system. A more practical way to compensate this aberration is to measure the image at the focal line in two dimensions. Since the coefficient $(y|\phi)$ usually has some finite value, the image combined with the aberration proportional to ϕ^2 shows a shape like crescent. The shape can easily be made straight by the software and the influence of this aberration can be minimized.

The present measurements were carried out at a dipole field strength of around 8 kG, corresponding to the proton energy of 65 MeV, E_{α} = 70 MeV and $E_{^3He}$ = 90 MeV. We restricted ourselves to this field strength because detailed field mappings[2-11] of the magnets composing the spectrograph showed small change in the field distribution and little change in ion optical property was expected at least up to about the excitation of 12 kG in main magnet. Actually many high resolution experiments have been performed using the kinematic correction parameter determined here. Some of the results are presented in Chapter 4.

References

2-1 J.E. Spencer and H.A. Enge, Nucl. Instr. and Meth. 49 (1967) 181.

2-2 H. Ikegami, Nucl. Instr. and Meth. 187 (1981) 13; and refs. therein.

2-3 H.A. Enge, Nucl. Instr. and Meth. 162 (1979) 161; and refs. therein; ibid. 187 (1981) 1; and refs. therein.

2-4 H.A. Enge and S.B. Kowalski, Proc. 3rd Conf. on Magnetic technology, Hamburg (1970) p. 366.

2-5 C.A. Wiedner, M. Goldschmidt, D. Rieck, H.A. Enge and S.B. Kowalski, Nucl. Instr. and Meth. 105 (1972) 205.

2-6 A.G. Drentje, H.A. Enge and S.B. Kowalski, Nucl. Instr. and Meth. 122 (1974) 485.

2-7 H.J. Scheerer, H. Vonach, M. Löffler, A.v.d. Decken, M. Goldschmidt, C.A. Wiedner and H.A. Enge, Nucl. Instr. and Meth. 136 (1976) 213.

2-8 A. Abdel-Gawad, A. Hardt, S. Martin, J. Reich, K.L. Brown and K. Halbach, Proc. Int. Conf. on Magnet technology, Rome (1975) p. 45.

2-9 H. Wollnik, Nucl. Instr. and Meth. 103 (1972) 479.

2-10 H. Ikegami, S. Morinobu, I. Katayama, M. Fujiwara and S. Yamabe, Nucl. Instr. and Meth. 175 (1980) 335; H. Ikegami, S. Morinobu, I. Katayama, M. Fujiwara, Y. Fujita and H. Ogata, RCNP Annual Report, (1976) p. 113.

2-11 M. Fujiwara, Thesis, Osaka University (1980), unpublished.

2-12 H. Ikegami, Proc. Int. Conf. on Magnet technology, Bratislava (1977) p. 904; H. Ikegami, T. Takayama, M. Fujiwara, I. Katayama and S. Morinobu, ibid. p. 908.

2-13 M. Löffler, H.J. Scheerer and H. Vonach, Nucl. Instr. and Meth. 111 (1973) 1.

2-14 S. Morinobu, private communication; Nucl. Instr. and Meth. to be submitted.

2-15 H.A. Enge and S.B. Kowalski, Proc. Int. Conf. on Magnet technology, Hamburg (1970) 336.

2-16 K.J. Binns and P.J. Lawrenson, Analysis and computation of electric and magnetic field problems (Pergamon press, Oxford, 1973).

Table 2-1.

Design specification of the spectrograph RAIDEN

Mean orbit radius		150 cm
Deflection angle		160°
Angular range		-20° ∿ +140°
Focal line length		180 cm
Tilt angle of focal line		54°
Maximum field flux density		16 kG
Maximum particle rigidity		24 kGm
Magnification	—— vertical	4.0
	—— horizontal[a)]	1.3
Momentum dispersion[a)]		27000 mm
Momentum range		6.7 %
Momentum resolution[b)]		20400
Acceptance angle	—— horizontal	±45 mr
	—— vertical	±70 mr
Solid angle		13 msr

a) Values are given along the focal line.

b) The particle source width is assumed to be 1.0 mm.

Table 2-2.

Reaction and its kinematic coefficient

Reaction	Energy (MeV)	$\theta_0(=\theta_{lab})$ (deg)	Bρ (kG·cm)	K_1
$^{50}Cr(p,p_0)$	65	12	1184.4	-0.0045
$^{208}Pb(\alpha,\alpha_0)$	70	21.5	1208.8	-0.0072
$^{27}Al(\alpha,\alpha_0)$	70	13	1205.8	-0.0340
$^{16}O(\alpha,\alpha_0)$	70	15	1200.0	-0.0661
$^{12}C(\alpha,\alpha_0)$	70	16	1194.6	-0.0940

Table 2-3. Coefficients for the liner response function

K_1	ρ	θ(mr)	C^Q	C^S	C^O	C^D	C^{SX2}	$C^{con.}$
-0.0045	inner (148 cm)	-30	214.3	-37.7	-19.3	7.1	-5.0	-52.0
		-15	99.0	-10.6	-4.0	0.0	-3.5	-23.5
		+15	-81.0	0.0	1.4	0.0	0.0	14.3
		+30	-133.5	-12.9	6.2	0.0	-2.5	7.5
	center (150 cm)	-30	222.7	-36.4	-19.3	7.3	-13.3	-59.9
		-15	98.9	-9.7	-3.7	0.0	-5.1	-25.4
		+15	-81.3	-1.8	1.6	-1.4	2.1	16.2
		+30	-150.9	-16.1	6.8	2.8	-2.4	-0.4
	outer (152 cm)	-30	259.0	-30.3	-14.9	5.3	-16.0	-67.0
		-15	100.5	-5.8	-2.7	0.0	-5.6	-26.6
		+15	-96.6	-6.4	2.3	0.0	1.6	10.2
		+30	-158.5	-24.8	11.2	2.6	-4.6	-23.1
-0.0340	inner	-30	205.7	-45.7	-26.2	13.9	-6.6	-97.9
		-15	99.8	-14.8	-6.6	1.7	-4.0	-45.9
		+15	-84.7	0.7	2.0	0.0	1.5	35.9
		+30	-148.2	-6.1	2.0	0.0	2.0	73.2
	center	-30	232.1	-38.0	-18.5	7.6	-17.5	-112.5
		-15	105.9	-5.5	-3.2	0.0	7.4	-52.2
		+15	-89.1	2.5	3.4	0.0	0.0	39.7
		+30	-151.8	-13.4	9.3	1.1	0.0	61.9
	outer	-30	248.6	-41.9	-19.6	7.3	-17.7	-116.3
		-15	116.8	-11.1	-4.9	0.8	-8.8	-59.8
		+15	-93.2	-5.2	0.0	0.0	1.5	47.0
		+30	-166.8	-20.3	8.8	0.0	-1.5	-58.5
-0.0940	inner	-30	215.1	-39.4	-20.4	6.5	-9.0	-185.1
		-15	99.6	-11.0	-4.8	-1.7	-5.3	-95.2
		+15	-80.1	-2.0	2.0	0.6	1.9	85.9
		+30	-141.8	-9.5	5.6	1.1	1.6	163.6
	center	-30	236.3	-36.9	-21.5	4.8	-14.7	-213.2
		-15	110.3	-6.9	-5.5	-1.1	7.9	-112.9
		+15	-88.0	0.0	1.8	-2.0	5.3	101.3
		+30	-144.4	-13.3	5.3	0.0	5.3	177.6
	outer	-30	254.7	-31.5	-23.5	3.9	-24.1	-284.3
		-15	115.0	-7.8	-4.9	-0.5	-12.4	-129.3
		+15	-86.7	-5.8	3.1	0.9	3.1	102.2
		+30	-151.3	-26.7	9.6	0.5	3.1	183.8

The conversion factors between the field strength and the shunt voltage were 3.406 G/cm·mV, 3.336×10^{-2} G/cm^2·mV, 7.727×10^{-4} G/cm^3·mV and 1.971×10^{-5} G/cm^4·mV respectively for MQ, MS, MO and MD magnet. The relative shift ΔX to the reference beam emitted to $\theta = 0$ can be known by $\Delta X = C^Q|MQ> + C^S|MS> + C^O|MO> + C^D|MD> + C^{SX2}|SX2> + C^{con.}$.

Table 2-4.

Obtained best fit parameters

for the auxiliary magnets at each K_1 value

K_1	-0.0045	-0.0940
|MQ>	0.183 (mV/kG)	1.074 (mV/kG)
|MS>	-0.889	1.042
|MO>	1.629	1.134
|MD>	——	0.886
|SX2>	-1.347	-1.347

Strengths of the magnets are displayed by means of shunt voltage (mV) of the power supply normalized by the strength B_D(kG) of the main magnet D_1.

Table 2-5.

The K_1 dependence of the strengths of various multipole fields

|···>	a_i	b_i
|MQ>	-9.960 (mV/kG)	0.138 (mV/kG)
|MS>	-21.571	-0.986
|MQ>	5.527	1.654
|MD>	-9.426	0.0
|SX2>	0.0	-1.347

Strengths of the magnets are displayed by means of shunt voltage (mV) of the power supply normalized by the strength B_D(kG) of the main magnet D_1.

Table 2-6.

Calculated and measured vertical aberration at various K_1 values

ϕ(mr)	$\lvert\Delta E\rvert$ (keV)	ΔX (ch)	ΔX measured
$^{50}Cr(p,p_0)$, $\Theta_0 = 12°$, $E_p = 65$ MeV			
0	0.0	0.0	0.0
15	0.3	0.2	0.0
30	1.2	0.7	2.0
45	2.7	1.5	3.0
60	4.8	2.7	4.5
$^{27}Al(\alpha,\alpha_0)$, $\Theta_0 = 13°$, $E_\alpha = 70$ MeV			
0	0.0	0.0	0.0
15	2.2	1.0	0.5
30	9.0	4.3	2.5
45	20.6	9.8	7.0
60	36.6	17.4	11.5
$^{12}C(\alpha,\alpha_0)$, $\Theta_0 = 16°$, $E_\alpha = 70$ MeV			
0	0.0	0.0	0.0
15	4.4	2.1	2.5
30	20.0	9.5	9.0
45	44.6	21.2	20.5
60	78.4	37.3	—

Table 2-7.

Strength difference between $K_1 = 0$ and $K_1 = -0.1$

	experimental (kG·cm)	calculated[1] (kG·cm)
MQ	33.39	26.67
MS	17.71	6.90
MQ	2.63	3.48

1) Value taken from ref. 10.

The strength difference is given in terms of integrated field strength along the axis of the multipole at the position x = 25cm in the multipole element. In the experimental value, the effective length of the field is assumed to be 36.9 cm.

Figure captions

Fig. 2-1. Schematic representation of the fundamental geometrical values appearing in the ray tracing. Abbreviations: O object point of the spectrograph; Θ scattering angle in horizontal direction; Θ_0 mean scattering angle of the particles accepted into the spectrograph; θ inclination angle of the trajectory defined by $\Theta-\Theta_0$; ϕ inclination angle of the trajectory in vertical direction; x horizontal deviation of particle trajectory in reference to the particle with $\theta=\phi=0$; y vertical deviation of particle trajectory; ρ mean radius of particle trajectory in the dipole magnet; X arrival position of a particle along the focal line; ΔX horizontal deviation of arrival position of an arbitrary particle in reference to the particle with $\theta=\phi=0$; Ψ inclination angle of the focal line.

Fig. 2-2. Calculated inclination angle Ψ of the focal line versus kinematic factor. It is seen that the inclusion of higher order multipole field components in addition to the quadrupole field component makes the angle Ψ constant irrespective of the K_1 value.

Fig. 2-3. a) Calculated results for the minimized kinematic line broadenings versus kinematic factor K_1.

Inclusion of higher order components is important for the complete compensation of the kinematic line broadening. b) Optimum field strength of each multipole field component of the multipole element.

Fig. 2-4. Optical geometry of the spectrograph RAIDEN. D1, D2 first and second dipole magent; Q1, Q2 first and second qudrupole magnet; SX1, SX2 first and second sextupole magnet; MP Multipole magnet.

Fig. 2-5. Calculated trajectories of particles in vertical (y) and horizontal (x) direction.

Fig. 2-6. Measured field distribution in the median plane of the multipole element. a) quadrupole and octupole field. b) sextupole and decapole field.

Fig. 2-7. Sub-divisions of the acceptance solid angle used to define the rays with different θ and ϕ.

Fig. 2-8. Front and side view of the defining slit system of the spectrograph installed between the scattering chamber and the Q1 magnet. The acceptance solid angle is defined by four jaws (left and right, upper and lower) made of 5 mm thick tantalum. These jaws are driven independently by pulse

motors, so that the acceptance aperture of the spectrograph may be defined arbitrarily within ±70 mr in the vertical direction and ±40 mr in the horizontal direction.

Fig. 2-9. Determination procedure of the focal line is shown schematically. Position counter was placed at the planned "normal position" and the "shifted position". At each position, the optimum values of MQ was searched for the rays with the mean radius of ρ_{in} (148 cm), ρ_{center} (150 cm) and ρ_{out}(152 cm). At ρ_{in} and ρ_{out}, focussing point was defined by an interpolation (extrapolation) to be the point where optimum value of MQ normalized by the strength of the main magnet B is the same as the value at F_c.

Fig. 2-10. The movement of the beam emitted to θ = -30, -15, 15 and 30 mr relative to the reference beam emitted to θ = 0 mr as a function of the strength of each auxiliary magnet measured for the reaction $^{50}Cr(p,p_0)$, E_p = 65 MeV, K_1 = -0.0045, ρ_{center} (150 cm). The amount of movement ΔX is expressed in channel numbers in the focal plane counter and each channel corresponds to 0.5 mm along the focal line. Here plus sign denotes the movement toward smaller radius. The strength of each

component is expressed in terms of shunt voltage of the power supply and the conversion factors for MQ, MS, MO and MD are 3.406 G/cm·mV, 3.336 × 10^{-2} G/cm^2·mV, 7.727 × 10^{-4} G/cm^3·mV and 1.971 × 10^{-5} G/cm^4·mV respectively. This kind of response was measured at ρ_{in} (148 cm), ρ_{center} (150 cm) and ρ_{out} (152 cm) for the cases K_1 = -0.0045, -0.0340 and -0.0940.

Fig. 2-11. Minimization procedure (calculation) is presented for the case of K_1 = -0.0045. The notation I, C and O denotes the property at ρ_{in}, ρ_{center} and ρ_{out}, respectively. a) first order focussing was adjusted by properly exciting the MQ strength. b) MS strength was also adjusted to compensate the second order aberration and the substantial part of the remaining aberration is of third order. c) the aberration was compensated by the proper combination of the multipole field strength up to octupole.

Fig. 2-12. Calculated aberration ΔX for the case of K_1 = -0.0340 by putting the multipole field strengths $|M_i>$ given by eq.(2-13) and the coefficients C listed in Table 2-3 into eq.(2-11).

Fig. 2-13. Measured aberration at various values of K_1. As

can be seen, the kinematic effect is compensated fairly well for the whole range of K_1 value of interst here.

Fig. 2-14. Arrival position X of the beam was measured for the beams with various values of vertical scattering angle ϕ. Relative movement ΔX to the beam with $\phi = 0$ is plotted. Since this vertical aberration is proportional to $K_1\phi^2$, large quadratic aberration is observed at large K_1 value.

Fig. 2-15. Calculated fringing field distribution under different geometries of the field clamp. The calculation was performed using conformal transformation[2-16] assuming two dimensional model and infinite magnetic permeability.

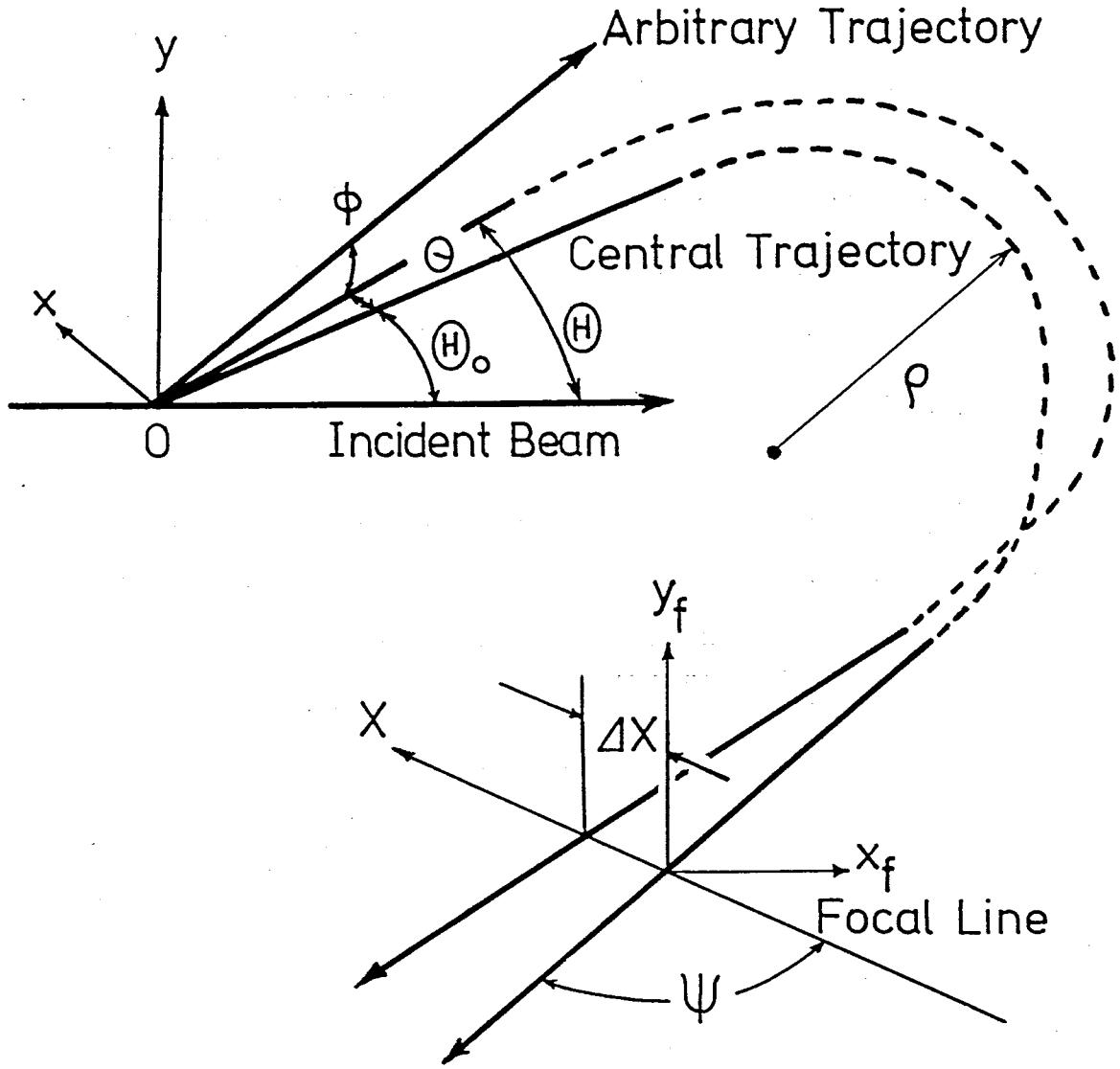
Arbitrary Trajectory
y
Φ
Θ
Central Trajectory
x
Ⓗ₀
Ⓗ
ρ
0
Incident Beam
y_f
X
ΔX
x_f
Focal Line
Ψ

Fig. 2-1.

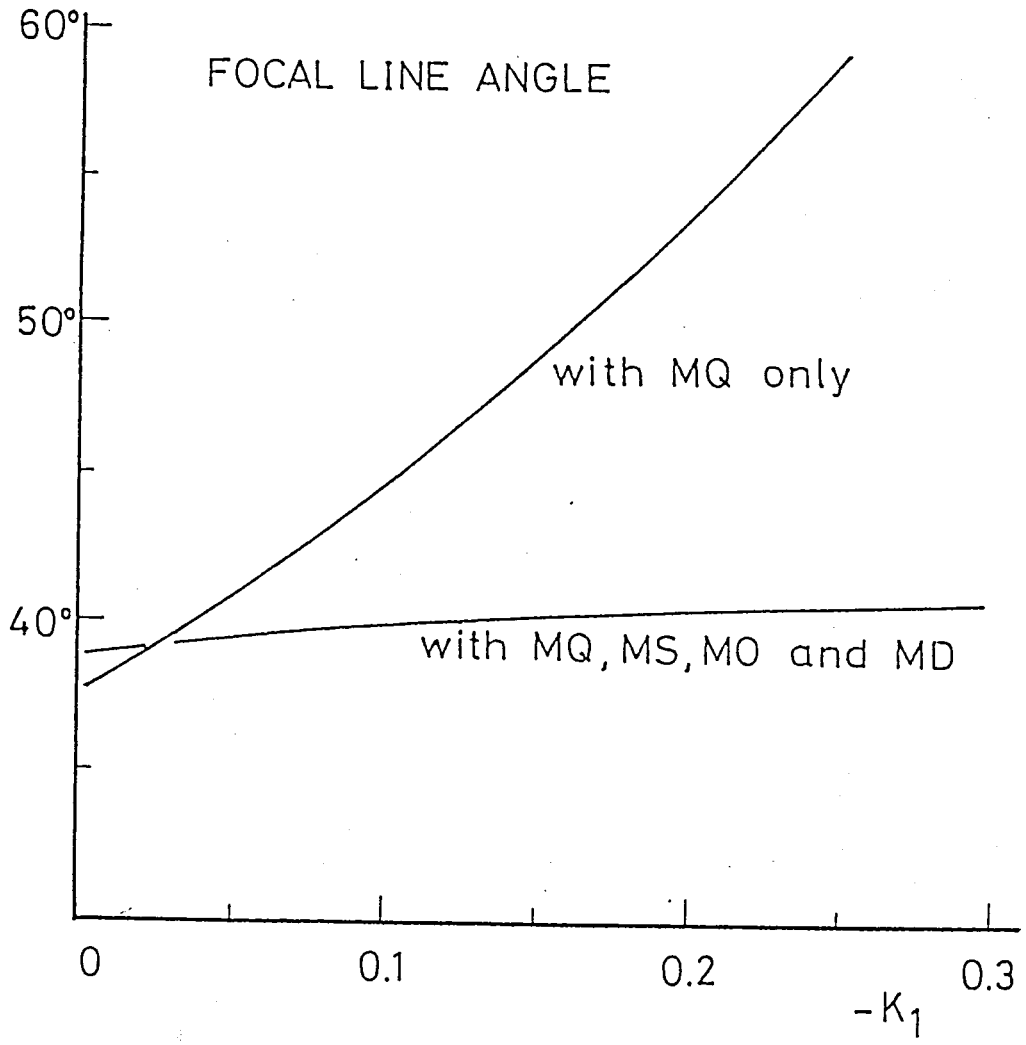
60°
50°
40°
FOCAL LINE ANGLE
with MQ only
with MQ, MS, MO and MD
0
0.1
0.2
0.3
$-K_1$

Fig. 2-2.

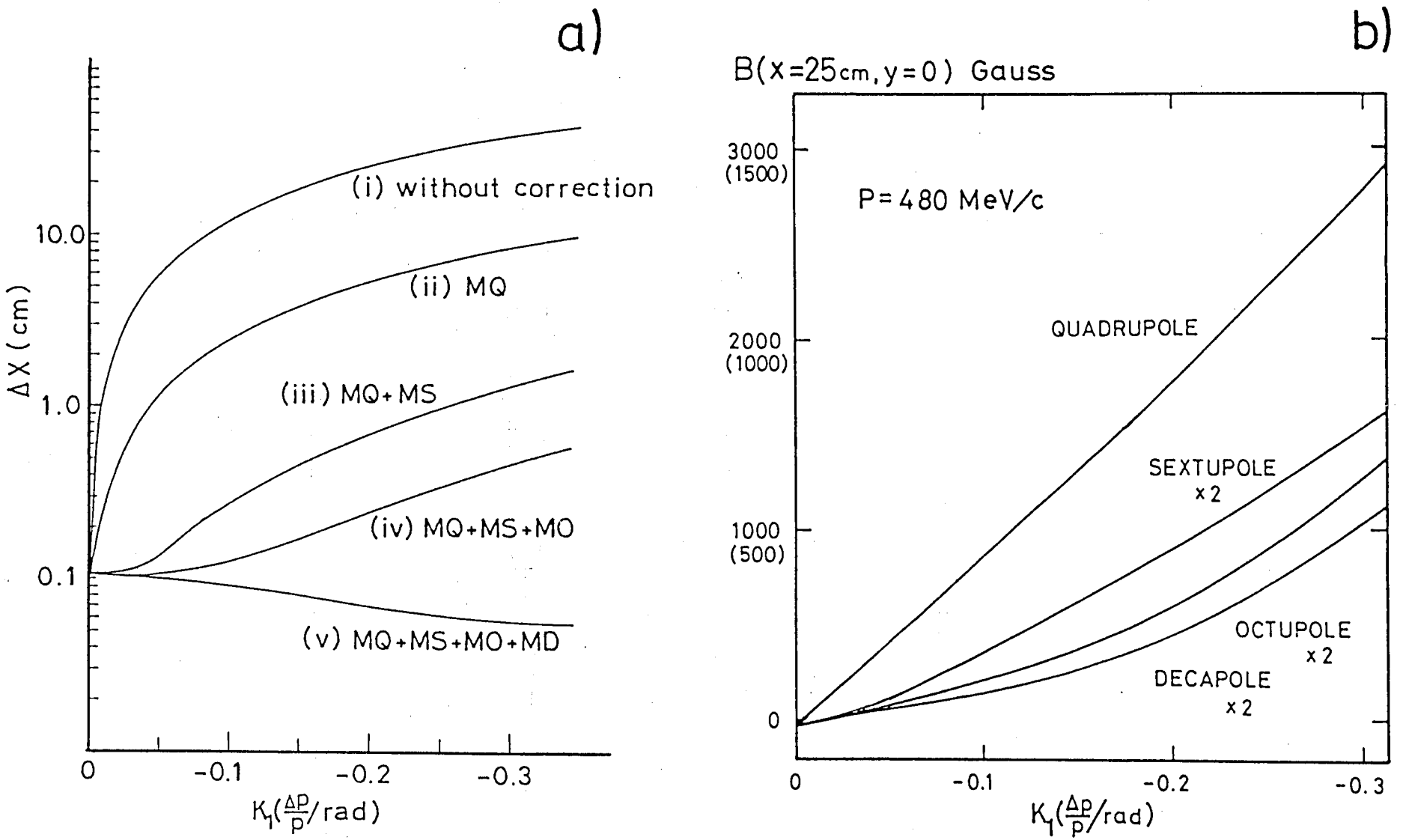
a)
ΔX (cm)
10.0
1.0
0.1
(i) without correction
(ii) MQ
(iii) MQ+MS
(iv) MQ+MS+MO
(v) MQ+MS+MO+MD
0
-0.1
-0.2
-0.3
K1(Δp/p/rad)
b)
B(x=25cm, y=0) Gauss
3000
(1500)
2000
(1000)
1000
(500)
0
P=480 MeV/c
QUADRUPOLE
SEXTUPOLE
x2
OCTUPOLE
x2
DECAPOLE
x2
0
-0.1
-0.2
-0.3
K1(Δp/p/rad)

Fig. 2-3.

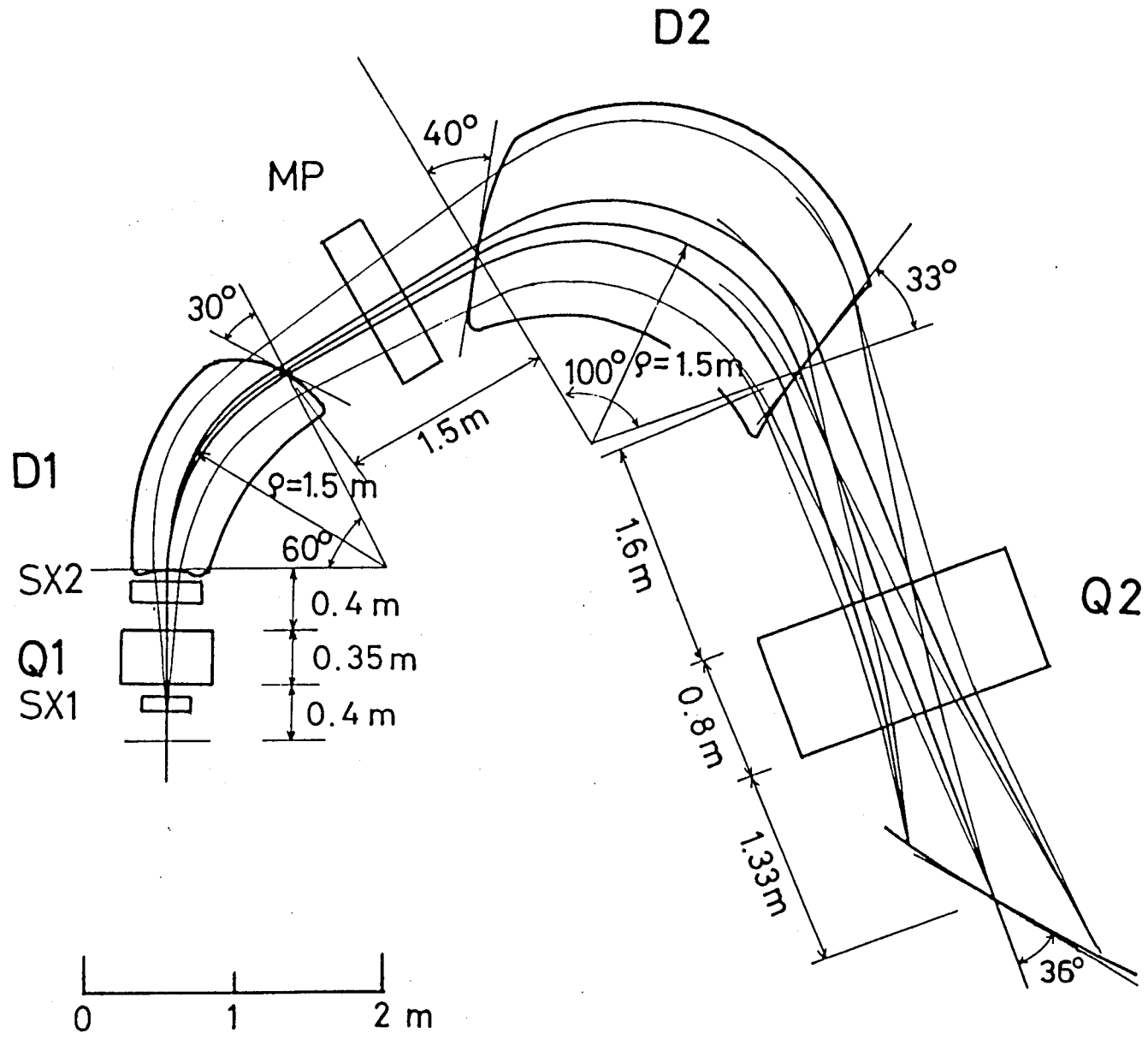
D2
40°
MP
30°
33°
100°
ρ=1.5m
1.5m
D1
ρ=1.5 m
60°
1.6m
SX2
0.4 m
Q1
0.35m
SX1
0.4 m
0.8m
1.33m
Q2
36°
0
1
2 m

Fig. 2-4.

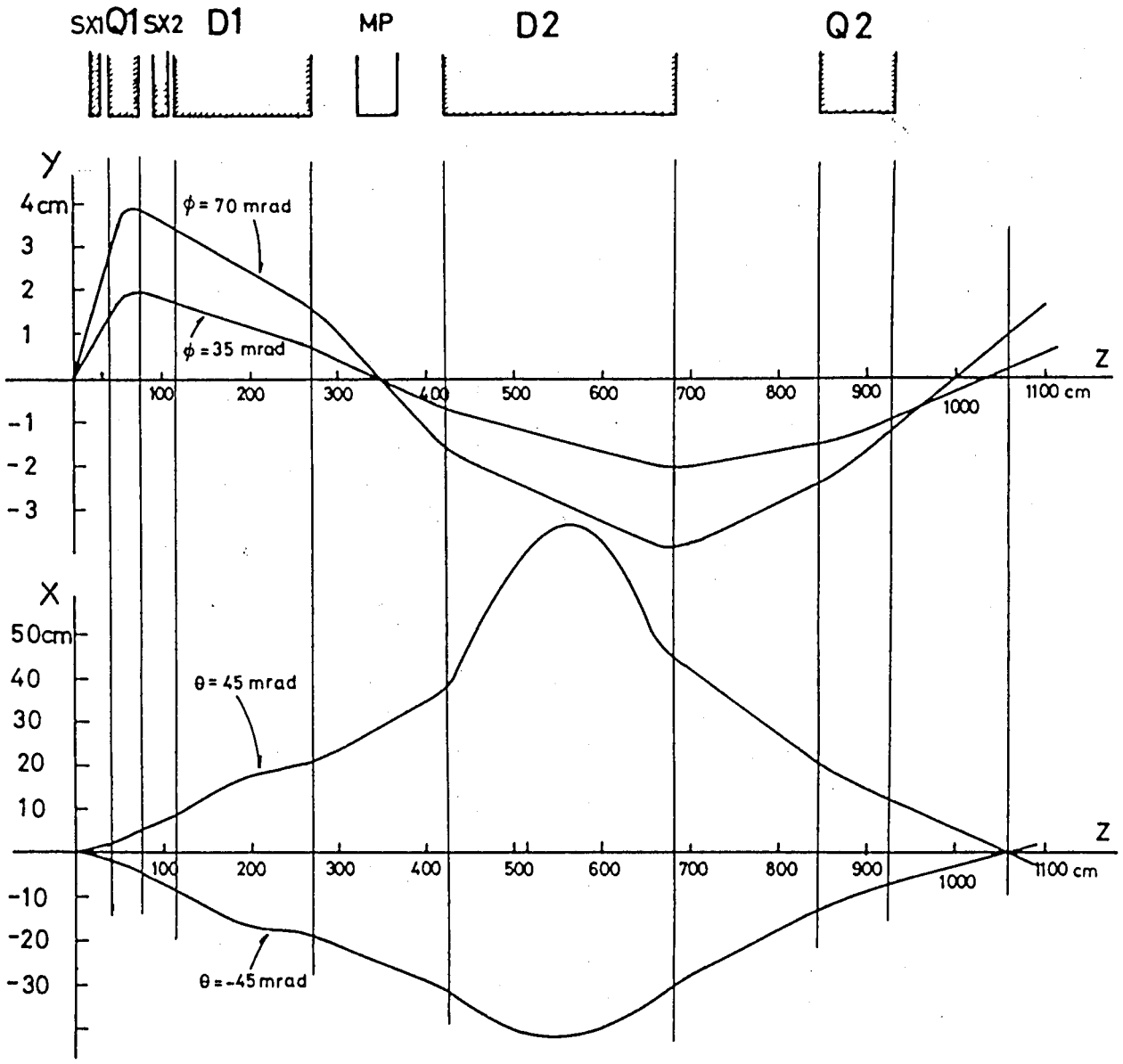
SX1
Q1
SX2
D1
MP
D2
Q2
Y
4cm
3
2
1
-1
-2
-3
φ = 70 mrad
φ = 35 mrad
Z
100
200
300
400
500
600
700
800
900
1000
1100 cm
X
50cm
40
30
20
10
-10
-20
-30
θ = 45 mrad
θ = -45 mrad

Fig. 2-5.

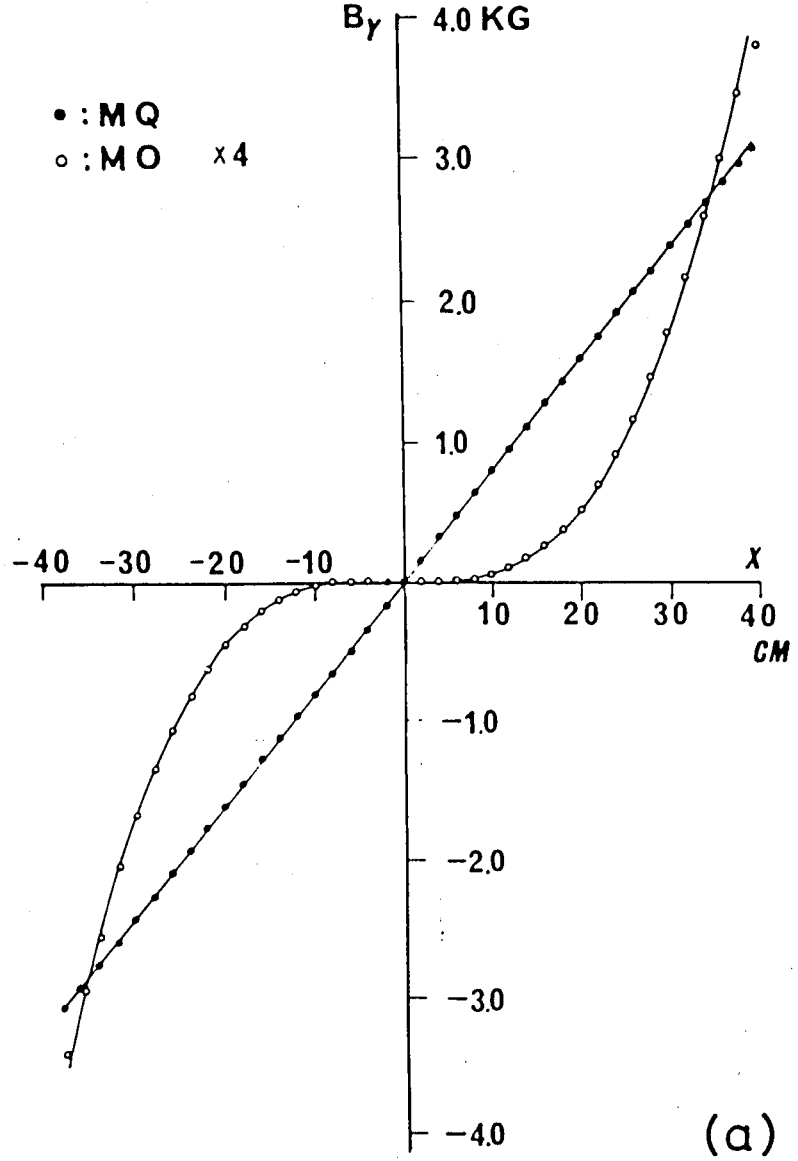
By
4.0 KG
• : MQ
○ : MO x4
3.0
2.0
1.0
-40 -30 -20 -10
X
10 20 30 40
CM
-1.0
-2.0
-3.0
-4.0
(a)

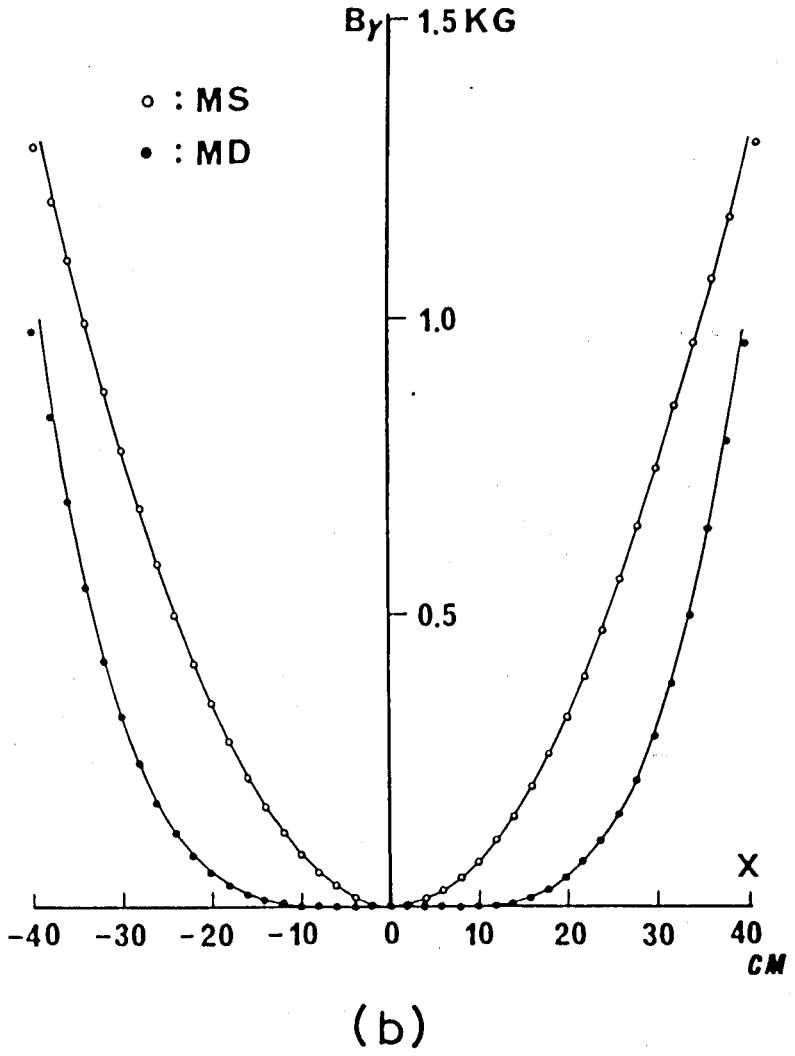
By
1.5 KG
○ : MS
• : MD
1.0
0.5
X
-40 -30 -20 -10 0 10 20 30 40
CM
(b)

Fig. 2-6.

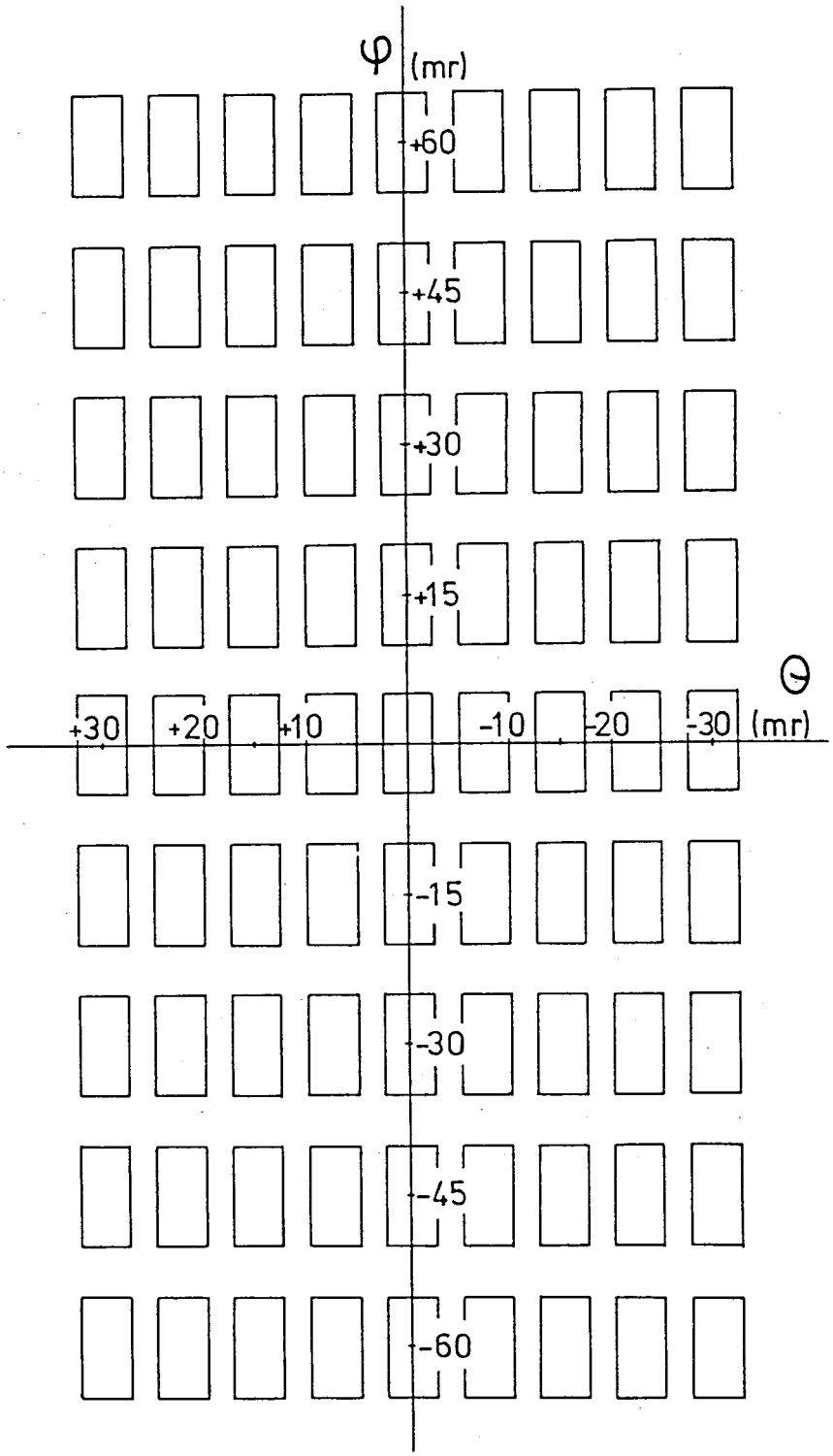

Fig. 2-7.

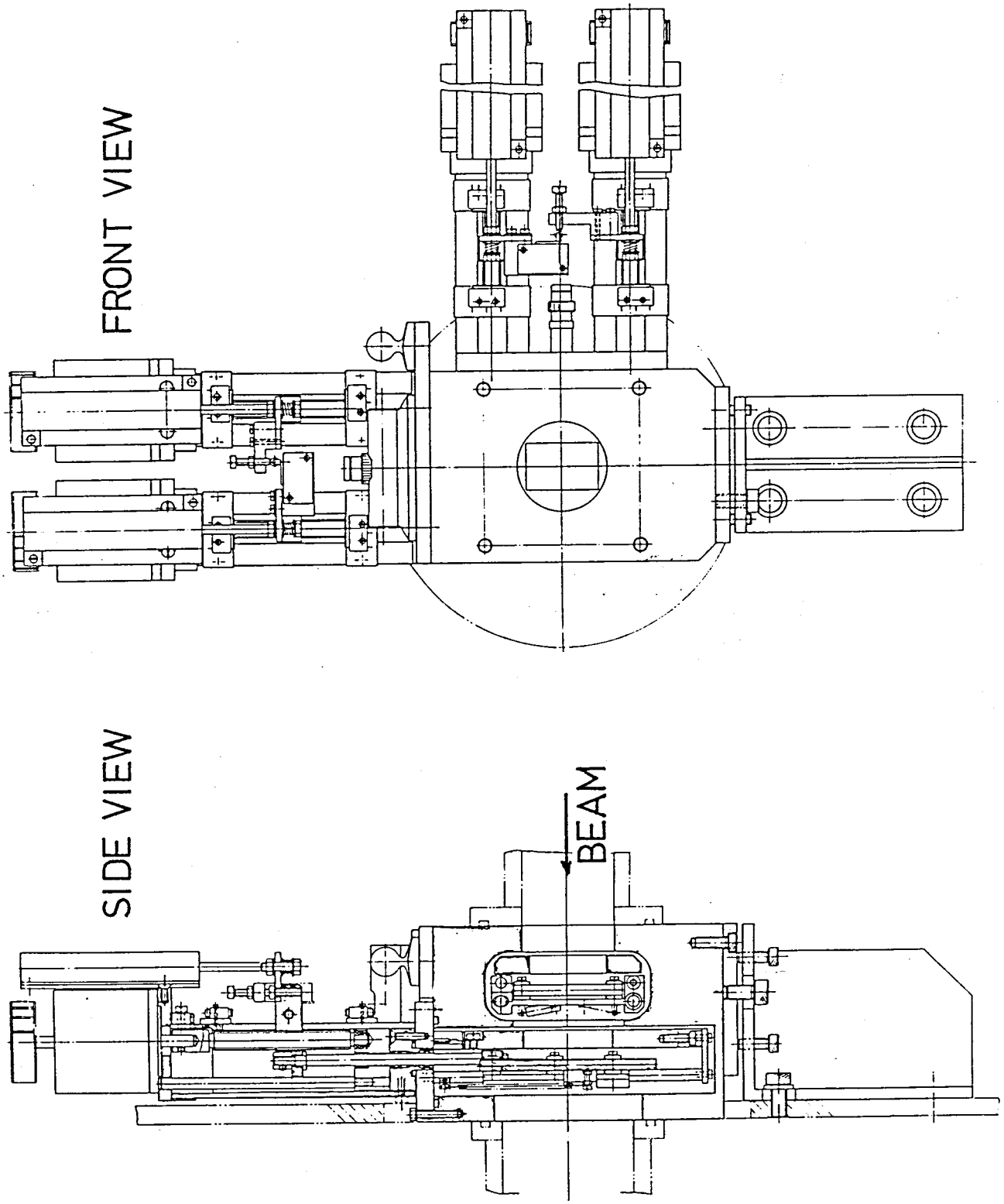

Fig. 2-8.

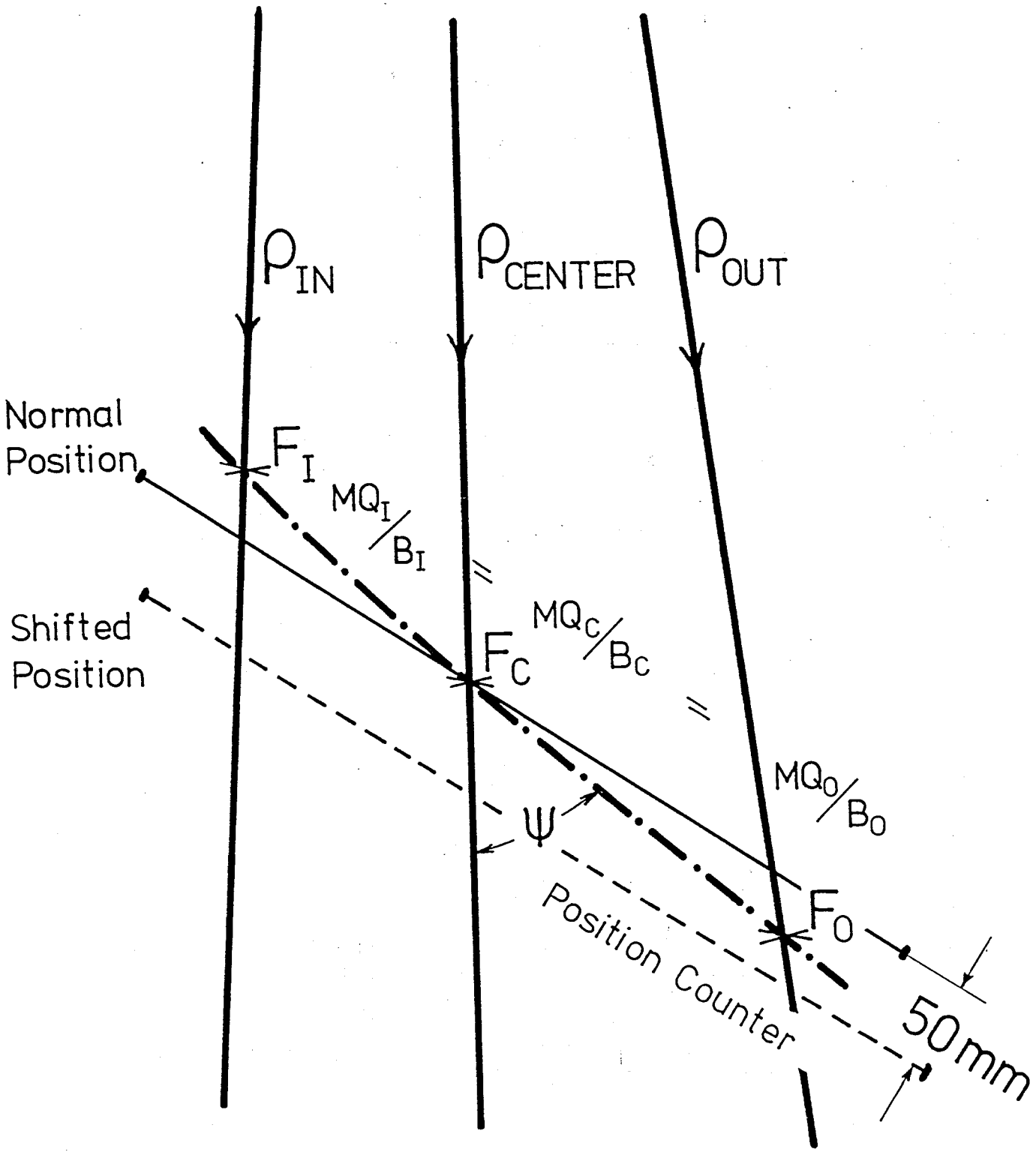
ρIN
ρCENTER
ρOUT
Normal Position
Shifted Position
FI
MQI/BI
FC
MQC/BC
MQO/BO
ψ
FO
Position Counter
50mm

Fig. 2-9.

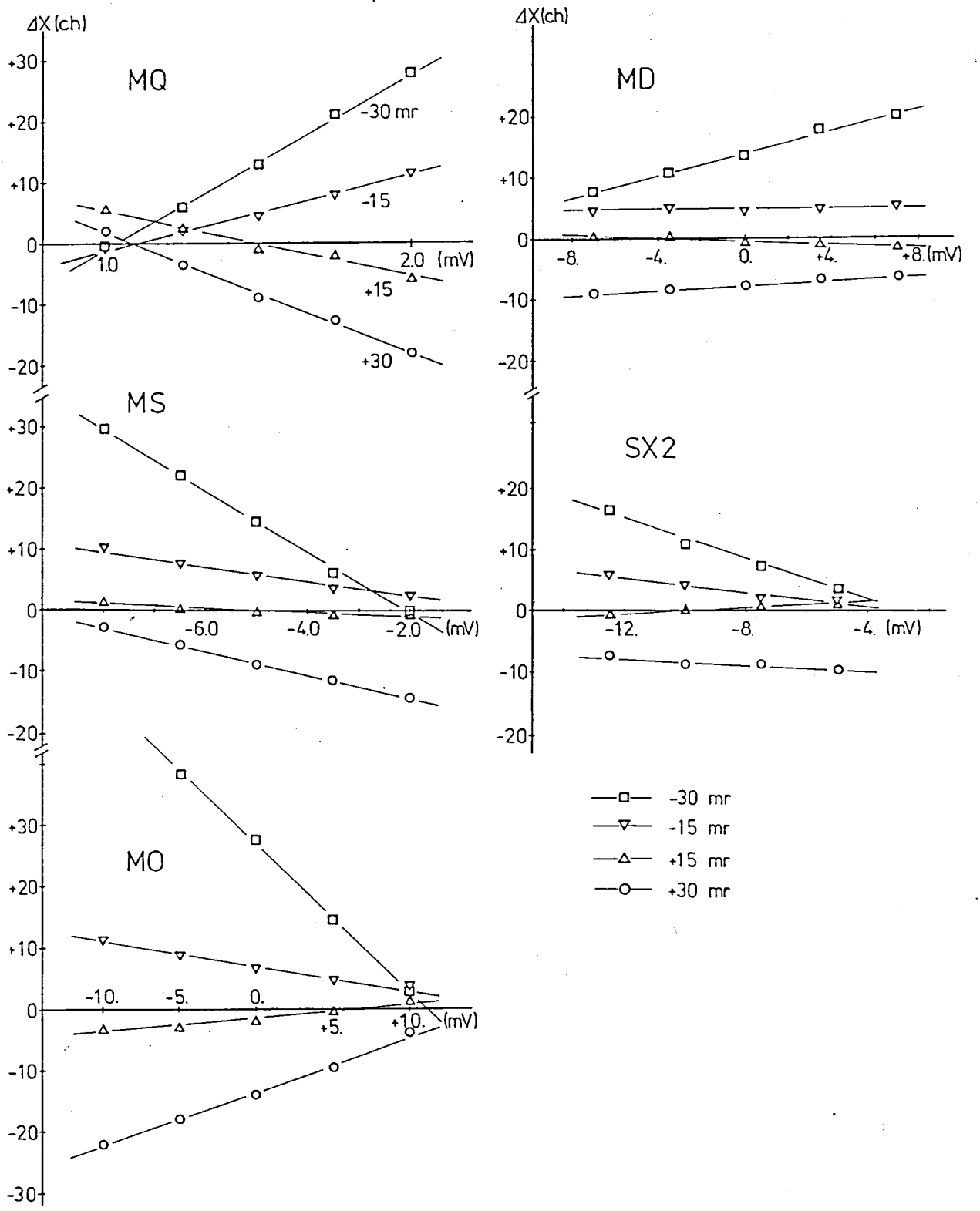
ΔX (ch)
MQ
-30 mr
-15
+15
+30
1.0
2.0 (mV)
MS
-6.0
-4.0
-2.0 (mV)
MO
-10.
-5.
0.
+5.
+10. (mV)
ΔX(ch)
MD
-8.
-4.
0.
+4.
+8.(mV)
SX2
-12.
-8.
-4. (mV)
-30 mr
-15 mr
+15 mr
+30 mr

Fig. 2-10.

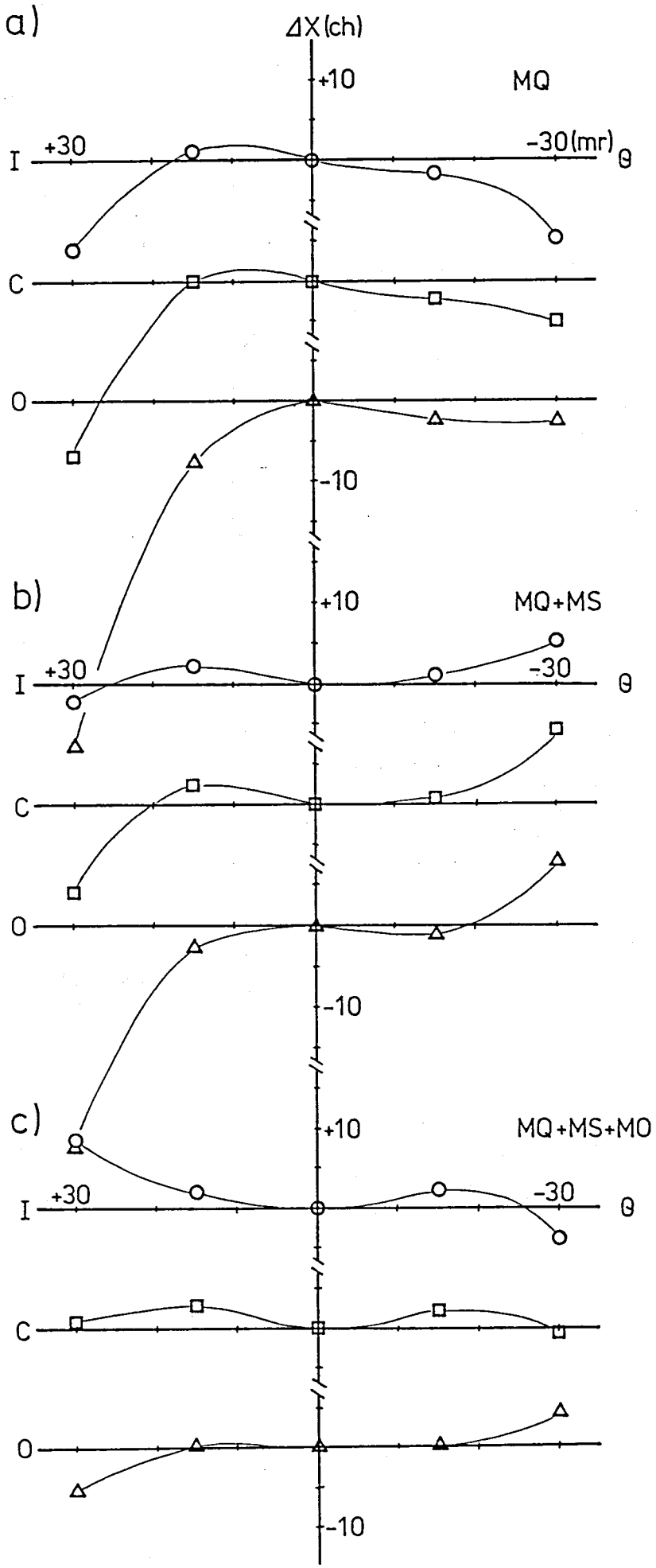
a)
ΔX(ch)
+10
MQ
I
+30
-30(mr)
θ
C
O
-10
b)
+10
MQ+MS
I
+30
-30
θ
C
O
-10
c)
+10
MQ+MS+MO
I
+30
-30
θ
C
O
-10

Fig. 2-11.

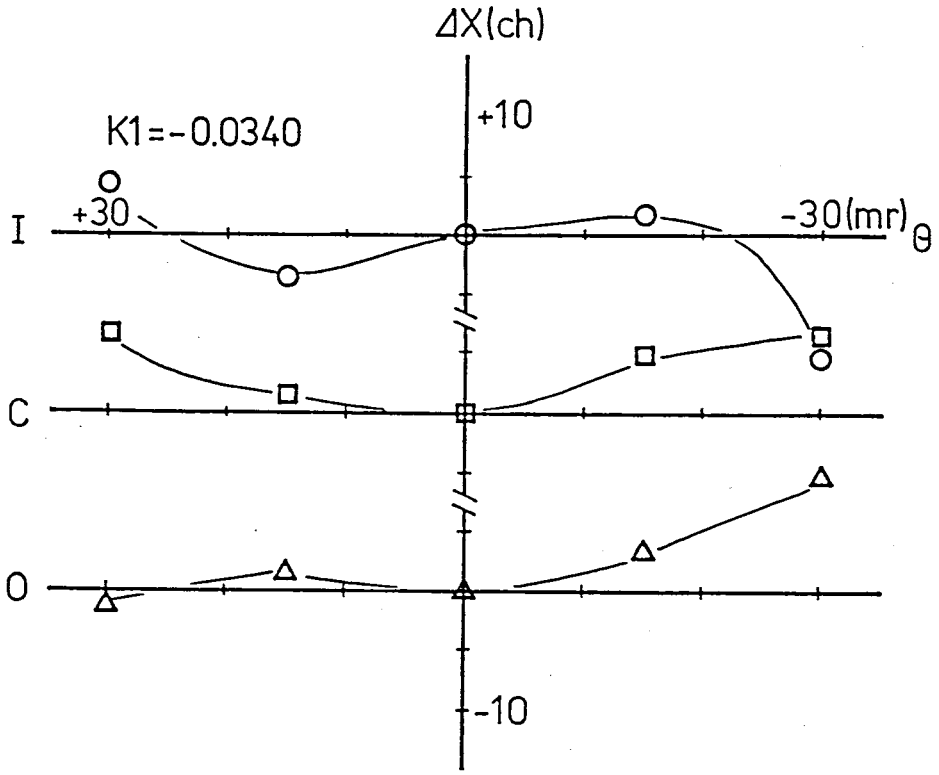

Fig. 2-12.

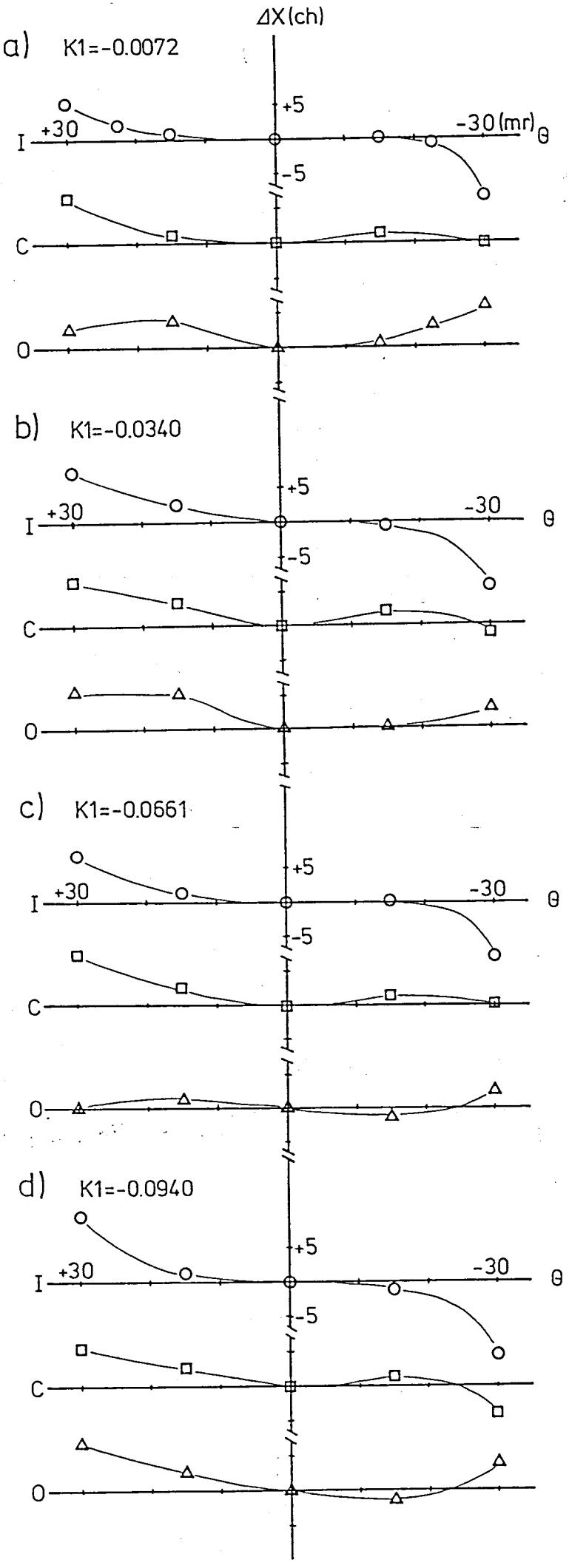
ΔX(ch)
a) K1=-0.0072
+5
+30
-30(mr)
θ
I
-5
C
O
b) K1=-0.0340
+5
+30
-30
θ
I
-5
C
O
c) K1=-0.0661
+5
+30
-30
θ
I
-5
C
O
d) K1=-0.0940
+5
+30
-30
θ
I
-5
C
O

Fig. 2-13.

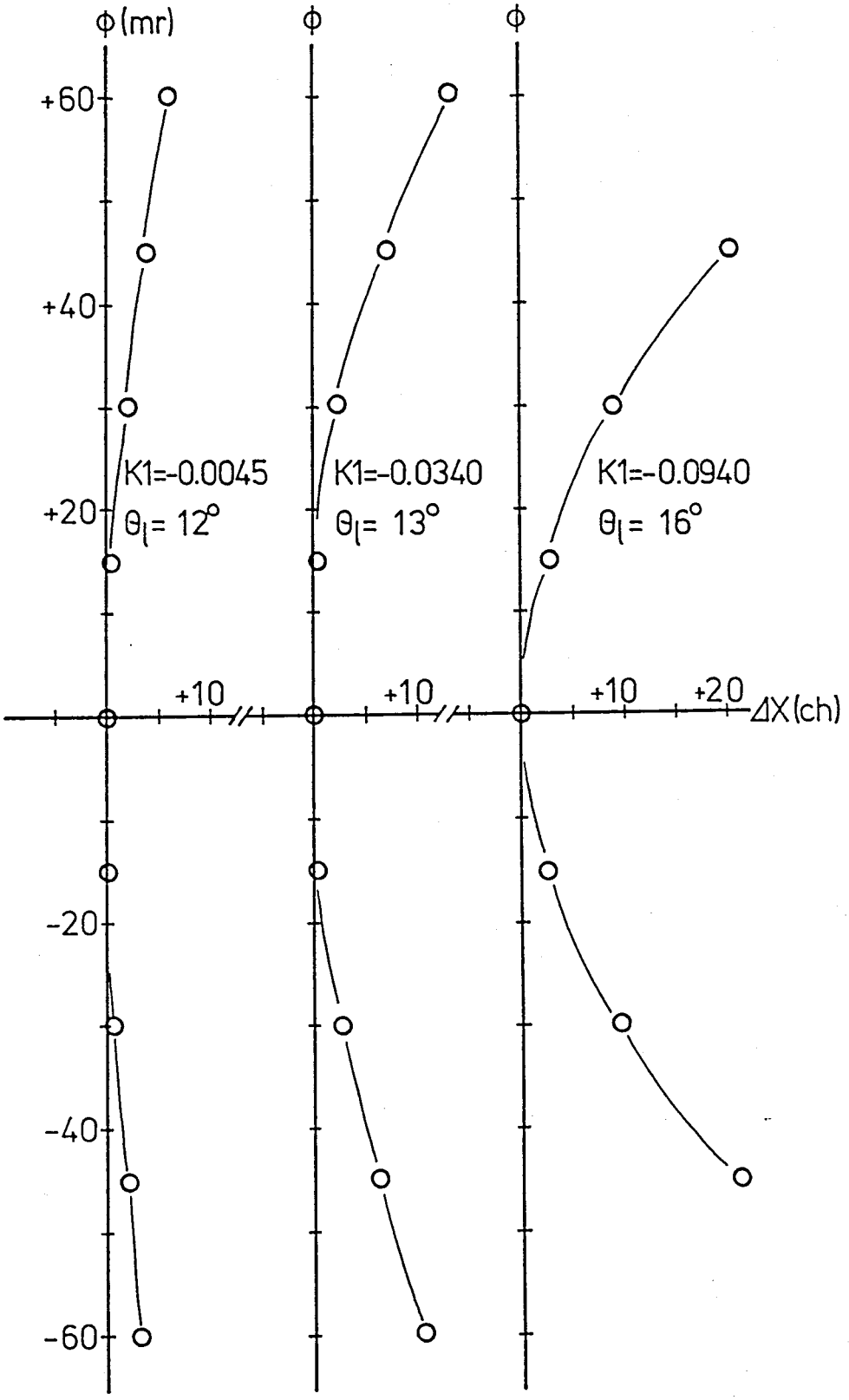
φ(mr)
φ
φ
+60
+40
+20
-20
-40
-60
K1=-0.0045
θl= 12°
K1=-0.0340
θl= 13°
K1=-0.0940
θl= 16°
+10
+10
+10
+20
ΔX(ch)

Fig. 2-14.

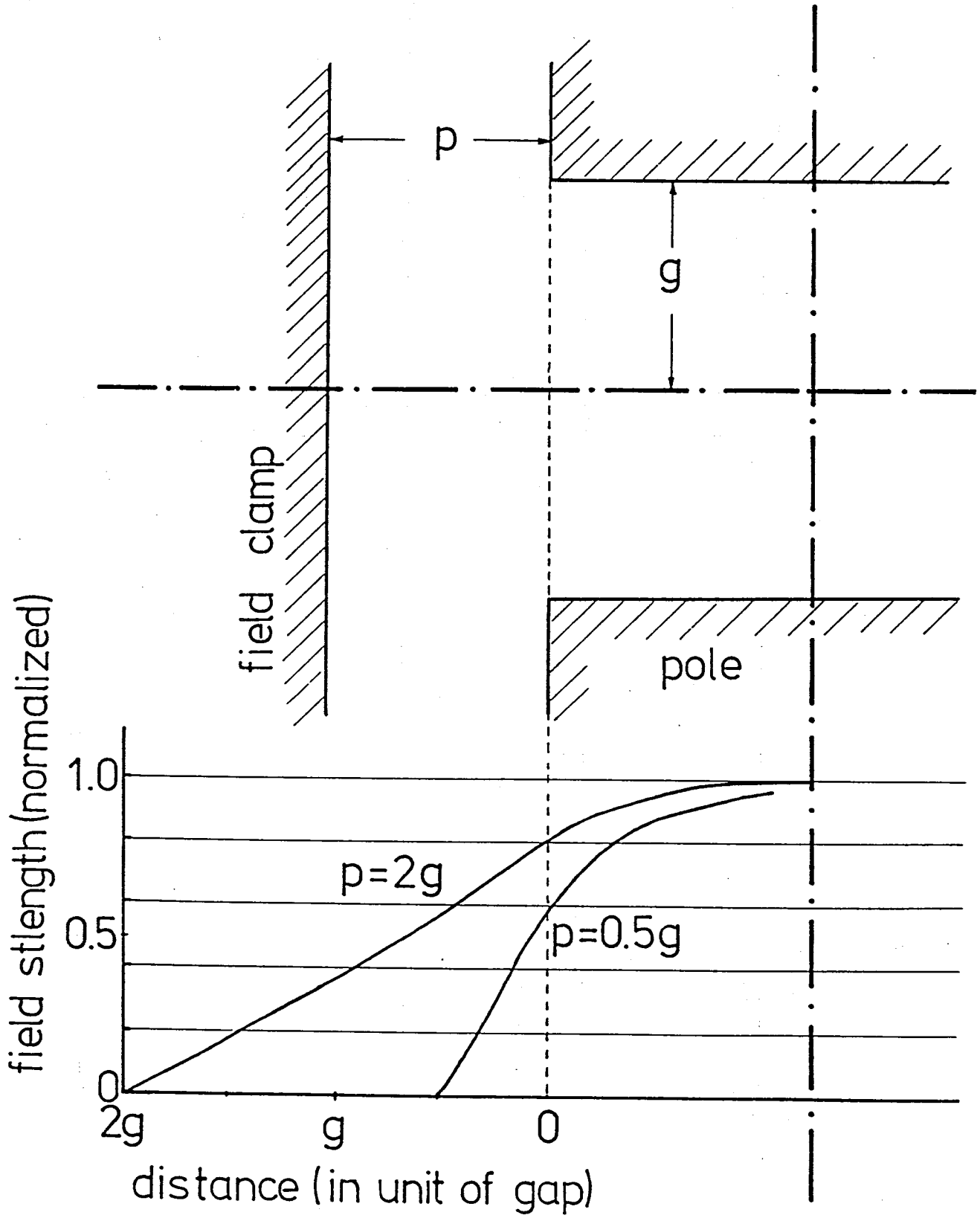
p
g
field clamp
pole
field stlength (normalized)
1.0
0.5
0
p=2g
p=0.5g
2g
g
0
distance (in unit of gap)

Chapter 3

Focal Plane Counter System for the Spectrograph

1. Introduction
2. Achievement of a long position counter
   - 2-1. Limitations encountered in MAPC
   - 2-2. Design principle of induction readout
     - 2-2-1. Introduction of sense wires
     - 2-2-2. Realization of multi-anode design by the induction readout wires
3. Counter system using induction wire proportional counter (IWPC)
   - 3-1. Construction of the counter system
     - 3-1-1. Position Counter
     - 3-1-2. Auxiliary counters
     - 3-1-3. Electronics and data taking system
   - 3-2. Operation and performance
     - 3-2-1. Output signal from the position counter
     - 3-2-2. Performance as a focal plane counter
     - 3-2-3. Elimination of pile-up effect by the fast rise time of the position pulses
     - 3-2-4. Particle identification
     - 3-2-5. Summary and example of a spectrum
4. Two dimensional position counter with induction readout
   - 4-1. Necessity for a two dimensional counter

Chapter 3

Focal Plane Counter System for the Spectrograph

Abstract

Focal plane counter system developed for the spectrograph is described. As focal plane detectors for the spectrograph with a long focal line, two kinds of position sensitive gas proportional counters were constructed. One is an induction wire gas proportional counter and the other is a two dimensional version of the same principle. In these two counters position informations are obtained by the charge division method using induced signals on resistive electrodes placed near anodes. Usual deterioration of resolution for the lightly ionizing particles of non-normal incidence is minimized by using a multi-anode design. The employment of the induction electrodes for the position readout made it possible to realize fast counting detector of multi-anode design with sub-millimeter position resolution for non-normal incidence (53.5° to the normal) of the particle rays.

1. Introduction

With a recent advent of large dispersion magnetic spectrographs, it has become necessary to develop position detectors which can cover their long focal lines that often exceed one meter. Using gas proportional counters, various systems have so far been designed[3-1] to detect the positions at which the analyzed particles hit the focal line. Among these, the resistive anode counter using the charge division technique[3-2~6] has proved to be one of the best detectors because of its simple counter structure and electronic circuits.

One of the main defect of this counter, however, has been the deterioration of position resolution for non-normal incidence of the particles especially for the particles with small ionization. Quite recently, Iwatani et al.[3-7] have shown, after the work of Markham and Robertson[3-8] concerning a stripped-cathode delay-line readout counter, that the problem can be solved if the single anode wire is replaced by multiple resistive wires. They used five anodes of carbon coated quartz filament mounted on a frame which was inclined to coincide with the direction of the particle rays. Since these five anode wires were expected to work as a stack of five thin counters, deterioration of resolution caused by the non-normal incidence of the particles was drastically reduced. Both 20 cm and 40 cm counters of this design succeeded in achieving good resolution of about 0.7 mm for 28 MeV protons with an incidence angle of 55° to the

normal and showed their usefulness as the focal plane counters.

When this multi-anode proportinal counter is extended (hereafter refered as MAPC) to an effective length of 1 m or longer, a problem, however, arises from the characteristically slow rise time of the output pulses. In the usual nuclear experiments where the background counting rate is often as high as a few tens of kHz, the occurrence of pile-up of the output pulses causes inaccuracies in the position determination, giving rise to a deterioration of position resolution. The pile-up probability increases with increasing rise time. A simple estimate for a 1 m long MAPC predicts a rise time value of around 15 μs which would cause the fractional amount of the inaccurately detected events to be as large as 30% for the assumed background counting rate of 20 kHz. Since the background rate is expected to increase with the length (or effective volume, it is of considerable importance to reduce the rise time value for a long counter to as small a value as possible.

In the present chapter, we describe an "induction wire proportional counter (IWPC)" and a two dimensional type counter, which is a developed version of IWPC. In IWPC, the good points of the multi-anode configuration and charge division technique is fully used. By inserting induction electrodes for position readout between the anodes and cathode, we could reduce the rise time of the position pulses to less than 1 μs for a counter length of 1 m. The

two dimensional counter was born by combining the IWPC with a drift counter for knowing the vertical incidence position of the particle. Two dimensional determination of the incidence position of the particle is effective in reducing the aberration of the spectrograph caused by the $(x|\phi^2)$ term and therefore in achieving higher resolution of all spectrograph system. Two dimensional display of the incidence position is found to play an important role in discriminating abnormally scattered background particles which tend to spread over rather widely off median plane.

The auxiliary detectors for particle identification and the data acquisition system are also described.

2. Achievement of a long position counter

2-1. Limitations encountered in MAPC

In a counter with the charge division readout, the anode wires normally have two functions i.e. producing a high electric field for gas multiplication and transmitting charge signals for position redout. To maintain a large gain of gas multiplication, it is necessary to keep the thickness of the anode wires around a few tens of μm, and the accurate calculation of position requires a sufficiently large anode resistance compared with the input impedance (about 100 Ω or so) of the charge sensitive preamplifiers. The only commercially available wires meeting these requirements are those of resistive metal alloys (stainless steel or nichrome) and carbon coated filament (hereafter refered as CCF) having resistivities of a few Ω/mm and several kΩ/mm, respectively.

It should be noted that the rate of charge collection on one end of the anode is inversely proportional to the anode time constant which is a product of the anode resistance and anode-cathode capacitance. For fast rise of the output pulses, it is therefore essential to keep the anode resistance as small as possible, which is usually in contradiction with the above requirements for the anode thickness.

The conflict becomes especially serious for a long counter where both the anode resistance and capacitance are generally large. In our preliminary test with a 50 cm long

MAPC of the three-anode type, 25 μm thick CCF wires (8 kΩ/mm) were used to obtain a moderate gas gain for 55 MeV proton beams and the rise time of the position pulses was observed to be nearly 4 μs. If we extend this counter keeping the same anode configuration to a length of 1 m, the anode time constant is expected to become four times as large considering the approximate proportionalities of the anode resistance and capacitance to the counter length. The rise time in a 1 m long MAPC will therefore be about 16 μs, which is too large for a counter which has to work under a high background rate. Of course, the use of the metal wires instead of CCF yields a much smaller resistance and hence a much faster rise time. However, in the MAPC where the multiple wires are connected together to sum up the charge signals on the individual wires, the total resistance of the metal anodes usually becomes no larger than 1 kΩ which is too small for the accurate calculation of position to be performed.

2-2. Design principle of induction readout

2-2-1. Introduction of sense wires

In order to overcome the above difficulties, we adopted a new wire configuration which includes additional wire electrodes between the anode and cathode as shown in Fig. 3-1. These grid wires are arranged with the same spacing as the anodes and kept at a potential for which no gas multiplication is expected. As is well known, such grid wires also carry charge signals being induced through the motion of

ions in the counter volume and can act as "sense wires" for the ionization events[3-4, 3-10~15]. If the position signals are only picked up from the sense wires, the anodes can be devoted to the exclusive production of electric fields for gas multiplication. With this scheme of readout, it is important that there is no restriction on the resistance of the anodes and that the sense wires are free from the thickness limitations. The fast rise of the position pulses may therefore be easily achieved by choosing sense wires of an appropriate resistivity without any regard to the gas gain. The choice of the materials for all the electrodes can, in practice, be based upon the mechanical strength and smoothness of the surface, both of which are quite important characteristics in the actual counter construction and performance. The most suitable wires for the electrodes in this design will then be thin metal wires for the anodes and rather thick CCF for the sense wires.

2-2-2. Realization of multi-anode design involving the induction readout wires

The usefulness of the multiple anodes in improving the position resolution for non-normal incidence of the particles still holds in this IWPC. The ions in an avalanche close to an anode wire induce charges on the sense wires in a somewhat distributed way. Let us consider the charges, for example, on the sense wire located nearest to the avalanche. An electrostatic calculation similar to that given in ref. 3-14

predicts that the induced charge distribution along a sense wire has a centroid at the closest point to the avalanche and a width (FWHM) roughly equal to the anode-sense wire separation (a in Fig. 3-1).

The charge signal at each end of the wire may be expressed as a sum of the point charge responses[3-16~18] over the distribution. Since the width of the distribution is very small compared with the length L of the counter, it is expected that the charge signal is, to first order in a/L or exactly for a long period of charge integration, equal to that obtainable when all the charges are induced at the centroid.

These considerations indicate that a sense wire correctly picks up the position of an avalanche on an anode wire. Therefore if the sense wires are mounted on an inclined frame so that $\theta=\theta_0$ in Fig. 3-1, the position calculation can be accomplished in just the same way as was done in the MAPC by Iwatani et al. Although the charges may also be induced on wires other than that closest to the avalanche, the symmetry of the charge distribution about the closest wire guarantees that the signals from such wires cause no error in the determination of position, provided a sufficiently large number of sense wires are employed. In practice, the use of a limited number of wires may produce a small error in the location of the avalanche.

If we assume a uniform gas gain over all the anode wires, a simple statistics calculation enables us to predict

that a theoretical limit of the position resolution R can be approximated as

$$R^2 = \frac{r^2}{N} + \frac{1}{N}\left(\frac{N-1}{N}\right)^2 \left(r^2+\frac{1}{N}\Sigma f_i^{\,2}\right)\left(\frac{\delta E}{\Delta E}\right)^2 , \qquad (3\text{-}1)$$

where r is the uncertainty in position (projected onto the anode wire) due to energy loss fluctuations[3-8] in a unit cell of the counter volume seen by a single anode, where N is the number of the cells or the number of anodes, f_i the readout error of the position of the avalanche on the i-th anode and $\delta E/\Delta E$ is the ratio of the energy loss straggling to the mean energy loss along the particle path in the unit cell. The readout error f_i is given by

$$f_i = d_i(\tan\theta_0-\tan\theta) + k_i\tan\theta_0 , \qquad (3\text{-}2)$$

with

$$k_i = \sum_i [q_{ij}(s_j-d_i)] / \sum_j q_{ij},$$

where s_j and d_i are the distances in the planes of the electrodes from the center of the counter to the j-th sense wire and to the i-th anode, respectively, and q_{ij} denotes the amount of charge on the j-th sense wire induced by the avalanche on the i-th anode. The second term in eq. (3-2) represents the readout error caused by the use of a limited number of sense wires. If some irregular fields shift the

avalanche positions, f_i should also include such errors. For a given configuration of the wires, the frame angle of the sense wires has to be chosen so that the second term in eq. (3-1) may be minimized. However, the choice is not usually so critical for the resolution owing to the reduction foctor of $(\delta E/\Delta E)$ which is around 0.1 for light ions.

3. Counter system using Induction Wire Proportional Counter

3-1. Construction of the counter system

3-1-1. Position counter

The cross sectional view of the IWPC is shown in Fig. 3-2. The anode and sense wires are arranged on the three different planes which are parallel to the beam direction and spaced 5 mm apart from each other. The sense wires are positioned symmetrically about the anode plane which forms the central plane of the counter and the same spacing of 3.5 mm is used for all the electrodes. In order to terminate the field irregularities at the entrance and exit faces of the counter, additional "guard wires" are used at the ends of the electrode planes. The materials used are Cu-Mn-Ni alloy (25 μm thick), CCF (75 μm) and gold plated tungsten (100 μm) wires for the anodes, sense and guard electrodes, respectively. The resultant resistance of one sense wire is 300 kΩ. The smoothness of the wire surfaces was carefully checked under a microscope.

The original design involved the use of five anodes and fourteen sense wires. However, in our preliminary test of the counter [3-19], a large variation was observed in the gas gain from anode to anode, indicating that the electric field strength around the central anode region of the counter was reduced to some extent. This fact can be understood from the result of the numerical field calculation[3-20] which was obtained by solving the Laplace's equation (see Fig. 3-3a). In order to diminish this effect,

the central anode has been replaced by a guard wire in the present design and has been electrically connected with the other guard wires on the same plane. This replacement yielded approximately equal gas gain over the active four anodes for an arbitrary choice of the guard wire potential. The calculated field distribution is shown in Fig. 3-3b. This replacement and the appropriate potential value put on the sense wires together makes the equipotential line fairly parallel with the anode plane, which assures the anodes to act as a stack of thin counters (about the potential value on sense wires detailed discussion will be given in Section 3-2-1).

The number of sense wires has been determined mainly from the resistance required to facilitate a fast as well as accurate position readout and from the practical simplicity of the wire configuration. The k_i values in eq. (3-2) were calculated from the distribution of induced charges. Using the results, the support angle of the sense wires has been determined to be $\theta_0 = 56.5°$ for the expected beam angle of $\theta = 54.5°$.

All the wires are mounted on two frames made of 1.2 cm thick and 105 cm long aluminium plate with teflon blocks being fixed to the ends to act as wire supports. The frames are placed at the top and bottom of the interior of the counter body and the wire supports are inclined at the above mentioned angle of 56.5° (see Fig. 3-4). The wires are fixed with epoxy resin to stainless steel pipes (outer

diameter of 0.75 mm) inserted into 0.6 mm holes in the teflon blocks. The pipes also act as guards against spark to occur at the end part of wires kept at high voltages. Using conductive paste, the electrical connections of the wires have been made separately in the respective groups of the anodes, sense wires, guard wires on the anode plane and guard wires on the sense electrode plane. The counter body is an aluminium box with overall dimensions of 5 cm × 9 cm × 123 cm. The entrance and exit windows are made of 9 μm thick aluminized Mylar sheets, which serve at the same time as cathodes and as the gas seals for the counter body. The active length of the counter is about 100 cm and the vertical aperture is 2.2 cm.

The expected position resolution can be calculated from eq. (3-1) using plausible values of r = 0.63 mm taken from ref. 3-8 and $(\delta E/\Delta E) = 0.3$ determined from the Vavilov distribution[3-1]. The result is R = 0.35 mm to which the second term in eq. (3-1) has quite a small contribution for the optimized value of $\theta_0 = 56.5°$.

3-1-2. Auxiliary counters

As a back-up counter system, a dual ΔE-counter and an E-counter are used just behind the position detector to identify the particles and to reduce the background counting rate as schematically shown in Fig. 3-5. The ΔE-counter involves two anodes which are held in an aluminium box, identical to that of the position detector, and the separa-

tion is accomplished by the use of an aluminized Mylar sheet. The purpose of using the dual structure is to reduce the background by requiring coincidence of increased multiplicity. The anode material used is a Cu-Mn-Ni alloy wire having a diameter of 25 μm. The E-counter is a plastic scintillator (NE-110) 2 cm thick, 4 cm high and 150 cm long. It is thick enough to stop the 70 MeV proton particles with non-normal incidence. Two photomultipliers are coupled to the both ends of the scintillator by optical compound and being pressed by coil springs to keep the optical contact in a good condition. The signals from them are summed together in an electronic circuit.

3-1-3. Electronics and data taking system

The block diagram of the electronic circuits and the data acquisition system is shown in Fig. 3-5. In the present system, the position signals are passed to a computer and the position coordinates of the particles are calculated using software. The signals from the auxiliary counters are simply used to select the events to be accumulated and the particle identification is performed by setting ΔE and E windows at the respective single channel analyzers. Most of the circuits are commercially available ones of conventional types.

The detail of the data acquisition system and the signal flow is shown in Fig. 3-6. The data acquisition system is designed to accept data from two independent

counter systems. A set of digital outputs prepared by the ADCs are fed to the CAMAC modules connected to a computer (PDP-11/40) through a general purpose interface "Raw Data Processor (RDP)"[3-21] and a logic circuit called "Coincidence Unit (CU)"[3-21]. The device CU has been designed to eliminate unpaired position signals that may happen to be caused by small discrimination of pulses at the ADCs. With this, the busy time of RDP and the computer is minimized.

According to the calculated position, the corresponding part of the memory in the computer are updated. Monitoring of the spectrum is available at the graphic terminal during the experiment. The maximum counting rate is about 300 Hz, which is mainly limited by the software.

3-2. Operation and performance

3-2-1. Output signal from the position counter

The counter is normally operated in a counting gas of a mixture of Ar(95%)-CO_2(5%) at a pressure of 1 atm. The anodes are biased at about 2900 V to the cathode and the sense wires are kept at a potential of 40% of that value. The fractional voltage of the guard wires on the anode plane has tentatively been chosen to be 70% and the guard wires on the sense wire planes are maintained at the same potential as for the sense wires. Although the present counter has been proved to work at higher anode potential as well, a slight indication of the increase of avalanche size has been observed above 2950 V.

A typical example of the signals obtained from the sense wires under the above operating conditions is shown in Fig. 3-7. The figure also contains an anode pulse in an inverted form for reference. Both the signals were observed at the output terminals of charge sensitive preamplifiers having differentiation time constants of 50 μs. In this figure it may easily be seen that the sense wire signal has a remarkably short rise time when compared with the aforementioned expectation for an MAPC of the same length, clearly showing the effectiveness of the employment of low resistance induction wires in producing fast pulses for position readout. The actual value of the rise time was measured to be about 0.8 μs. The measurement showed that the rise time value is nearly independent of the position of incidence of particle rays.

The figure also illustrates the characteristic behaviour of the sense wire signal with time, starting at the same time as the anode signal and forming a bump at around 100 μs after the start. Note that the long undershoot seen in the figure is a result of differentiation in the preamplifier. This bump is considered to be caused when the positive ions, while drifting from the anode to cathode, pass through the plane of the sense wires[3-4, 3-13~14]. Its height therefore is expected to be a function of the drift velocity of the ions in the region near the sense wire plane. Indeed, it was observed that the bump height decreases with the decreasing voltage difference between the anodes and sense wires, corresponding to the reduction of the drift velocity.

In order to prevent the bump from producing a spurious pulse in the main amplifier, a higher potential is used for the sense wires, which, however, tends to reduce the gas gain. The above choice of the sense wire potential (40% of that of the anodes) was found to yield a good performance in eliminating spurious pulses at the output of the main amplifier without seriously reducing the signal height. Relatively large deviations from this choice were also allowed in practical operation.

3-2-2. Performance as a focal plane counter

The performance of the counter system was examined using mainly 65 MeV proton beam from the AVF cyclotron at RCNP. The counter was placed on the focal line of the spectrograph forming an angle of 35.5° with the trajectories of the particles i.e., the particle incidence angle was set at 54.5° to the normal line of the counter. The vacuum end of the spectrograph is a 40 μm thick Mylar window which together with the counter window is expected to cause a beam spread of less than 0.1 mm at the center of the counter depth for the particles. The image size on the focal line ranged from about 1-3 mm depending mainly on the tuning of the beam line and partly on the slit settings at the entrance of the spectrograph.

The linearity of the counter was checked by measuring the position of the shadows of many of evenly spaced bars put in front of the position counter using particles with

continuous spectrum emitted from a thick (∿1 mm) aluminium target. The resultant relationship between the channel numbers of the computer output and the positions of the bars is shown in Fig. 3-8. Although slight nonlinearity of less than 1% was observed at the both ends, good overall linearity is apparent from the figure.

The best resolution result was observed in the spectrum of elastically scattered 65 MeV protons from a 370 $\mu g/cm^2$ thick ^{50}Cr target after re-tuning the beam line to yield a beam energy spread of about 10^{-4} at the target. The vertical aperture of the entrance slit of the spectrograph was also readjusted to reduce the aberration. The overall resolution observed was 1.8 mm as shown in the spectrum in Fig. 3-9 which was taken with τ = 1 μs at a total counting rate of about 1 kHz. Apparently this resolution includes contributions from many sources other than in the position counter. They are the energy spread in the primary beam (1.0 ∿ 1.8 mm), finite beam spot size on the target (1.0 mm), angular spread of the particles detected (0.2 mm), energy loss straggling in the target (0.3 mm), multiple scattering in the vacuum seal of the spectrograph as well as in the entrance foil of the counter (0.1 mm) and circuit noises (0.3 mm), with the respective contributions being given in the parentheses. If all these are subtracted in quadrature from the observed resolution, the intrinsic resolution of the present counter becomes no larger than 1.1 mm or most probably around 0.8 mm. Although, due to the large

uncertainty involved, we are not in a position to discuss the experimental resolution in detail, the result does suggest the presence of room for improvement in order to bring the resolution closer to the theoretical limit of 0.35 mm.

3-2-3. Elimination of pile-up effect by the fast rise time of the position pulses

As presented in Section 3-2-1, the position signal from the counter has a rise time of 0.8 μs which would allow a short shaping time of the main active filter amplifiers (ORTEC 572). To see the effect of the shaping time τ on the position readout at a high counting rate, deuteron spectra of $^{50}Cr(p,d)$ with the previous target were observed for different time constants between 0.5 and 3 μs. Keeping the other circuit parameters constant, the spectra as shown in Fig. 3-10 were obtained for the low lying states in ^{49}Cr at a total counting rate of 25 kHz in the position counter. In this figure the pile-up effects are evident for larger τ in the broadened shapes at the skirts of the spectrum lines. The broadened skirts are considered to be due to position pulses that were slightly modified in height by accidental coincidences with the small background pulses caused by the gamma-rays and neutrons which were uniformly distributed over the counter length. This effect is seen to be considerably reduced as τ, an equivalent of the resolving time, decreases. The relative peak positions, on the other hand,

were found to be in good agreement with each other, indicating a constant position linearity irrespective of the τ values adopted. These facts show that the present method for the production of the fast position pulses on the sense wires allows the charge division technique to be as effective as in the multi-anode counter whilst eliminating the pile-up effect to a large extent. The elimination of this effect was nearly complete in the case of τ = 0.5 or 1.0 μs at the counting rate examined. Since the amplitudes of the position pulses were observed to be reduced by 30% for τ = 0.5 μs, the best choice would be τ = 1 μs in the practical use of the counter.

In Fig. 3-11 we show the spectrum line width of the first excited state in ^{49}Cr (the most prominent peak in Fig. 3-10) as a function of the total counting rate in the position counter for τ = 1 μs. This was obtained by changing the primary beam intensity at the ion source of the cyclotron. Although the position resolution shown in the figure was predominated by the energy spread in the primary proton beam, the FWHM may be seen to be practically constant up to the total counting rate of 25 kHz. Since for τ = 1 μs, the pile-up of the position pulses is expected only to have an effect on a few percent of the total events, the slight slope seen in the figure is considered to show a contribution of the base line fluctuations caused by the high counting rate in the amplifiers used.

3-2-4. Particle identification

Throughout the experiments, the particle identification system with two ΔE counters and a plastic E counter worked quite well in separating light ions up to ^{6}He particles. The upper part of Fig. 3-12 shows an example of two dimensional distribution of the particles coming from a thick aluminium target in the ΔE versus E plane. In the lower part of Fig. 3-12, calculated distribution of the different particles according to the two basic equations

$$\Delta E \propto mz^2/E,$$

and

$$E = z^2(B\rho)^2/2m,$$

are plotted for p, d, t, ^{3}He and α particles as a reference.

The most severe test performed was in the separation of tritons from a large number of deuterons in a ^{3}He induced reaction as shown in Fig. 3-13. The magnetic field strength was adjusted at an excitation region where deuterons formed strong peaks in the position spectra. By carefully adjusting the gates of the ΔE and E counters, the deuteron reduction factor of much larger than 5×10^{3} was obtained. In such an experiment, the dual structure of the ΔE counter was of considerable help in reducing accidental coincidences induced by the fluctuations of the ΔE signals in the gas counters.

3-2-5. Summary and example of a spectrum

The present 1 m long position counter (IWPC) performed well in a focal plane counter system of a magnetic

spectrograph. The counter employs the multi-anode design (MAPC), after the work of Iwatani et al., to achieve high position resolution, and induction grids (sense wires) for position readout to realize a fast rise in the output pulses, with the latter being especially important in a long counter. The rise time observed was about 0.8 μs which is even shorter than that obtained in an MAPC of much shorter length. As a consequence of this, the IWPC was successful in eliminating the resolution degrading effect due to the pile-up of the position pulses at a high total counting rate of up to 25 kHz. It is to be noted that the advantages of the multi-anode design in realizing good resolution, and of the charge division technique in avoiding the complexity in the circuit configuration, were both retained in the counter. From a practical point of view, the employment of the induction wires yielded the additional advantages of facilitating the use of rather thick and strong materials for all the wires and of regulating the field distribution in the counter. We have so far experienced no trouble arising from mechanical defects in the wires or from the electrical breakdown of the counter. Rather low potential required for the sense wires also seems to be effective in reducing the probability of the circuit failure at the input stage of the preamplifier.

Many reactions have been studied in the experiments using this counter on the focal line of the spectrograph at RCNP. An example is presented in Fig. 3-14, which shows the

low-lying states of ^{49}Cr in the $^{50}Cr(p,d)^{49}Cr$ reaction at 55 MeV on the same target as in the test experiment. The overall resolution was 6.7 keV, corresponding to 2.8 mm FWHM for the solid angle of the spectrograph with setting of acceptance of 1.0 msr.

4. Two dimensional position counter with induction readout

4-1. Necessity for a two dimensional counter

In addition to the necessity of fast rise time of position pulses in a long position counter, another requirement has emerged from a point of view of reducing the aberrations in the spectrograph at the focal line. In a broad range spectrograph, it is generally difficult to achieve a good focussing condition at every point of the focal plane. As was discussed in Chapter 2, the term proportional to ϕ^2 caused by the kinematic aberration in vertical direction is important especially when a large acceptance angle in the vertical (ϕ) direction ($\sim\pm$50 to 70 mr) is desired. If there exists a condition that the ion optical coefficient $(y|\phi)$ and/or $(y|\delta\phi)$ are not zero, the aberration term $(x|\phi^2)$ is expected to cause a curved image like a crescent. In such a situation, it is possible to correct the aberration if the incidence positions of the particles are determined two-dimensionally.

Another important merit of the two dimensional position determination can be found in a possibility of reducing some of the background counts. For instance it is often experienced that continuous background counts increase in inelastic scattering experiments especially at forward angles of less than 10°. The detailed mechanism of the occurrence of such background is still an open problem, but it is proved that substantial part of the background counts are those caused by the slit edge scattering in the beam

line and the wall scattering of the strong elastic particles in the magnetic spectrograph[3-22]. These background particles are out of focus at the focal line of the spectrograph and therefore are expected to be distributed over the whole counter aperture. In the two dimensional display, by choosing true area where properly scattered particles are focussing, background counts out of focus may be reduced to a large extent.

4-2. Design and construction

4-2-1. 1.5 m two dimensional position counter

Design of two dimensional counter is based on the combination of the previously described IWPC with a drift counter[3-23,24] for the measurement of vertical position of an incident particle. The schematic view of this counter is shown in Fig. 3-15. The counter consists of three sections with different functions; the drift space surrounded by a negative high voltage electrode (drift plate) and field shaping wires, gas amplification section near anodes and the resistive electrodes for position readout using the signals induced by the anodes.

The vertical incidence position of a particle is known by the drift time measurement. In the decision of the arrangement of potential shaping wires, care has been taken to shape the potential distribution in the drift space homogeneously. In Fig. 3-16 are shown the equi-potential lines inside the two dimensional counter under typical

working conditions. The equi-potential lines at the drift space are parallel and equally spaced, which ensures that ionized electrons drift with an equal velocity. Fast pulses from the plastic E counter placed behind the position counter are used for the start pulses of the drift-time measurement and for the stop pulses, voltage signals from the anodes are used. Since low resistive wires can be used for the anodes in the induction readout counter, a rise time of less than 20 ns is achieved for the stop timing signals from anodes.

There are six anodes in the counter (see Fig. 3-16). Among these, the first and last ones, where the field is less uniform, are replaced by thick wires (120 μm) and no gas multiplication occurs on them. As the equi-potential lines are parallel in the drift space and the guard wires surrounding the anodes are grounded, four thin (50 μm) anodes are expected to behave as a stack of independent thin counters with a thickness of less than 6 mm (the distance between anodes). This arrangement, therefore, satisfies the requirement for the "multi anode design" which is essential for achieving good resolution for the non-normal incidence of particles.

For the position readout using charge division method, newly developed resistive plate[3-25] is used instead of the induction resistive wires (sense wires). Twenty resistive strips of metalglaze (each 2 mm wide) are sintered on a glass plate. The resistivity of each strip is adjusted to

around 100 Ω/mm. This low resistivity gives the possibility for getting fast rise time (∿0.5 μsec) of the position pulses for the counter length of 1.5 m and still high enough for the charge division to be performed correctly. The end part of the resistive strips are displaced just as in the IWPC to match the inclined incidence of the particles.

In the arrangement shown in Fig. 3-16, the amount of capacitance between a resistive strip and the wires as well as the walls of the counter contributes quite a lot for the rise time value of the position pulses. The results of electrostatic calculation shows that a 20 mm separation of this glass plate from the bottom support (metal frame) is indispensable to reduce the value of capacitance small enough for achieving rise time of around 0.5 μsec for a counter length of 1.5 m.

4-2-2. Electronic circuit and data acquisition system

The schematic view of the electronic circuit is shown in Fig. 3-17. As for the linear circuits and slow logics, mostly same system is used as the 1 m long IWPC. In this counter system, important role is played by the three fast pulses. They are fast pulses from the anodes of the position counter, summed dynode pulses from the photomultipliers attached to a plastic E counter and the RF signals obtained from the oscillation system of the cyclotron. The time difference between the anode signal from the position counter and the dynode signal is used for the measurement of

the vertical drift time of the electron in the position counter, which is proportional to the vertical position of the incident particle. On the other hand, the time difference between the RF signal and the dynode signal is used for the measurement of the relative flight time of the scattered particles in the spectrograph.

Left and right charge informations for the position determination along the counter direction and the two kinds of TOF signals described above are recorded on a magnetic tape event by event using the computer PDP-11/40 and an interface "Raw Data Processor (RDP)"[3-21]. The position spectrum is monitored all the time on a graphic terminal. This data taking system[*1] permitted a swift data acquisition of up to about 1 kHz for a usual operation.

4-3. Operation and performance

4-3-1. Decision of operational conditions by bench tests

For the anode wires of this counter 50 μm thick low resistive Cu-Mn-Ni wires are used because of its smoothness on the surface. The low resistivity of the anodes permits us the possibility of getting fast voltage signals which are fitted for the timing signals of the drift time measurement. Since the drift velocity of the electron in the gas of 1 atm is known to be around 20 ns/mm, a rise time of the order of 10 ns is desirable to achieve a vertical position resolution of 1 mm. The property of the anode signals largely depends on the anode termination resistance R_a in Fig. 3-17.

---

*1) The main part of the data acquisition program was written by Professor H. Ogata, RCNP.

Rise time of the anode pulse was measured as a function of the termination resistance R_a using a ^{55}Fe X-ray source. The results of the measurement are shown in Fig. 3-18. Here the anode voltage was fixed at 1800 V and drift plate voltage -1400V. The values less than 50 Ω were not so effective in obtaining the faster signal perhaps because of the non-zero resistivity of the anode wires though it is small (∿1 Ω/mm). Besides this, the output signal was too small to achieve enough S/N ratio. At the value of R_a larger than 200 Ω, the rise time became too long though the obtained signal got larger. In addition it was afraid that a larger termination resistance R_a changes the properties of the induced signals on the resistive plate[3-14]. Finally we selected 50 Ω for the R_a and as a result, the rise time of less than 20 ns and pulse height of about 4 mV were achieved for the condition of the measurement shown in Fig. 3-18.

The relationship between the height of induced output signal seen after a charge sensitive preamplifier and the drift voltage placed on the drift plate was measured also using ^{55}Fe X-ray source. In the test the anode voltage of 1800 V and a gas mixture of Ar-CO_2 (5%) was used. Until -2200 V, the output pulse height increased linearly according to the increase of drift voltage as shown in Fig. 3-19. At higher voltage, however, a rapid increase of the pulse height was observed and in addition the operation became rather unstable. An optimum value of drift voltage for our

counter, therefore, seemed to be around -2000 V or the electric field strength of 900 V/cm at the drift region. It may be noted that this value is consistent with the usually recommended value of around 1000 V/cm[3-24] although this value depend largely on the gas mixture.

4-3-2. Operation in two dimensional mode

Test experiments were performed using a 65 MeV proton beam. The gas mixture used was Ar-CO_2 (5∿20%). As in the case of IWPC, elastic protons from a 370 μg/cm² thick ^{50}Cr target was used for the resolution check of this counter. The dependence of resolution on the anode voltage was measured at the drift plate voltages of -2000 V and -1500 V. As shown in Fig. 3-20, the best resolution of 2.9 channels (2 mm FWHM) was obtained for the horizontal direction at the voltage around 1770 V in both cases of the drift voltage. It should be noted that this value of resolution is comparable to the best resolution of the 1 m long IWPC.

At the voltage higher than 1780 V, some deterioration of resolution was observed, probably indicating the increase of avalanche size above this voltage. Judging from the voltage at which this phenomenon happened, it is quite probable that this effect is closely related with the space charge effect[3-26] of the positive ions around the anode wires observed in a test using ^{55}Fe, 5.9 keV X-ray. In a wire counter proportionality between the output pulse height

and the incoming electron number is lost when the anode voltage is increased and a larger gas gain is achieved. In our case, the observed pulse height distribution for the 5.9 keV X-ray seen by a multi channel pulse height analyzer showed a change in shape shown below;

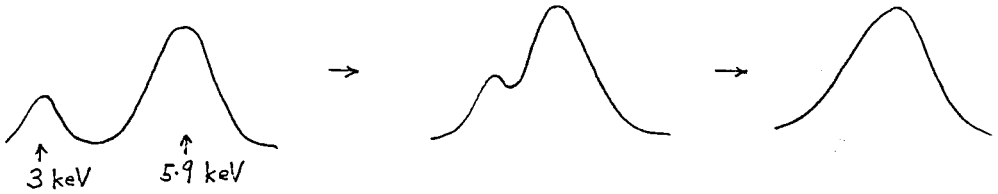

At the voltage higher than 1750 V, 5.9 keV total absorption peak and the 3.0 keV escape peak came closer i.e., the proportionality for the energy is lost and finally at the voltage higher than 1810 V, escape peak was not seen any more. As shown at the top of Fig. 3-21, the ratio of pulse heights between 5.9 keV and 3.0 keV peak began to decrease at the anode voltage of around 1750 V and the output pulse height for the 5.9 keV X-ray increased rapidly. Besides this, pulse height resolution for the 5.9 keV X-ray deteriorated rapidly as seen from the figure.

This deterioration of position resolution indicates that above the space charge limit around an anode wire, the size of the avalanche stretches along the anode wire. Recommended value of anode voltage, therefore, is around 1770 V and a higher voltage should be avoided in our case.

Spatial resolution in vertical direction was measured by putting a slit in front of the counter. The resolution of less than 1.0 mm was obtained at a drift voltage of

-2000 V. This resolution seems to be sufficient for our purpose.

As described in Section 4-2-2, two dimensional data were recorded event by event. In Fig. 3-22a, two dimensional positions of the incident particles are shown by the dots for the case of $^{50}Cr(p,d)^{49}Cr$ reaction. In the figure, each dot corresponds to one event. Also shown in Fig. 3-22b is a one dimensional projection of the same example. In this measurement the vertical acceptance angle of the spectrograph was set at ±50 mr. As is seen from the two dimensional display, the vertical curving of the image can be observed. A better resolution is expected by making a proper correction to the curved image. In Fig. 3-23, the result of correction is shown for the 0.271 MeV, $7/2^-$ peak in Fig. 3-22. When bunch of dots corresponding to this peak was projected directly to the horizontal axis, a histogram shown in the left part of Fig. 3-23 was obtained. On the other hand, when the curved image was made straight by a software before the projection, the resolution improved about 20% as shown in the right part of Fig. 3-23. This example clearly indicates that it is benificial to take the position data in two dimensions when a good resolution is desired under the condition of large vertical acceptance angle of the spectrograph.

4-3-3. Reduction of background by the use of two dimensional counter

It may well be said that two dimensional display of the incidence position of the particles opens a new scope for reducing the background counts especially in the forward angle inelastic scattering experiments. As shown in Fig. 3-24b for the case of $^{48}Ca(p,p')$ experiment at 16°, scattered particles coming from the target directly are concentrating in the region around the median plane. On the other hand background particles which appear in the spectrum at 8° are found to be spreading widely over the aperture of the counter as seen in Fig. 3-24a. By taking only the particles coming to the proper central region near the median plane in the two dimensional display as true counts, the background counts can be reduced fairly well without loosing the true counts. Simple one dimensional projection of Fig. 3-24a at 8° resulted in the spectrum shown in Fig. 3-26a. The valid two dimensional gate area for the true counts was carefully decided consulting the two dimensional display of Fig. 3-24b at 16° as shown by the dotted lines. Projected spectrum with this two dimensional gate is shown in Fig. 3-26c. With this process being included, the background counts reduced to about half value of the original spectrum.

Another interesting feature about the background particles is seen from the relation between the incoming position of a particle along the focal plane and the

measurement of the flight time in the spectrograph. Usually background particles scattered inside the spectrograph arrive at the counter position on the focal line with some time delay compared with the normally scattered particles coming from the target directly. This is shown in Fig. 3-25 clearly. In the lower figure, concentrating area of these normal particles is seen in the position-time of flight display for the case of 16°. In the upper figure, which shows the spectrum at 8°, in addition to the normal particles, background particles are distributing rather widely with some delay in flight time. The true area in the position vs. time of flight display was decided consulting that of 16°. The usage of this time of flight gate was also fairly effective in reducing the background as shown in Fig. 3-26b.

In the actual use of the counter, these two gates were combined together to reduce the background counts. The obtained spectrum is shown in Fig. 3-26d. About 70% of the background counts were taken away in the case of $^{48}Ca(p,p')$ experiment at 8°. As a result of this reduction more reliable peak area could be obtained. In addition some small peaks which were masked by the background could be seen in the spectrum.

5. Summary for the position counter system

Both focal plane counters described in Section 3 and 4 are based on induction readout and charge division method. As described in Section 2, two functions of the usual resistive anode wires i.e., gas multiplication and the charge division are separated in the induction readout counters. In order to reduce the usual degradiation of resolution associated with non-normally incoming lightly ionizing particles, multi-anode design plays an important role. Introduction of the induction readout made it possible to achieve the multi-anode design even for the counter of 1 m or more by obtaining fast position signals of around 0.5 $\sim$ 1 μs from the induction grids. With this fast rise time of the position pulses, the induction readout position counters were found to endure a total counting rate of more than 30 kHz without seriously affected by the effect of pile-up.

In the two dimensional version of the induction readout counter, fast voltage pulses from the anode wires are used for the timing signal of the electron drift time measurement in the vertical direction. Since the anode wires are not resistive anymore, fast rise time of less than 20 ns is achieved for the anode pulses and these fast pulses play an important role in accurately determining the vertical incidence position of the particles. This two dimensional determination of incidence position of particles is found to be quite effective in improving the effective resolution of

the spectrum and in reducing the background counts as was mentioned in Section 4.

As a conclusion, it should be noted from the practical view point of counter usage that rather simple position counter exceeding 1 m in length have a resolution around 1 mm and endures a total counting rate of more than 30 kHz.

References

3-1 J.L.C. Ford, Jr. Nucl. Instr. and Meth. 162 (1979) 277; and refs. therein.

3-2 W.R. Kuhlmann, K.H. Lauterjung, B. Schimmer and K. Sistemich, Nucl. Instr. and Meth. 40 (1966) 118.

3-3 G.L. Miller, N. Williams, A. Senator, R. Stensgaard and J. Fischer, Nucl. Instr. and Meth. 91 (1971) 389.

3-4 J. Hough and R.W.P. Drever, Nucl. Instr. and Meth. 103 (1972) 365.

3-5 H.W. Fulbright, R.G. Markham and W.A. Lanford, Nucl. Instr. and Meth. 108 (1973) 125.

3-6 B. Saghai and P. Roussel, Nucl. Instr. and Meth. 141 (1977) 93.

3-7 K. Iwatani, H. Yokomizo, M. Tanaka, S. Kato, T. Hasegawa, H. Hasai and F. Nishiyama, Nucl. Instr. and Meth. 171 (1980) 61.

3-8 R.G. Markham and R.G.H. Robertson, Nucl. Instr. and Meth. 129 (1975) 131.

3-9 H. Ikegami, S. Morinobu, I. Katayama, M. Fujiwara, Y. Fujita and H. Ogata, RCNP Annual Report, (1976) p. 113; H. Ikegami, S. Morinobu, I. Katayama, M. Fujiwara and S. Yamabe, Nucl. Instr. and Meth. 175 (1980) 335.

3-10 G. Charpak, D. Rahm and H. Steiner, Nucl. Instr. and Meth. 80 (1970) 13.

3-11 R. Grove, K. Lee, V. Perez-Mendez and J. Sperinde, Nucl. Instr. and Meth. 89 (1970) 257.

3-12 G. Charpak and F. Sauli, Nucl. Instr. and Meth. 113 (1973) 381.

3-13 J. Fischer, H. Okuno and A.H. Walenta, Nucl. Instr. and Meth. 151 (1978) 451.

3-14 A.H. Walenta, Nucl. Instr. and Meth. 151 (1978) 461.

3-15 E. Gatti, A. Longoni, H. Okuno and P. Semenza, Nucl. Instr. and Meth. 163 (1979) 83.

3-16 S. Kalbitzer and W. Melzer, Nucl. Instr. and Meth. 56 (1967) 301.

3-17 R.B. Owen and M.L. Awcock, IEEE Trans. Nucl. Sci. NS-15(3) (1968) 290.

3-18 E. Mathieson, Nucl. Instr. and Meth. 97 (1971) 171.

3-19 Y. Fujita, M. Fujiwara, R. Yoshioka, N. Takeda, I. Katayama, T. Yamazaki, S. Morinobu and H. Ikegami, RCNP Annual Report, (1977) p. 77.

3-20 H. Matsuda and Y. Fujita, Int. J. Mass Spectrom. Ion Phys. 16 (1975) 395.

3-21 I. Katayama and H. Ogata, RCNP Annual Report, (1976) p. 153; Nucl. Instr. and Meth. 174 (1980) 295.

3-22 M. Fujiwara, I. Katayama, S. Morinobu, Y. Fujita, T. Yamazaki and H. Ikegami, RCNP Annual Report, (1978) p. 183.

3-23 G. Charpak, Ann. Rev. Nucl. Sci. 20 (1970) 195.

3-24 P. Rice-Evans, Spark, streamer, proportional, and drift chambers (Richelieu, London, 1974).

3-25 Resistive plate made by Japan Fine Chemical Co. Inc. Hiratsuka, Kanagawa 254, Japan.

3-26 R. Bosshard, J. Fischer, S. Iwata, V. Radeka, C.L. Wang and W.J. Willis, Nucl. Instr. and Meth. 130 (1975) 365.

Figure Captions

Fig. 3-1. Conceptional view of the IWPC. The resistive snese wires are placed at a distance "a" from the anodes and are mounted on an inclined frame to form an angle θ_0 to the normal. The particle beams are shown to be incident with an angle θ.

Fig. 3-2. Cross sectional view of the counter. (A) window frame; (B) aluminium bar for cathode and wire mount; (C) aluminized mylar window (9 μm); (D) anode wire; (E,G) guard wire; (F) sense wire. The teflon terminal blocks are shown by the dotted lines.

Fig. 3-3. Difference of the equi-potential line distribution is shown for the different anode and guard configuration. In the present counter (b), the cetnral anode is replaced by a guard to obtain a equal gas gain on each anode.

Fig. 3-4. Photograph of the end part of the position counter, with the entrance foil removed to show the inclined structure of the wire supports.

Fig. 3-5. Simplified block diagram of the electronic circuit used in the experiment. Abbreviations:

PA charge sensitive preamplifier; PM photomultiplier; LA linear amplifier with an active filter; LG linear gate circuit; SCA single channel pulse height analyzer; COIN slow coincidence circuit. For the CU and RDP, see text. To reduce the input impedances of the charge sensitive preamplifiers for position readout, the feedback capacitors C_f are directly connected to the sense wires.

Fig. 3-6. Data and signal flow in the data acquisition system. The data acquisition system is designed to handle data from two independent counter systems including up to four ADCs. For the detailed description see text and ref. 3-21.

Fig. 3-7. Typical output signals at the charge sensitive preamplifiers connected to the sense wires and the anode wires. The differentiation time constant of each preamplifier was 50 s.

Fig. 3-8. Result of the position linearity measurement performed for the 1 m long position counter.

Fig. 3-9. One of the best resolution data for the 65 MeV elastic protons from the ^{50}Cr target (370 $\mu g/cm^2$). Each channel corresponds to a distance of 0.5 mm along the counter.

Fig. 3-10. The deuteron spectra of the $^{50}Cr(p,d)$ reaction at 65 MeV, obtained for the different shaping time constants in the main amplifier. The two peaks correspond to the ground and first excited states in ^{49}Cr and the time constant is given at the top of each figure. The total counting rate in the position counter was 25 kHz. Each channel corresponds to a distance of 0.5 mm along the counter.

Fig. 3-11. Peak width (FWHM) versus total counting rate in the position counter. The data were obtained for the prominent peak in Fig. 3-10. The shaping time constant in the main amplifier was 1 μs. The width in mm may be obtained by multiplying a factor of 0.5 to the value in the figure.

Fig. 3-12. Example of two dimensional distribution of the particles in the ΔE-E plane. In the lower part, expected positions for the different kind of particles are plotted as a reference.

Fig. 3-13. Separtaion of tritons from a large number of deuterons. The ability of separation increased by the use of dual structure of the ΔE counter system in spite of rather large fluctuations of the height of ΔE signals in the gas counter.

Fig. 3-14. Deuteron spectrum taken in the $^{50}Cr(p,d)^{49}Cr$ reaction. The target thickness was about 370 $\mu g/cm^2$ and the solid angle of the spectrograph was set to 1 msr. Each channel corresponds to an energy interval of 2.4 keV or a distance of 1.0 mm along the focal line.

Fig. 3-15. Conceptual view of the two dimensional counter with induction readout. The end parts of the resistive strips are displaced to match the inclined incidence of the particles.

Fig. 3-16. Equi-potential lines in the two dimensional counter calculated by solving the Laplace equation at the normal working condition.

Fig. 3-17. Block diagram of the electronic circuit used for the two dimensional counter system. Abbreviations: PA charge sensitive preamplifier; PM photomultiplier; FAST-A fast linear amplifier; R.F radio frequency output from the cyclotron; DISCRI fast discriminator; MAIN-A main linear amplifier with an active filter; SCA single channel pulse height analyzer; COIN slow coincidence circuit; TAC time to analog converter; L.G linear gate circuit; ADC analog to digital converter.

Fig. 3-18. Measured rise time (open circle) and pulse height (open square) of the anode pulse as a function of the value of termination resistance (R_a).

Fig. 3-19. Drift voltage dependence of the pulse height of the induced signal. The pulse height was measured at the output of the charge sensitive preamplifier using a 5.9 keV ^{55}Fe X-ray source.

Fig. 3-20. Change of resolution as a function of anode voltage. One channel corresponds to 0.7 mm.

Fig. 3-21. The results obtained in a test using ^{55}Fe, X-ray source. The output pulse height began to increase rapidly at around the anode voltage 1750 V. At the voltage higher than this voltage, the ratio of output pulse heights between 5.9 keV and 3.0 keV escape peak decreased. This fact shows that the proportionality in the gas amplification is being lost at the higher voltage. At the same time pulse height resolution got worse drastically.

Fig. 3-22. (a) Two dimensional display of the position spectrum obtained for the $^{50}Cr(p,d)^{49}Cr$ reaction, where a rather large vertical acceptance angle of the spectrograph of ±50 mr was used. Each dot corresponds to an event. The slight curving of

the image was observed especially at the outermost part of the focal line (left part of the figure). (b) Position spectrum projected from the two dimensional display.

Fig. 3-23. Projected histogram of the two dimensional image of the 0.271 MeV lebel in Fig. 3-22. The resolution increased by about 20% in the right figure where the projection was performed after making the curved image straight.

Fig. 3-24. Normally scattered particles are concentrating to the central region of the focal plane as can be seen in the spectum of 16°. On the other hand, particles making background which are seen in the spectrum of 8° (see Fig. 3-26a) are distributing rather widely in the two dimensional display. The area surrounded by the dotted lines in Fig. (b) is thought to be the "true" area for the normally scattered particles to come.

Fig. 3-25. The relation between the flight time of the particles in the spectometer and the arrival position on the focal plane. The relative flight time is decided by measuring the time difference between the RF-signal of the oscillator system of the cyclotoron and the first signal from the

plastic E-counter. The background particles seen in the spectrum of 8° arrive at the counter with some delay compared with the normally scattered particles.

Fig. 3-26. (a) The spectrum of $^{48}Ca(p,p')$ reaction at 8° in the energy range between 7 and 11 MeV. Large amount of instrumental background can not be avoided at the forward-angle inelastic scattering experiment. (b) The background is slightly reduced using a time of flight (TOF) gate described in Fig. 3-25. (c) The background is reduced using the two dimensional gate described in Fig. 3-24. (d) Both the TOF gate and the two dimensional gate are used to reject the background. About 70% of the background counts are taken away and more reliable peak area determination is available even for small peaks.

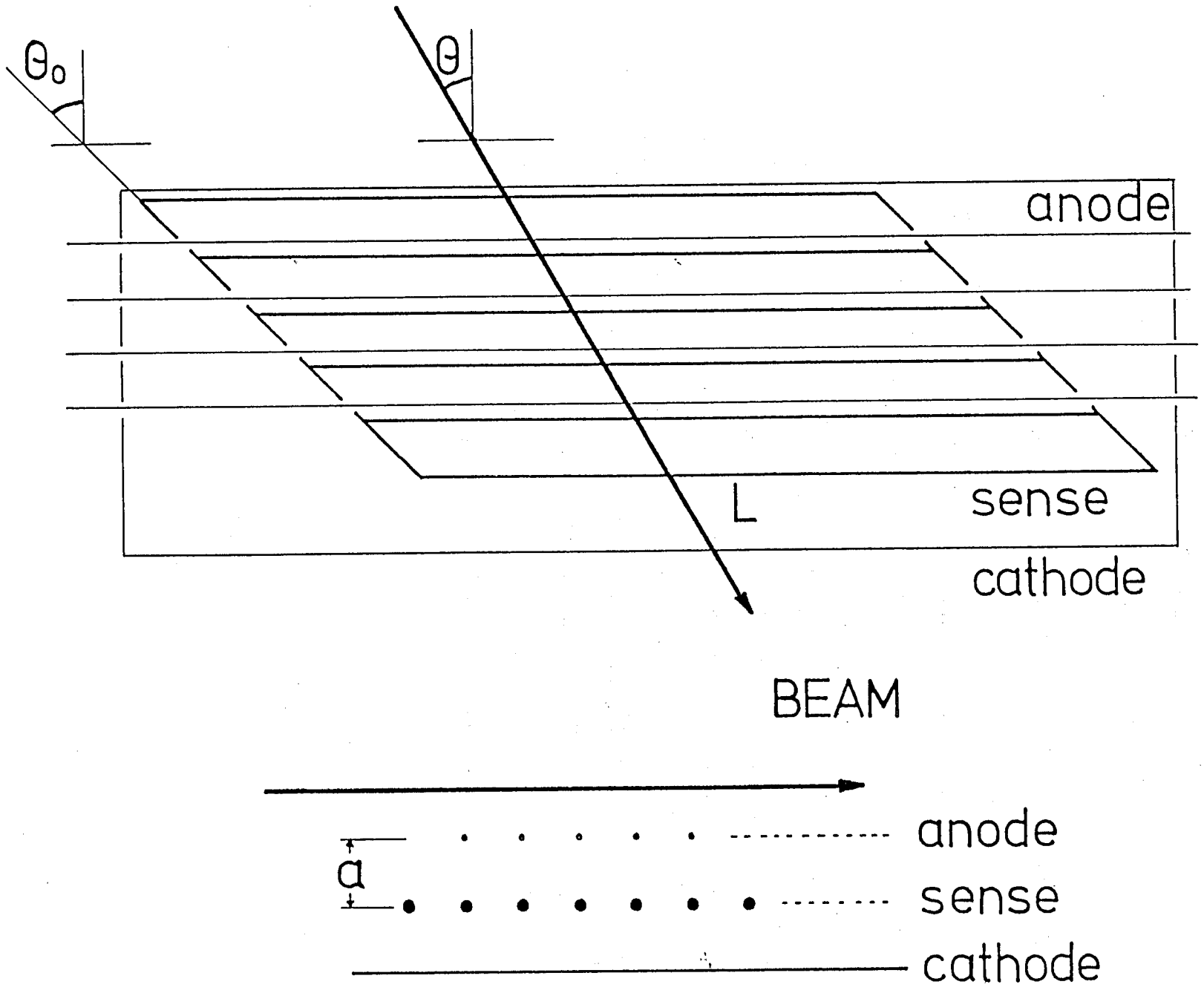

Fig. 3-1.

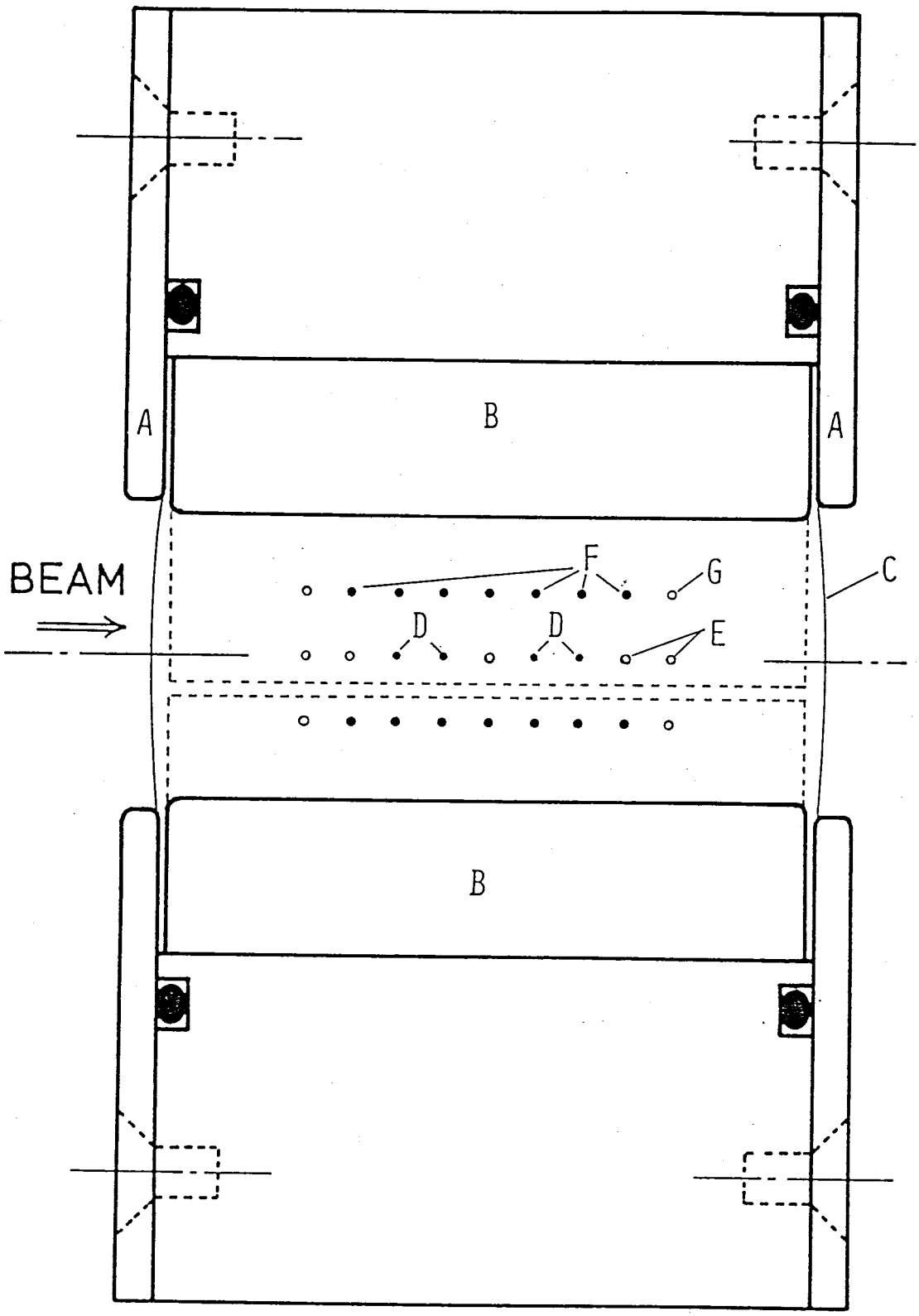

Fig. 3-2.

a) FIVE ANODES

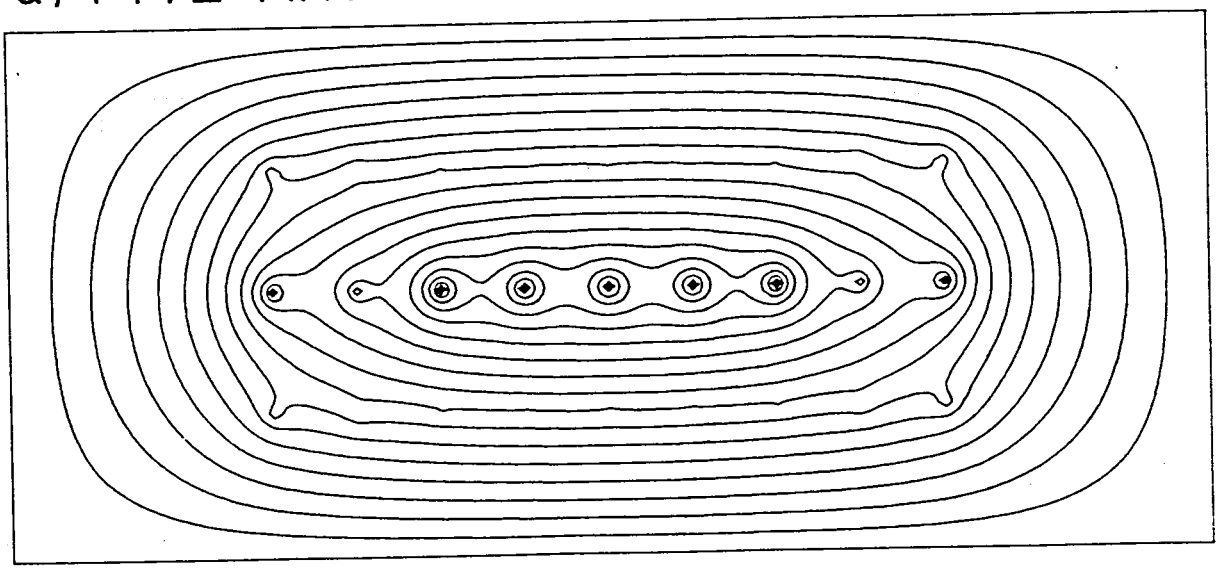

b) FOUR ANODES

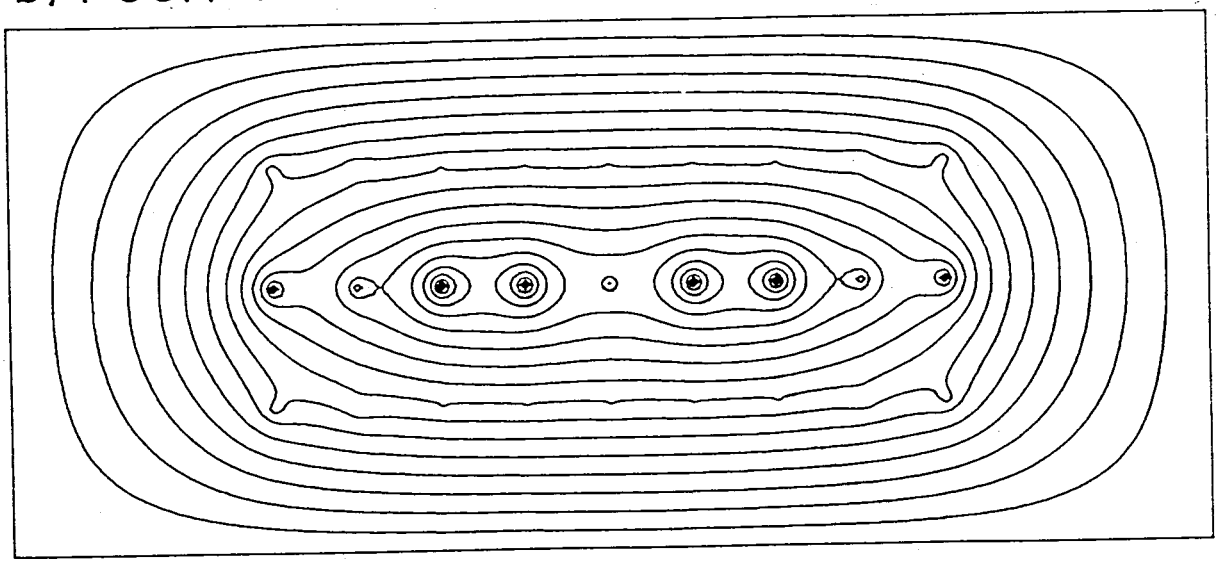

Fig. 3-3.

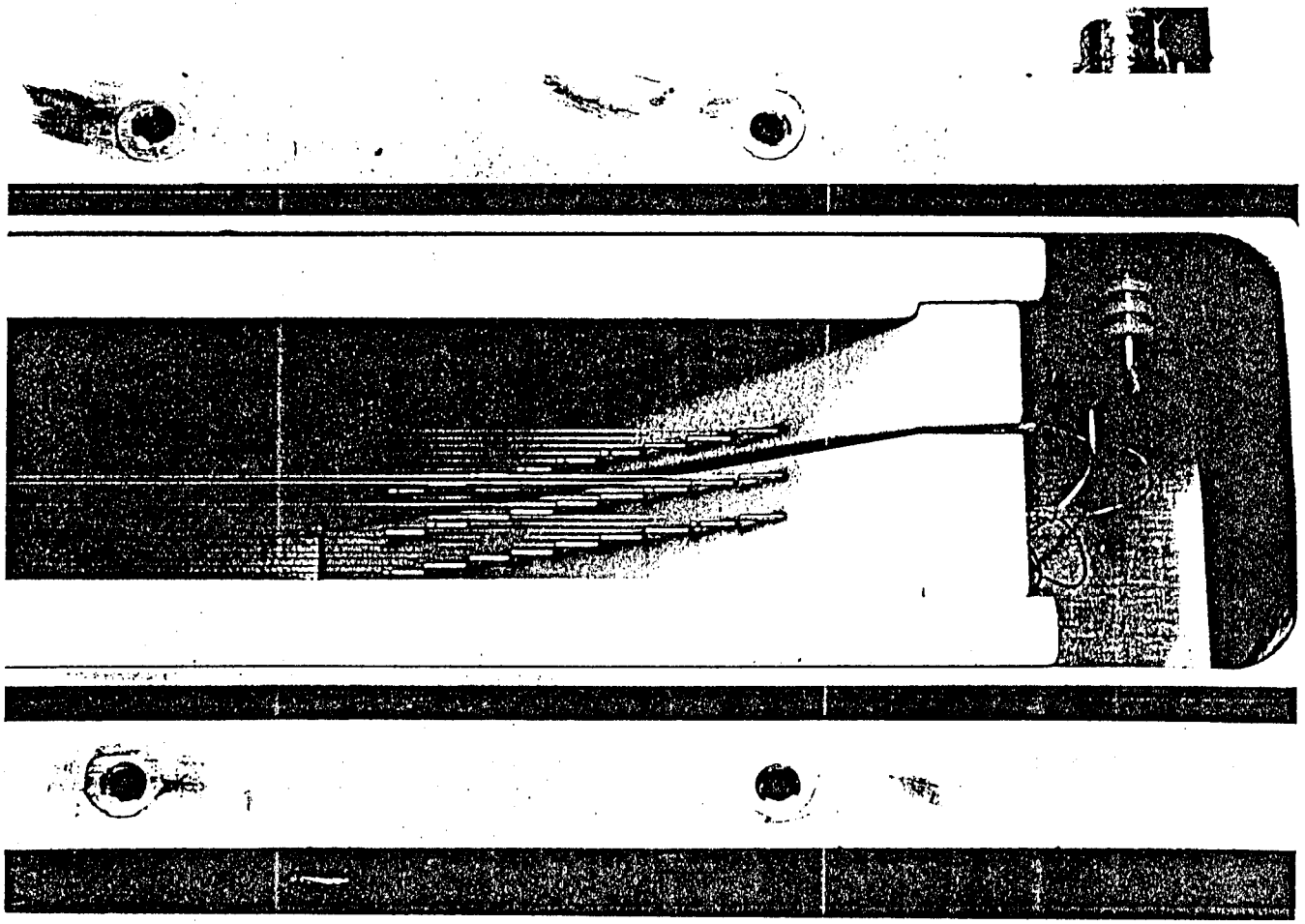

Fig. 3-4.

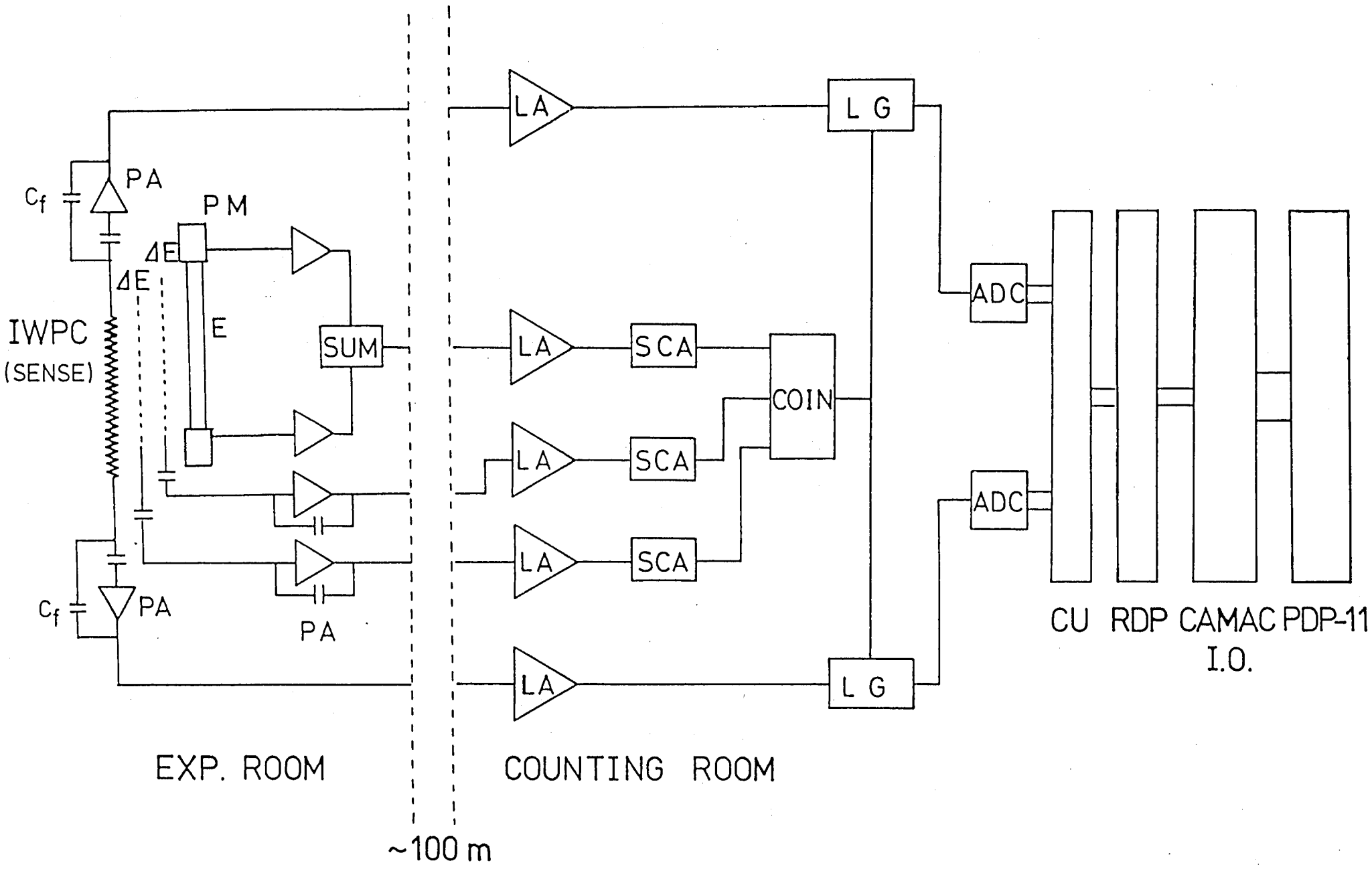
PA
Cf
PM
ΔE
ΔE
E
IWPC
(SENSE)
SUM
PA
Cf
PA
LA
LA
LA
LA
LA
SCA
SCA
SCA
COIN
LG
LG
ADC
ADC
CU
RDP
CAMAC I.O.
PDP-11
EXP. ROOM
COUNTING ROOM
~100 m

Fig. 3-5.

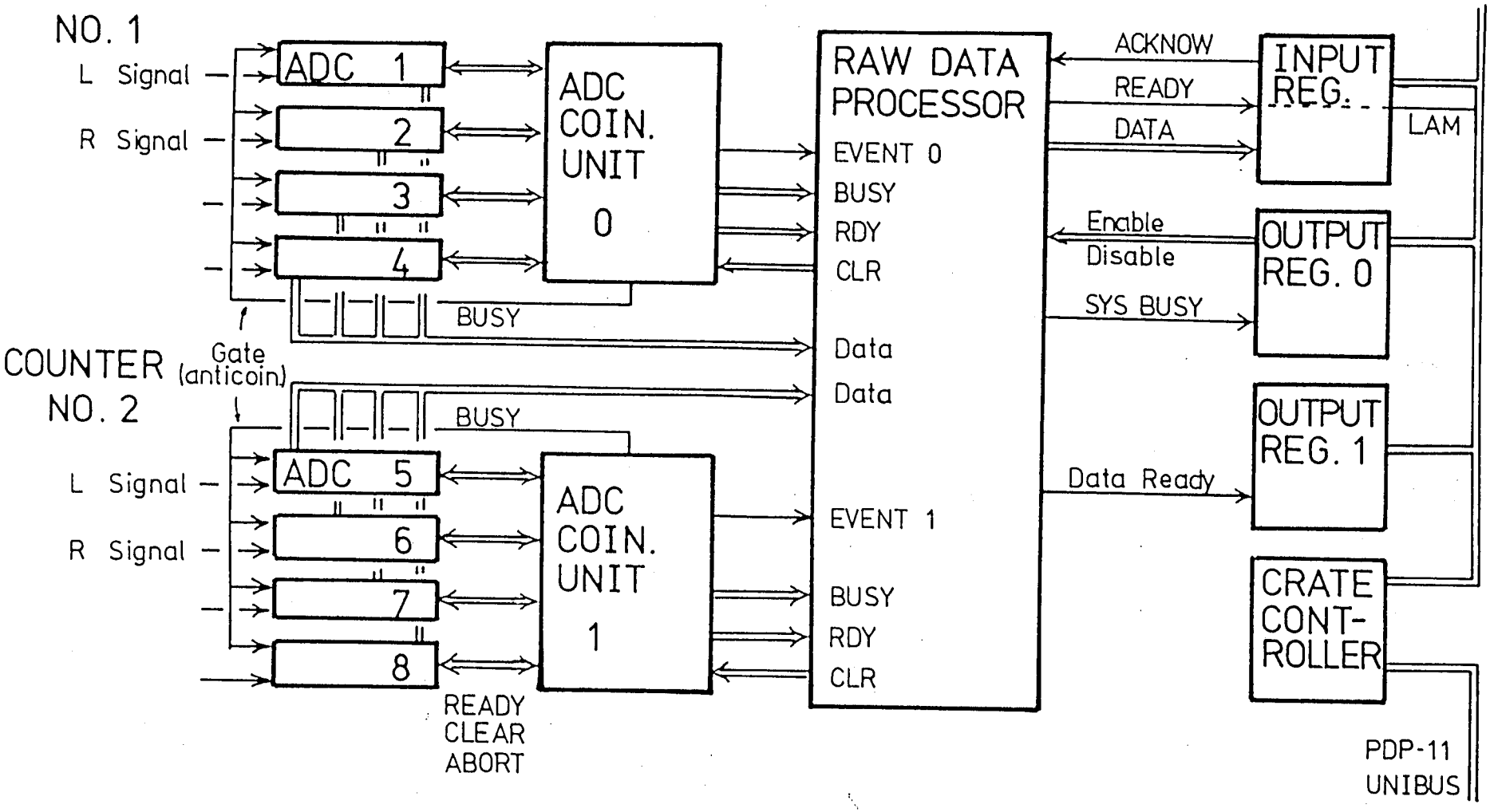
COUNTER
NO. 1
L Signal
R Signal
ADC 1
2
3
4
ADC
COIN.
UNIT
0
BUSY
Gate
(anticoin)
COUNTER
NO. 2
L Signal
R Signal
ADC 5
6
7
8
BUSY
ADC
COIN.
UNIT
1
READY
CLEAR
ABORT
RAW DATA
PROCESSOR
EVENT 0
BUSY
RDY
CLR
Data
Data
EVENT 1
BUSY
RDY
CLR
ACKNOW
READY
DATA
Enable
Disable
SYS BUSY
Data Ready
INPUT
REG.
LAM
OUTPUT
REG. 0
OUTPUT
REG. 1
CRATE
CONT-
ROLLER
PDP-11
UNIBUS

Fig. 3-6.

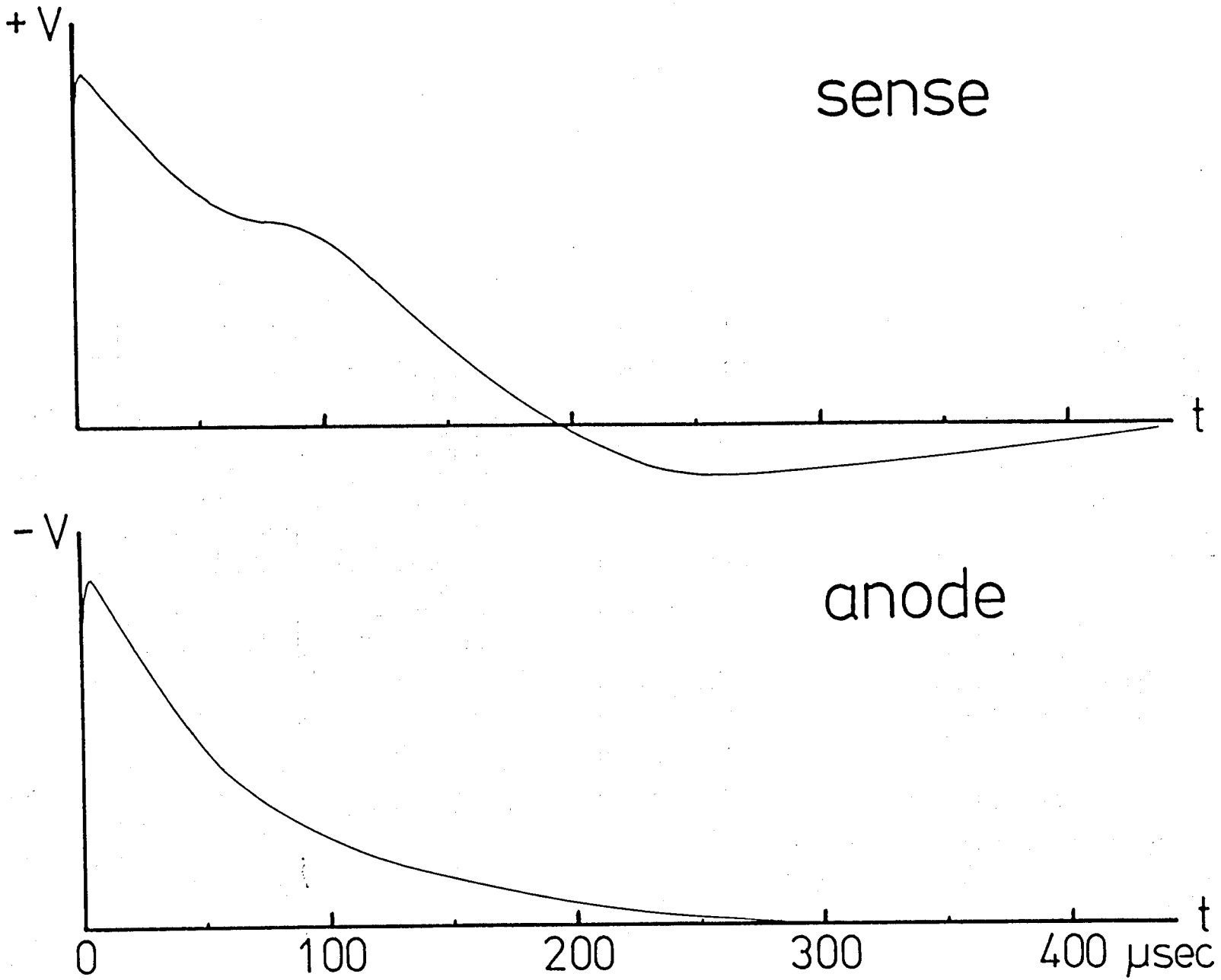

Fig. 3-7.

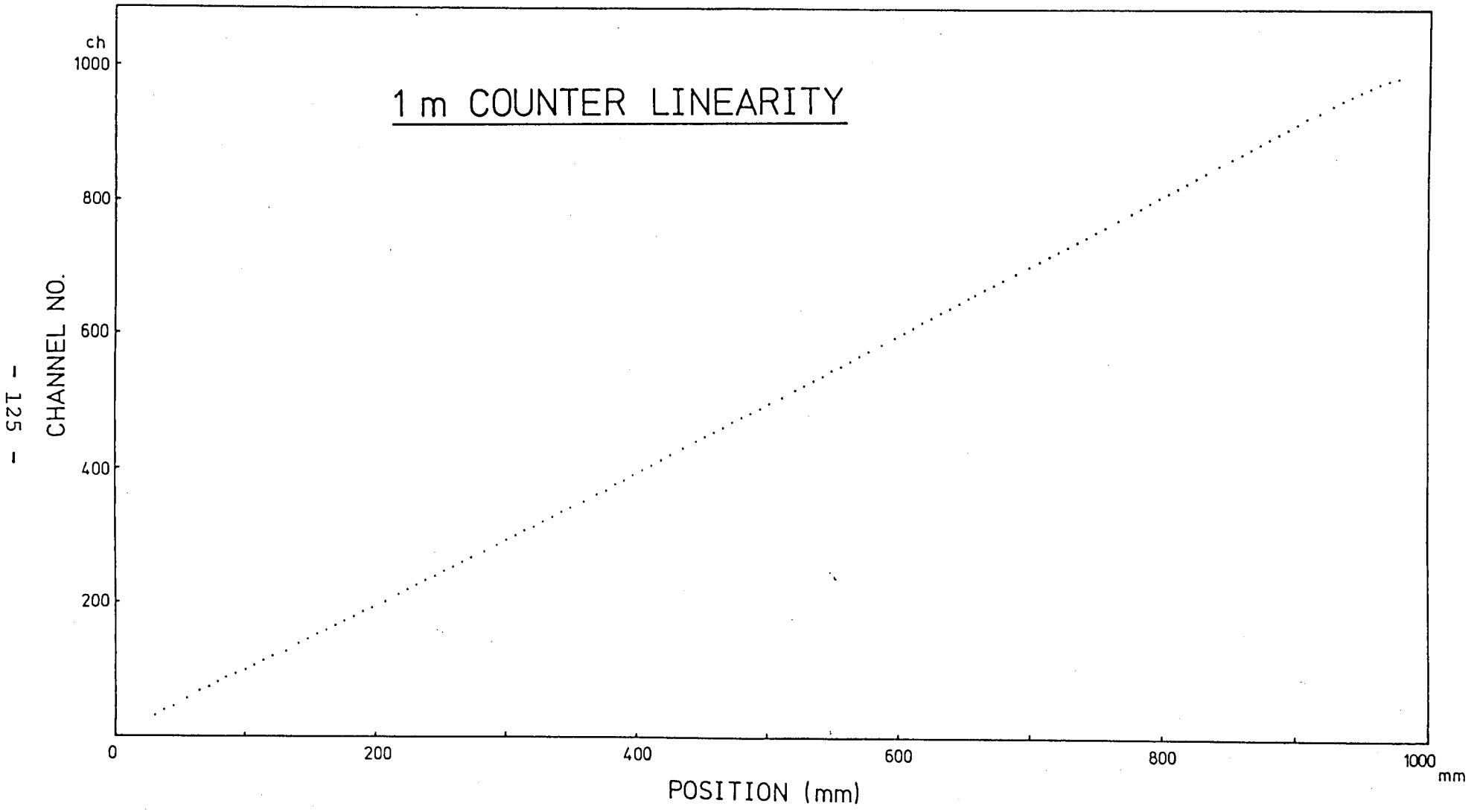
1 m COUNTER LINEARITY
ch
1000
800
600
400
200
CHANNEL NO.
0
200
400
600
800
1000
mm
POSITION (mm)

Fig. 3-8.

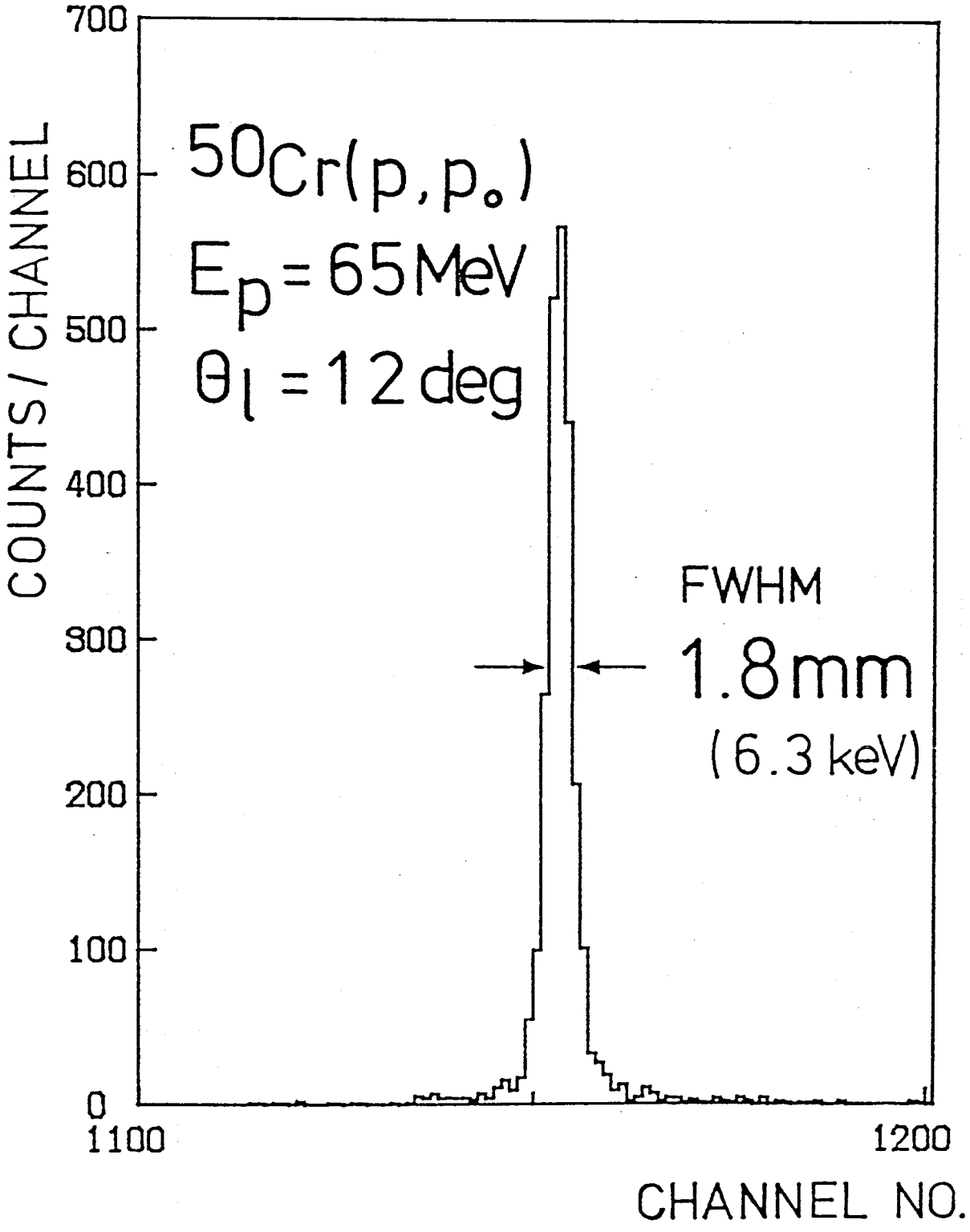
700
600
500
400
300
200
100
0
COUNTS / CHANNEL
50Cr(p,p0)
Ep = 65MeV
θl = 12 deg
FWHM
1.8mm
(6.3 keV)
1100
1200
CHANNEL NO.

Fig. 3-9.

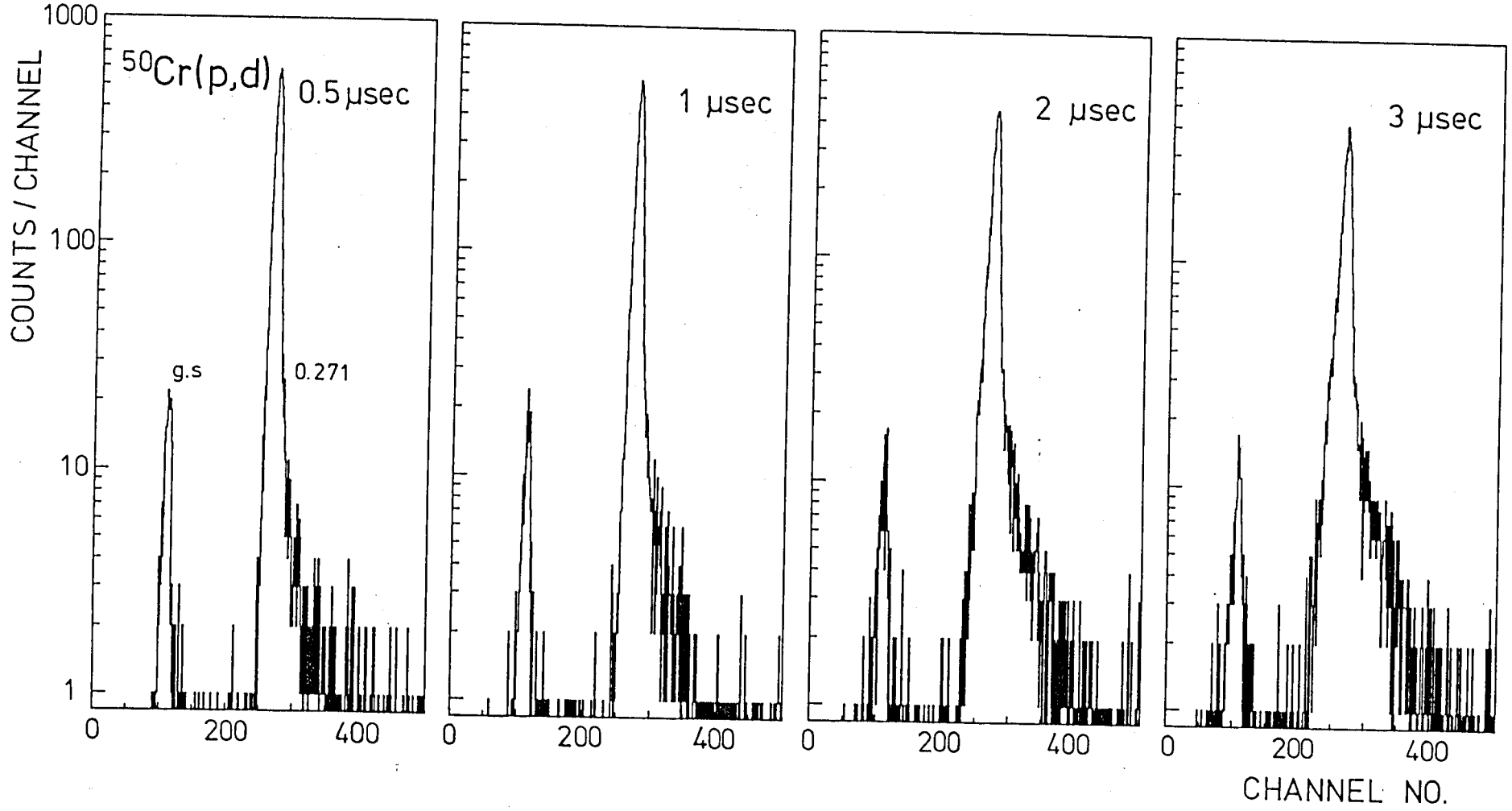
1000
100
10
1
COUNTS / CHANNEL
^{50}Cr(p,d)
0.5 μsec
g.s
0.271
1 μsec
2 μsec
3 μsec
0
200
400
CHANNEL NO.

Fig. 3-10.

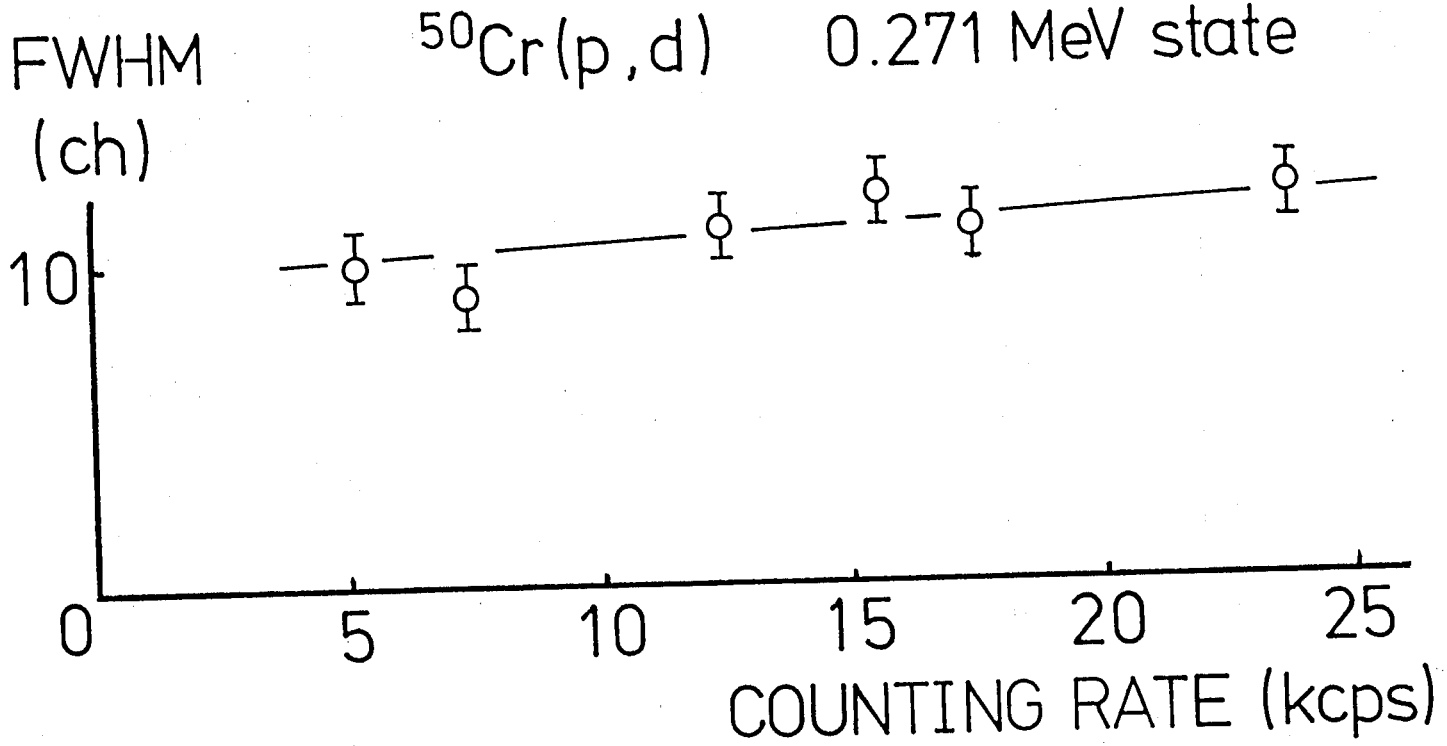
FWHM
(ch)
^{50}Cr(p,d) 0.271 MeV state
10
0
5
10
15
20
25
COUNTING RATE (kcps)

Fig. 3-11.

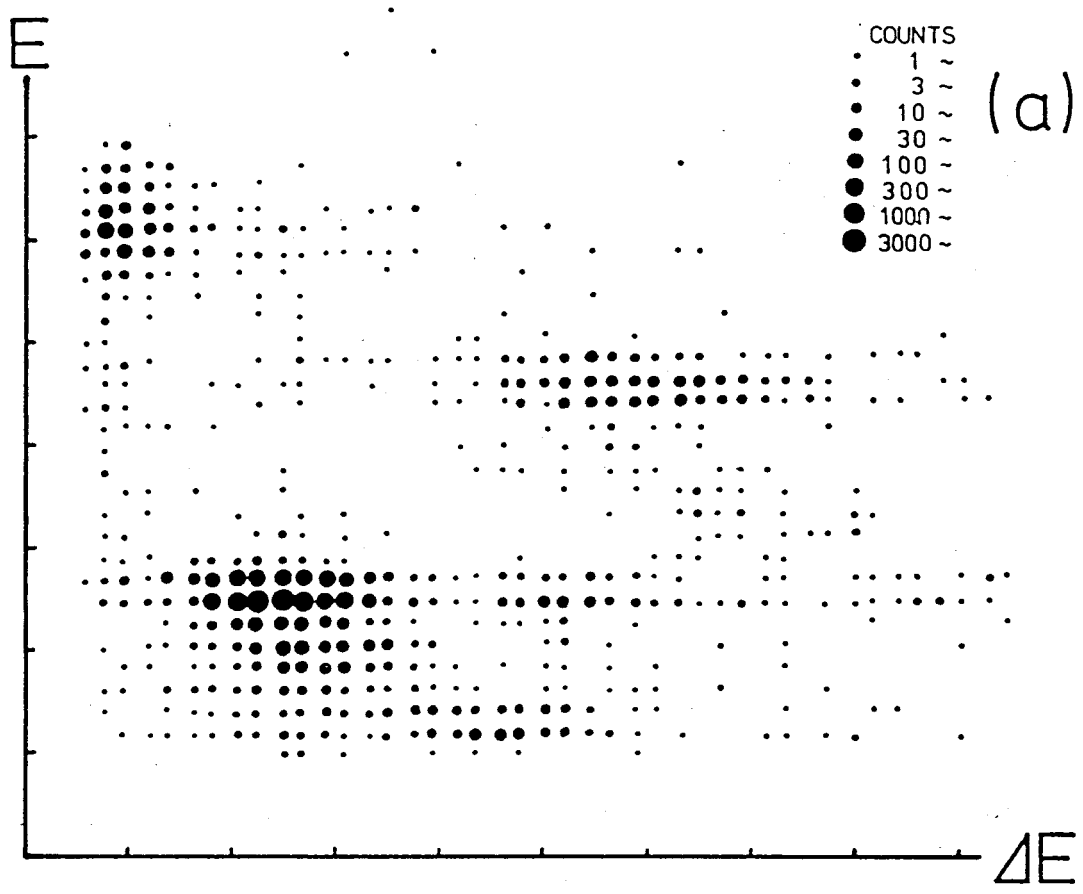

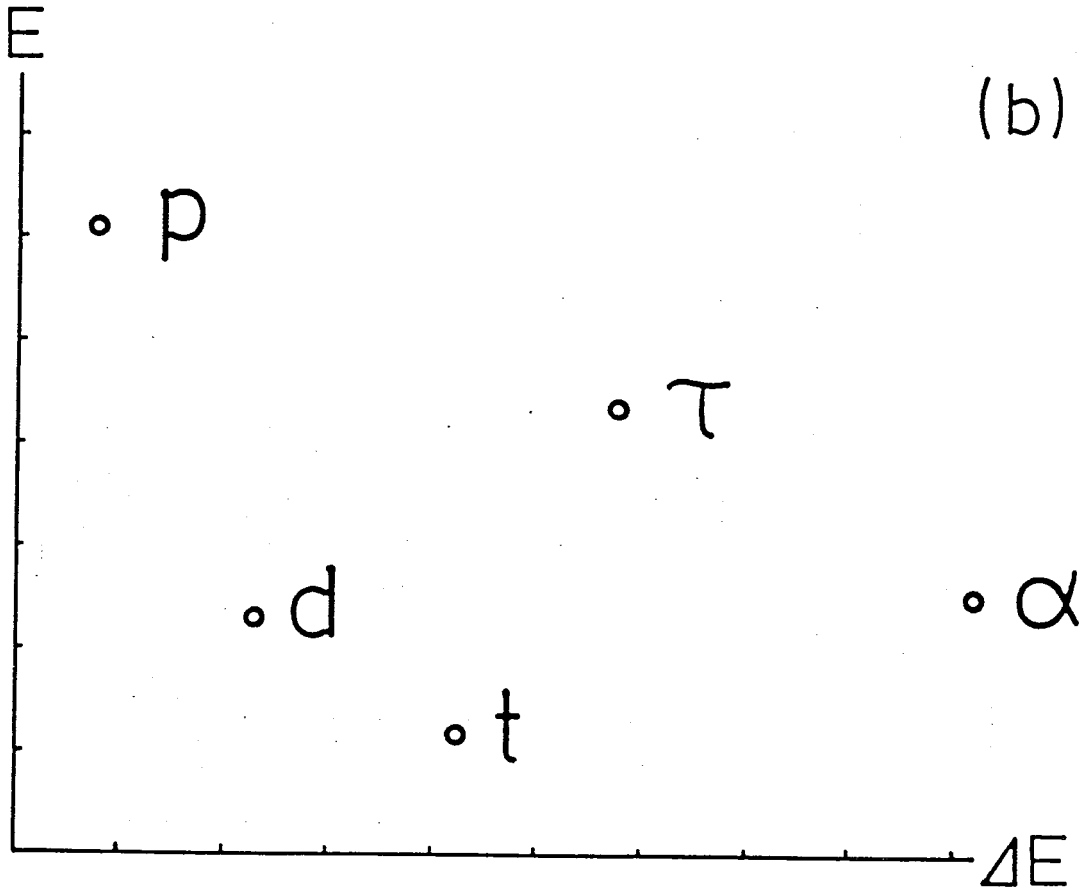

Fig. 3-12.

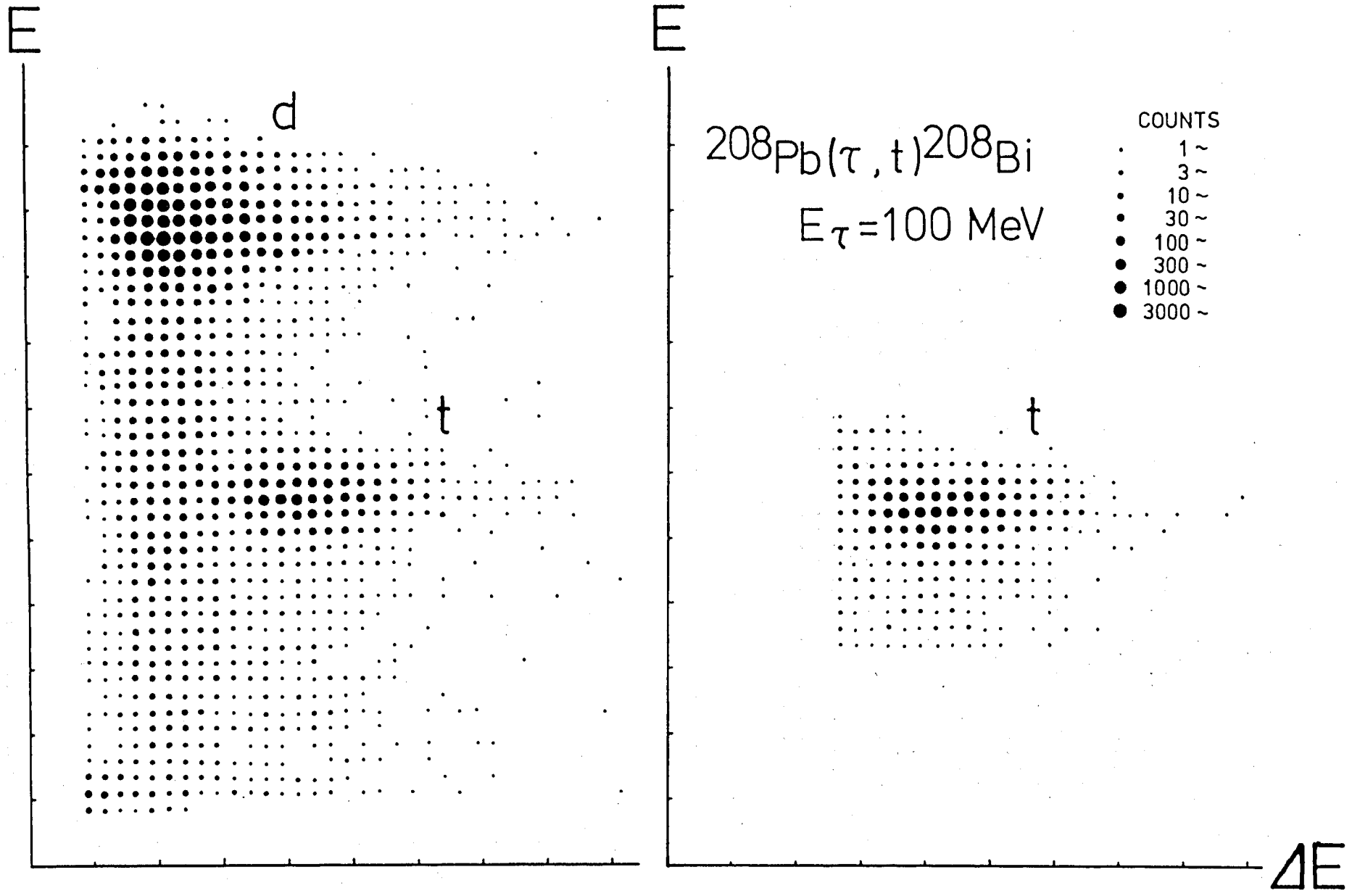
E
d
t
E
^{208}Pb(τ, t)^{208}Bi
Eτ=100 MeV
COUNTS
1 ~
3 ~
10 ~
30 ~
100 ~
300 ~
1000 ~
3000 ~
t
ΔE

Fig. 3-13.

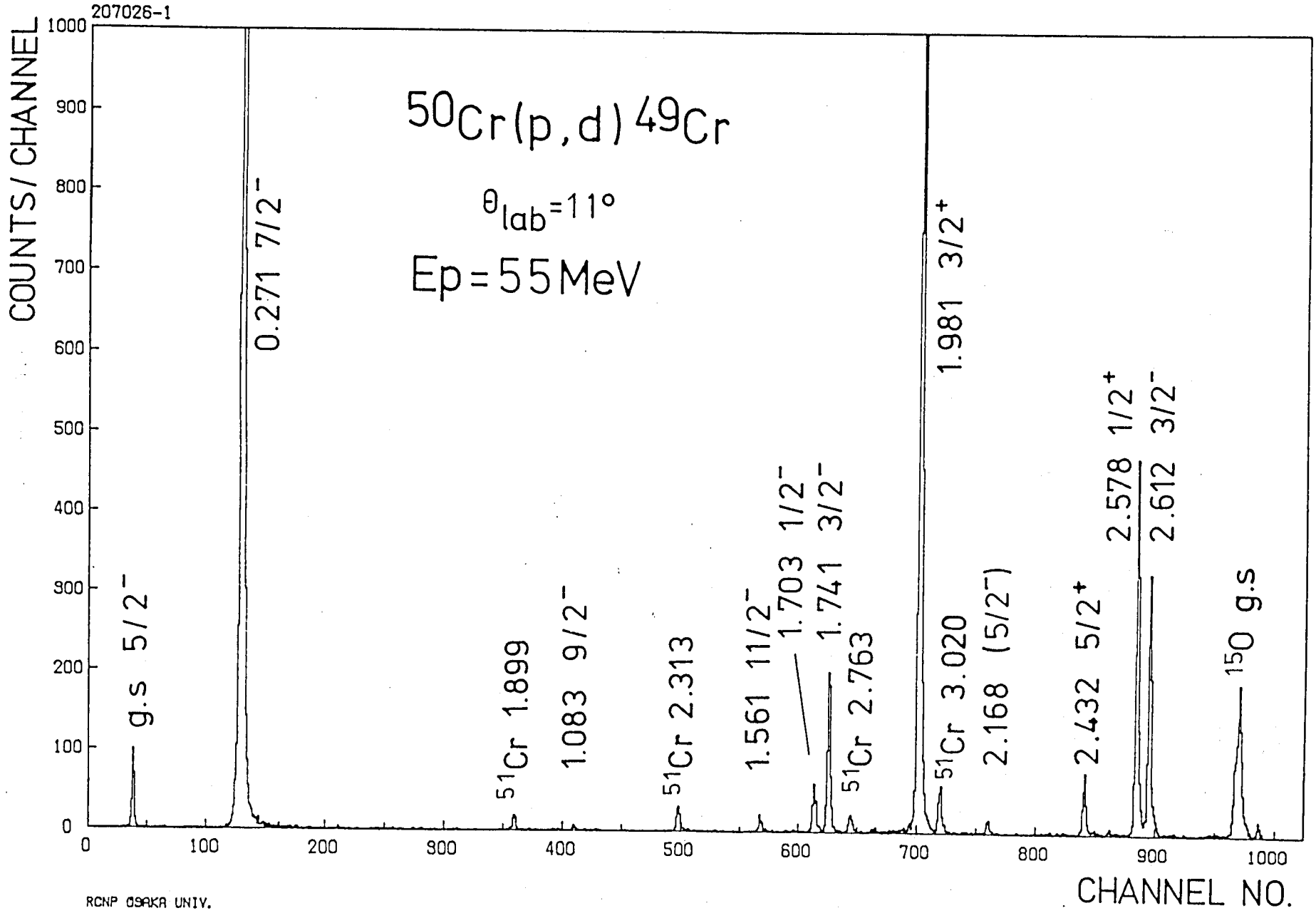
207026-1
$^{50}Cr(p,d)^{49}Cr$
$\theta_{lab}=11°$
Ep=55MeV
COUNTS/CHANNEL
CHANNEL NO.
RCNP OSAKA UNIV.
g.s 5/2⁻
0.271 7/2⁻
^{51}Cr 1.899
1.083 9/2⁻
^{51}Cr 2.313
1.561 11/2⁻
1.703 1/2⁻
1.741 3/2⁻
^{51}Cr 2.763
1.981 3/2⁺
^{51}Cr 3.020
2.168 (5/2⁻)
2.432 5/2⁺
2.578 1/2⁺
2.612 3/2⁻
^{15}O g.s

Fig. 3-14.

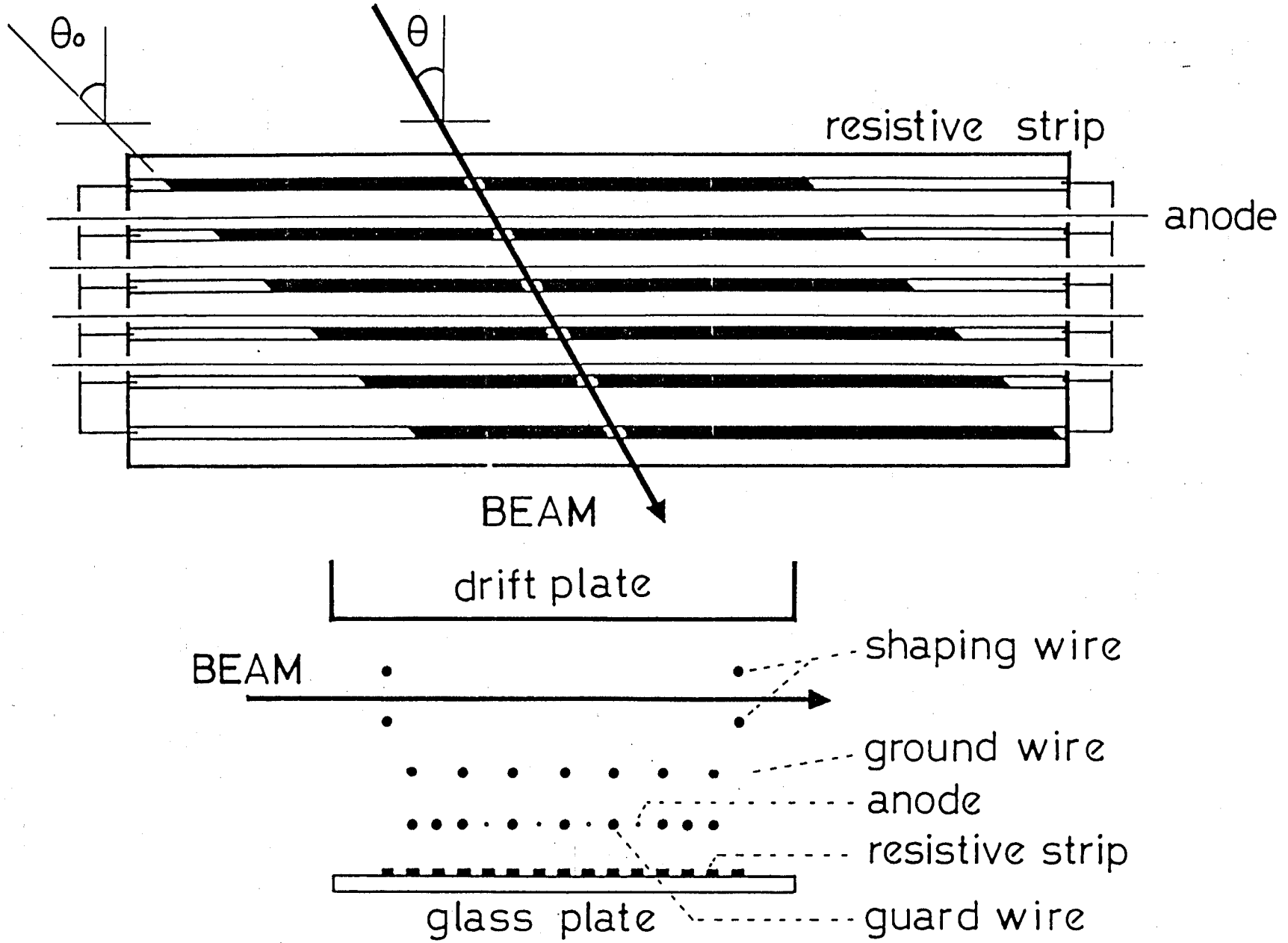
θ₀
θ
resistive strip
anode
BEAM
drift plate
BEAM
shaping wire
ground wire
anode
resistive strip
glass plate
guard wire

Fig. 3-15.

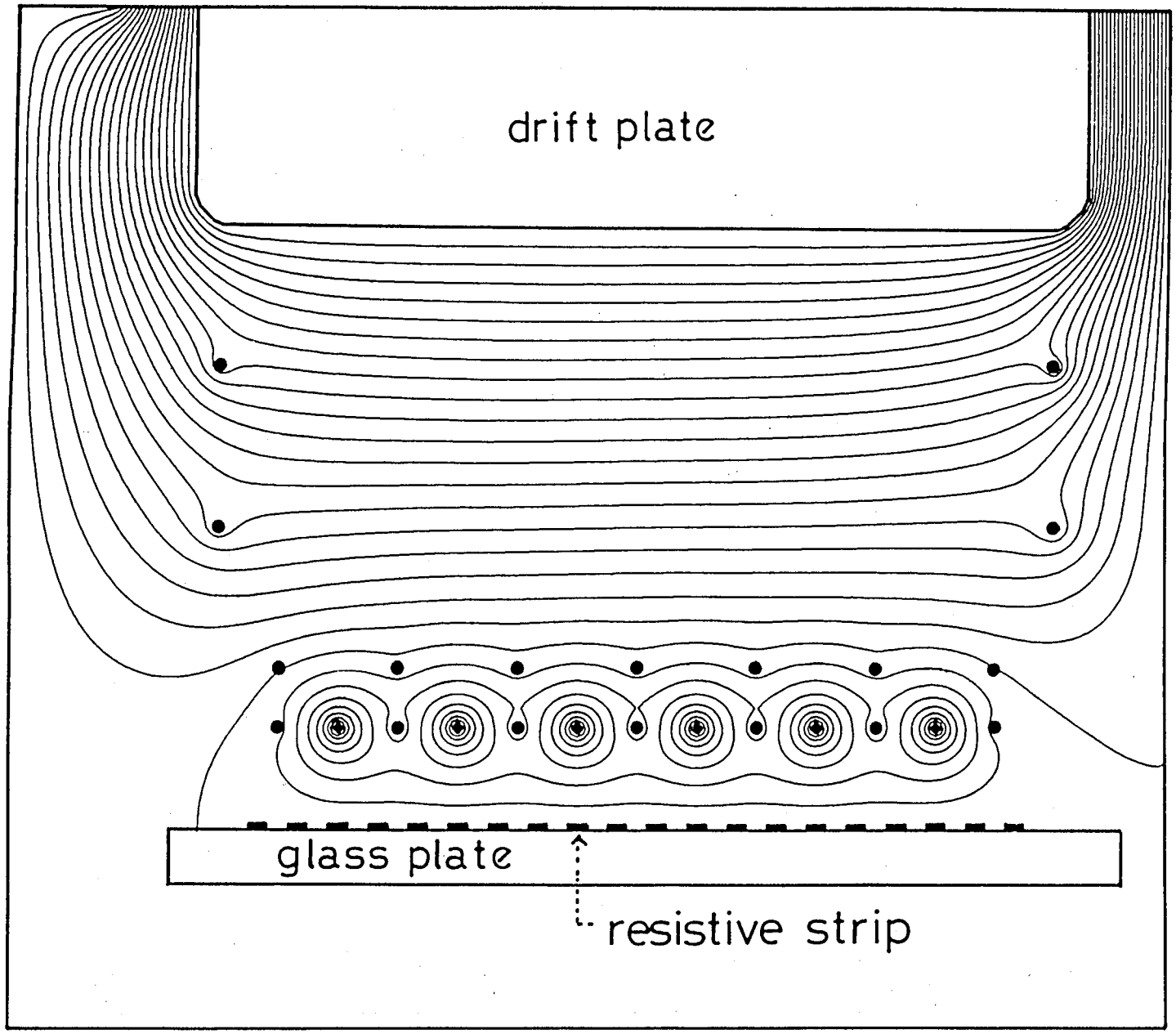

Fig. 3-16.

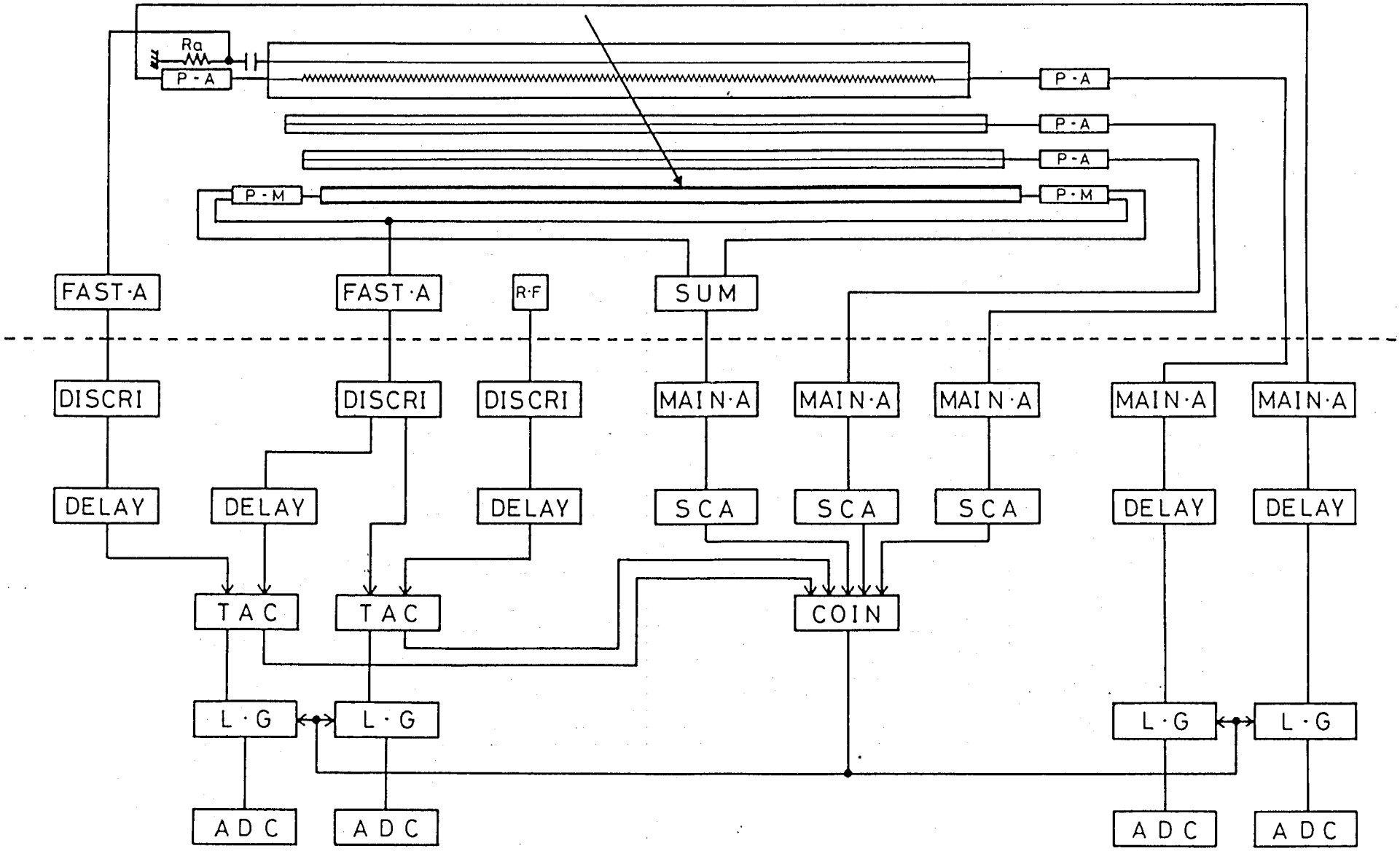
Ra
P·A
P·A
P·A
P·A
P·M
P·M
FAST·A
FAST·A
R·F
SUM
DISCRI
DISCRI
DISCRI
MAIN·A
MAIN·A
MAIN·A
MAIN·A
MAIN·A
DELAY
DELAY
DELAY
SCA
SCA
SCA
DELAY
DELAY
TAC
TAC
COIN
L·G
L·G
L·G
L·G
ADC
ADC
ADC
ADC

Fig. 3-17.

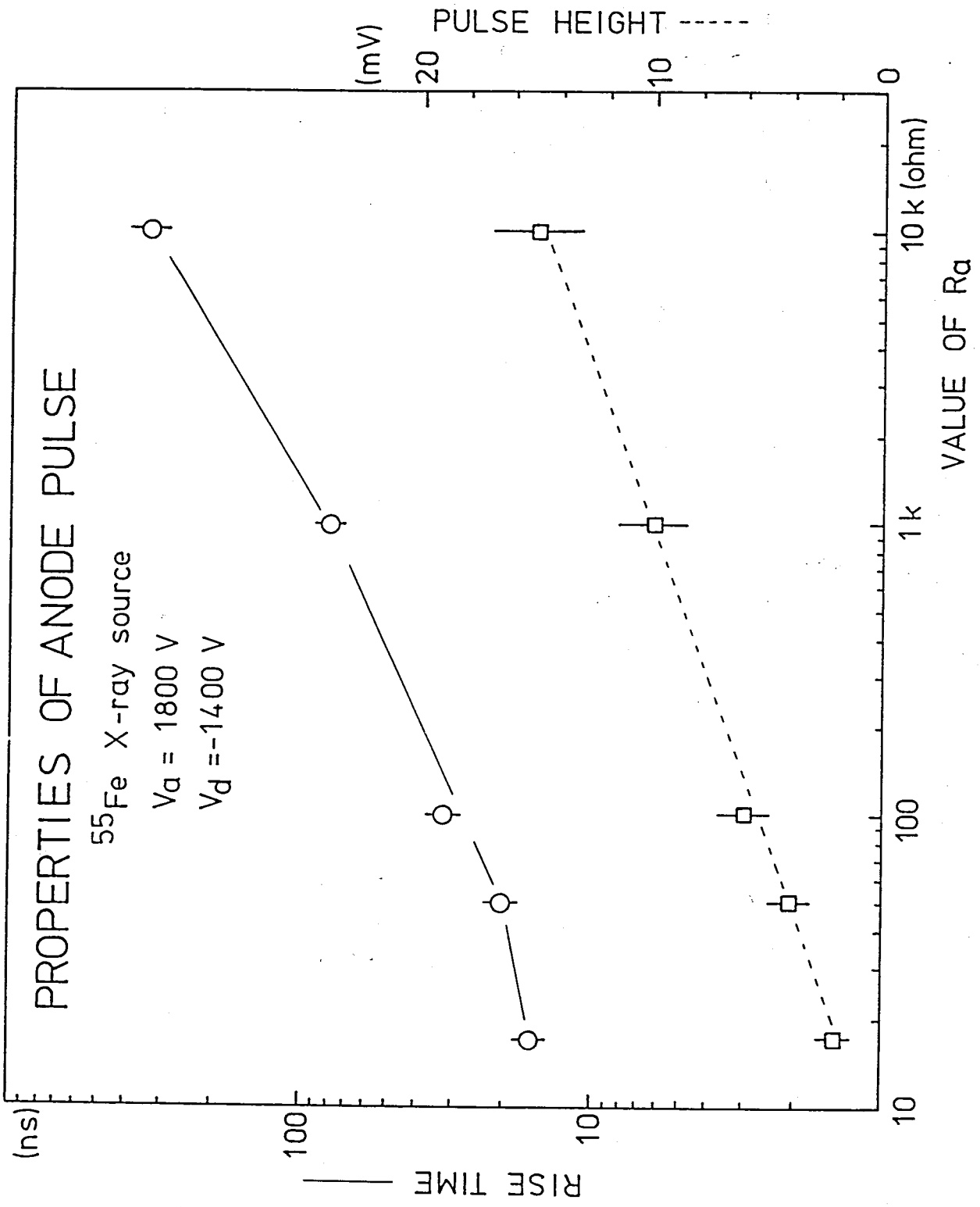
PROPERTIES OF ANODE PULSE
^{55}Fe X-ray source
V_a = 1800 V
V_d =-1400 V
PULSE HEIGHT -----
(mV)
20
10
0
RISE TIME ——
(ns)
100
10
10
100
1 k
10 k (ohm)
VALUE OF Ra

Fig. 3-18.

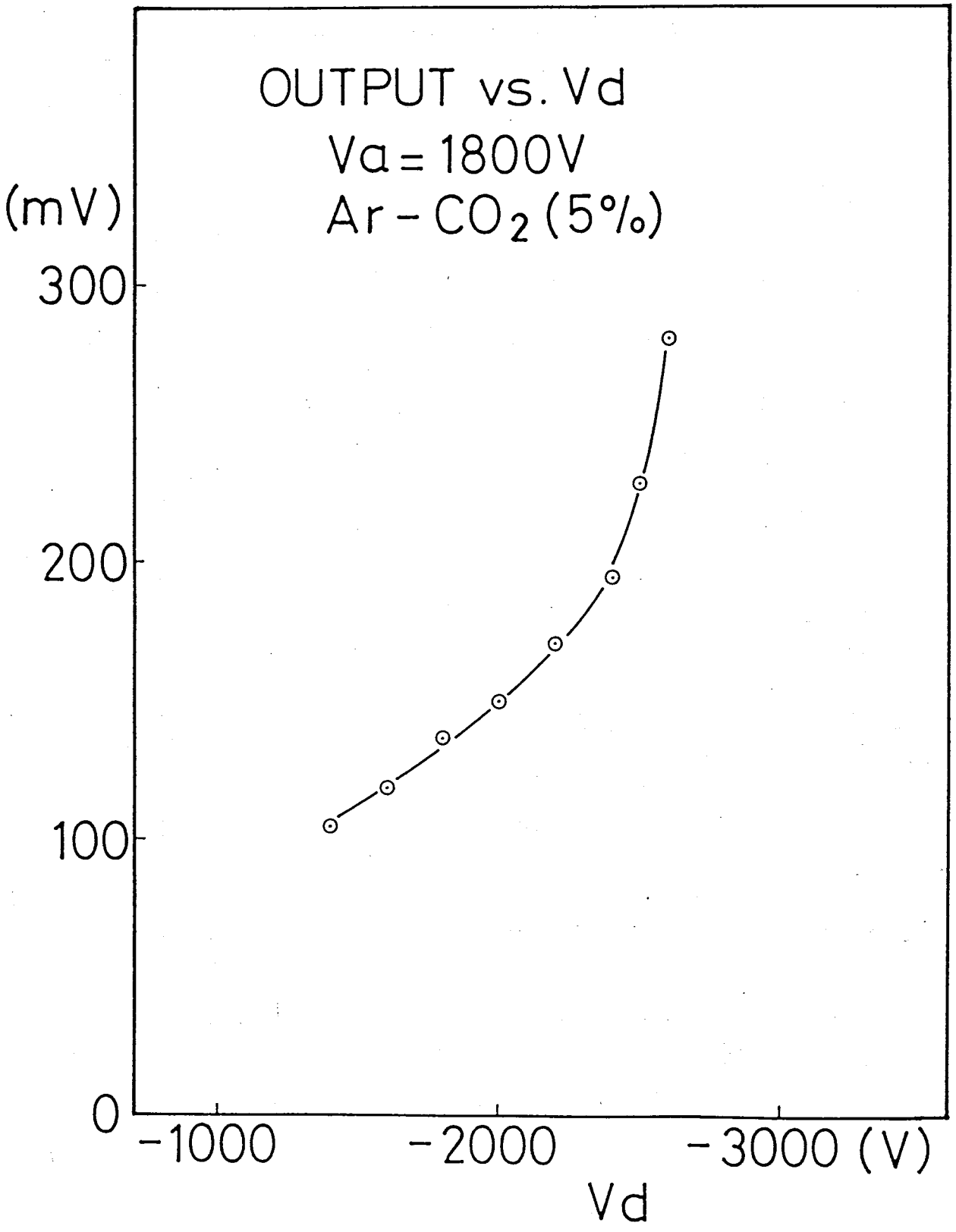
OUTPUT vs. Vd
Va = 1800V
Ar - CO2 (5%)
(mV)
300
200
100
0
-1000
-2000
-3000 (V)
Vd

Fig. 3-19.

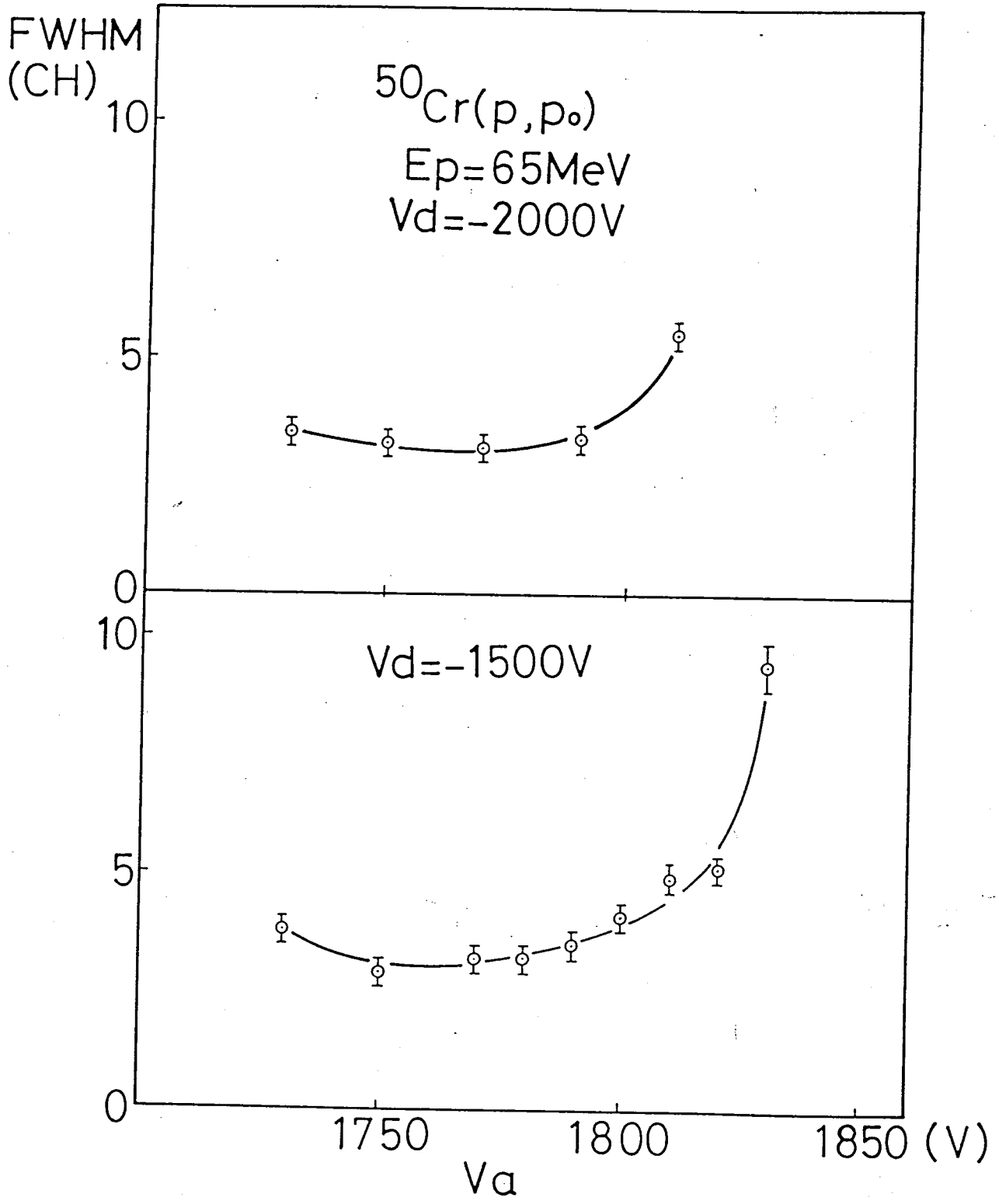
FWHM
(CH)
10
5
0
^{50}Cr(p,p$_0$)
Ep=65MeV
Vd=-2000V
10
5
0
Vd=-1500V
1750
1800
1850 (V)
Va

Fig. 3-20.

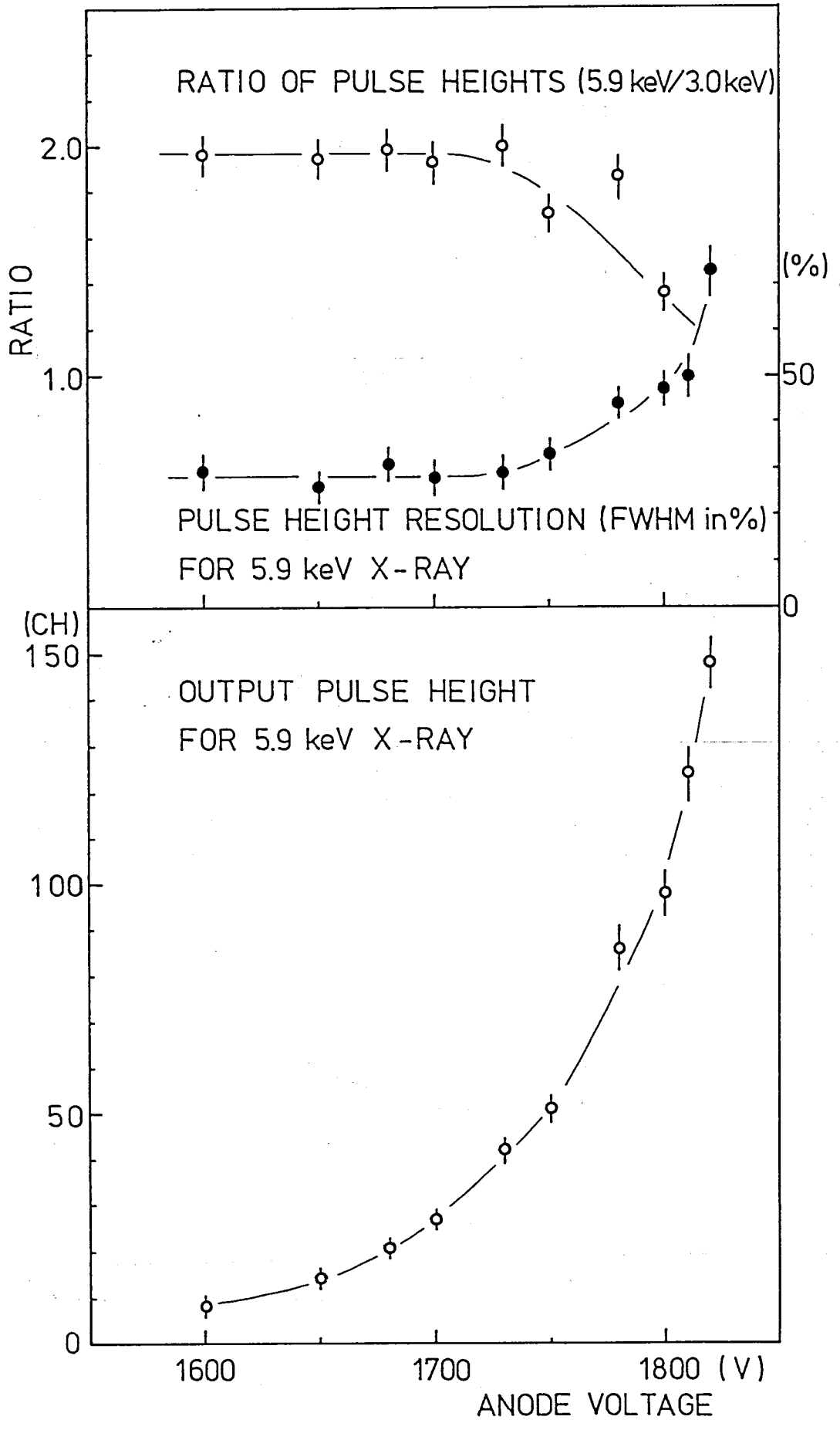
RATIO OF PULSE HEIGHTS (5.9 keV/3.0keV)
2.0
1.0
RATIO
(%)
50
0
PULSE HEIGHT RESOLUTION (FWHM in%)
FOR 5.9 keV X-RAY
(CH)
150
100
50
0
OUTPUT PULSE HEIGHT
FOR 5.9 keV X-RAY
1600
1700
1800 (V)
ANODE VOLTAGE

Fig. 3-21.

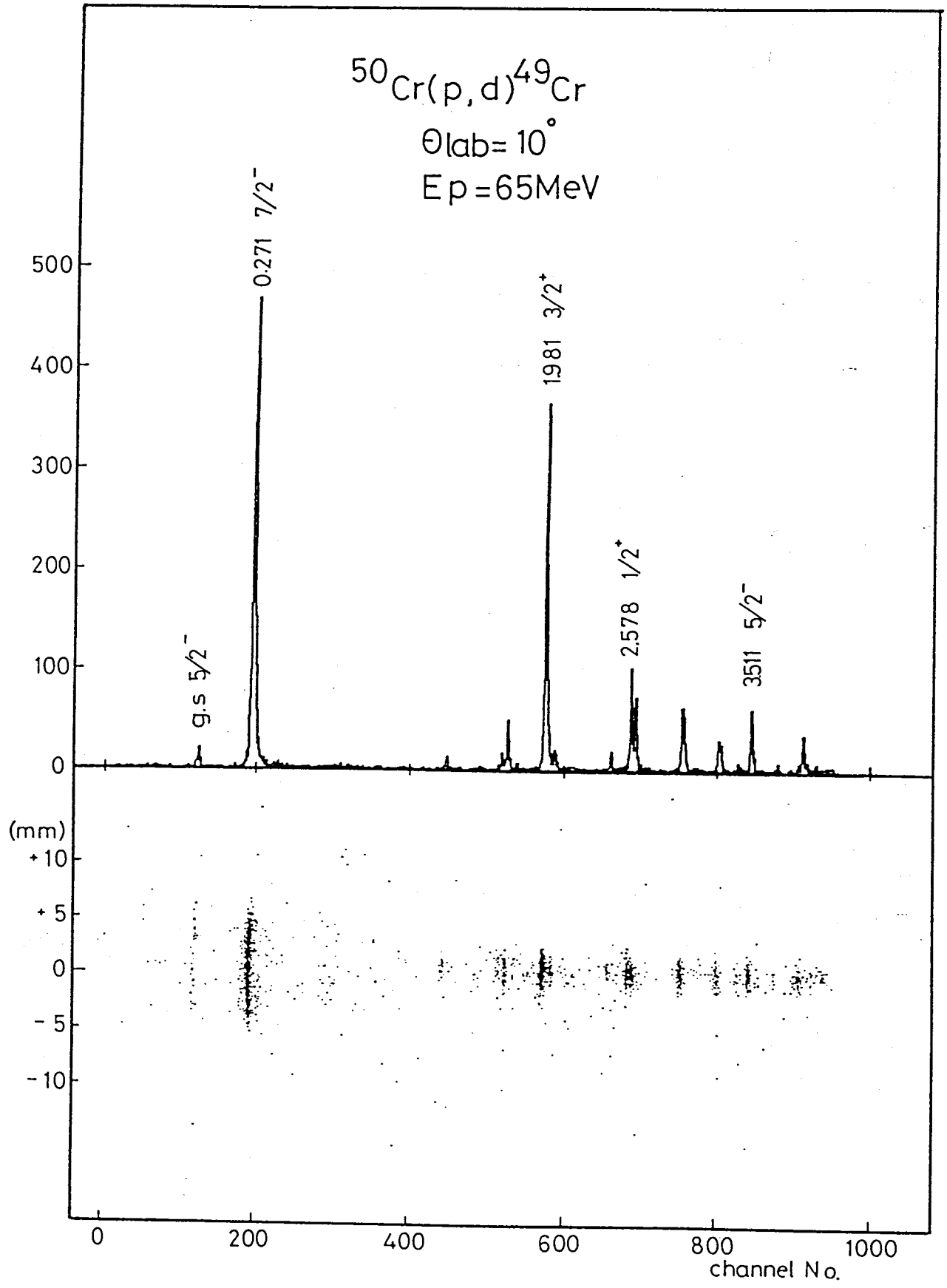
$^{50}Cr(p,d)^{49}Cr$
θlab= 10°
Ep =65MeV
g.s 5/2⁻
0.271 7/2⁻
1.981 3/2⁺
2.578 1/2⁺
3.511 5/2⁻
500
400
300
200
100
0
(mm)
+10
+5
0
-5
-10
0
200
400
600
800
1000
channel No.

Fig. 3-22.

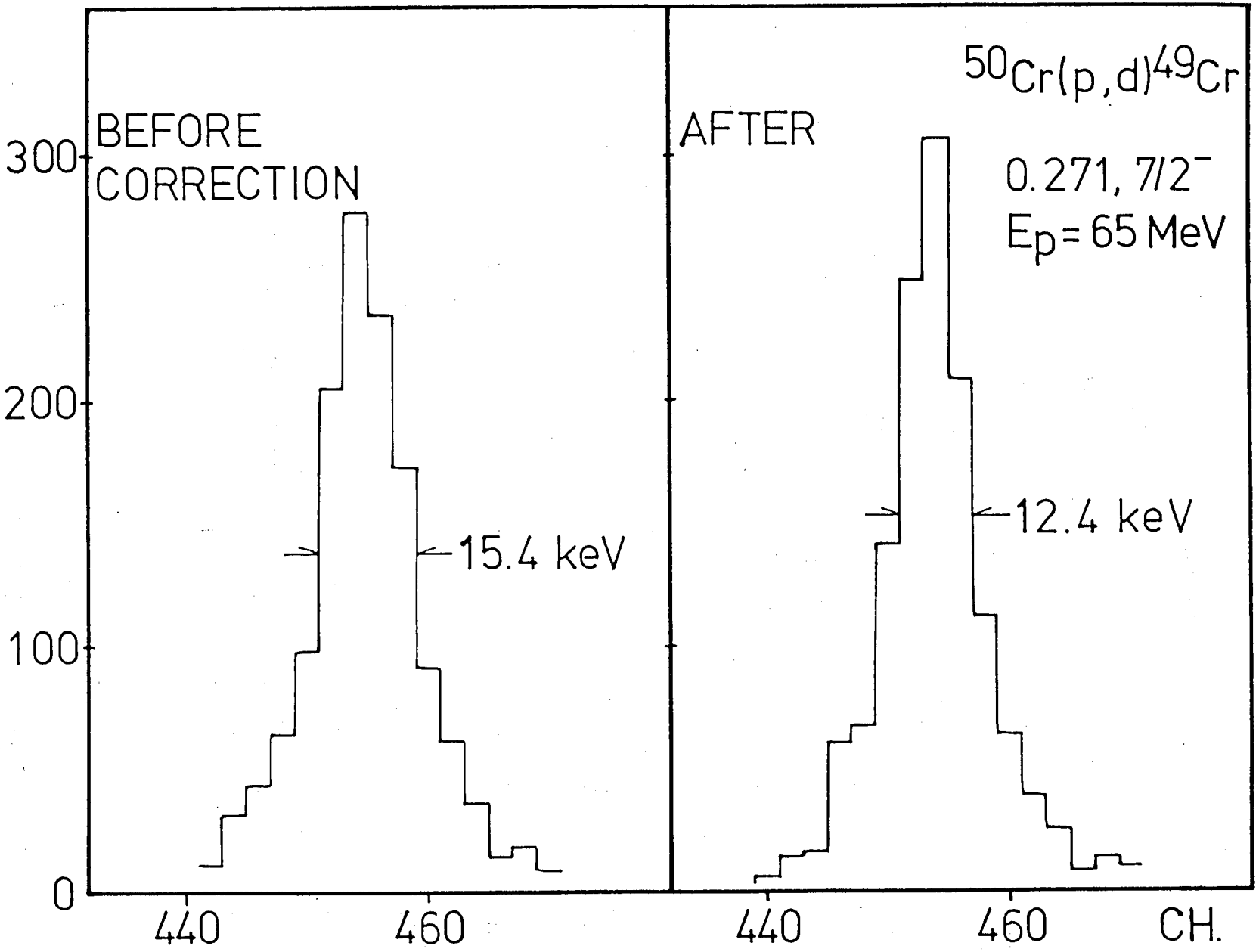
BEFORE
CORRECTION
15.4 keV
AFTER
$^{50}Cr(p,d)^{49}Cr$
0.271, 7/2⁻
E_p= 65 MeV
12.4 keV
300
200
100
0
440
460
440
460
CH.

Fig. 3-23.

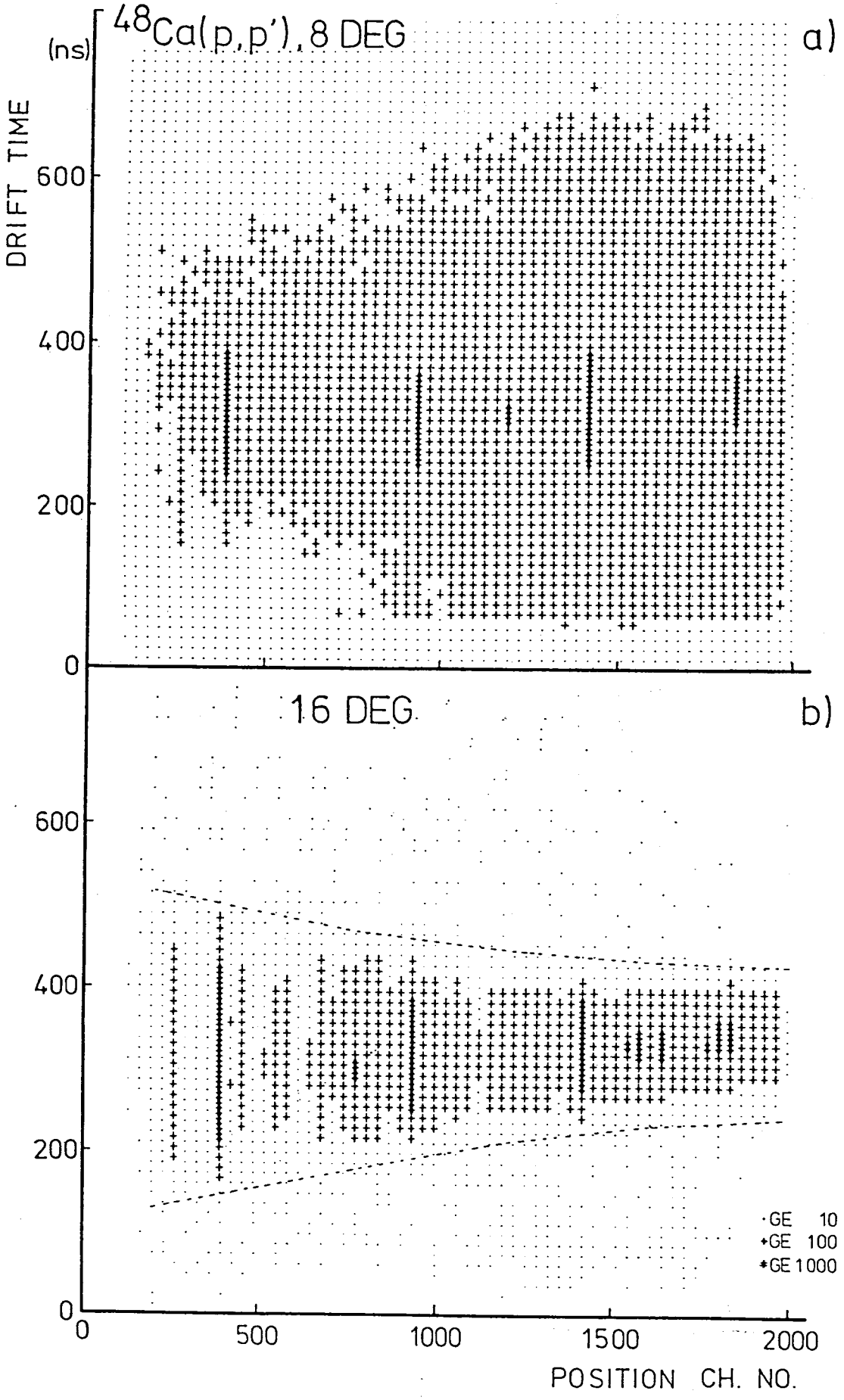
48Ca(p,p'),8 DEG
a)
(ns)
DRIFT TIME
600
400
200
0
16 DEG
b)
600
400
200
0
·GE 10
+GE 100
*GE 1000
0
500
1000
1500
2000
POSITION CH. NO.

Fig. 3-24.

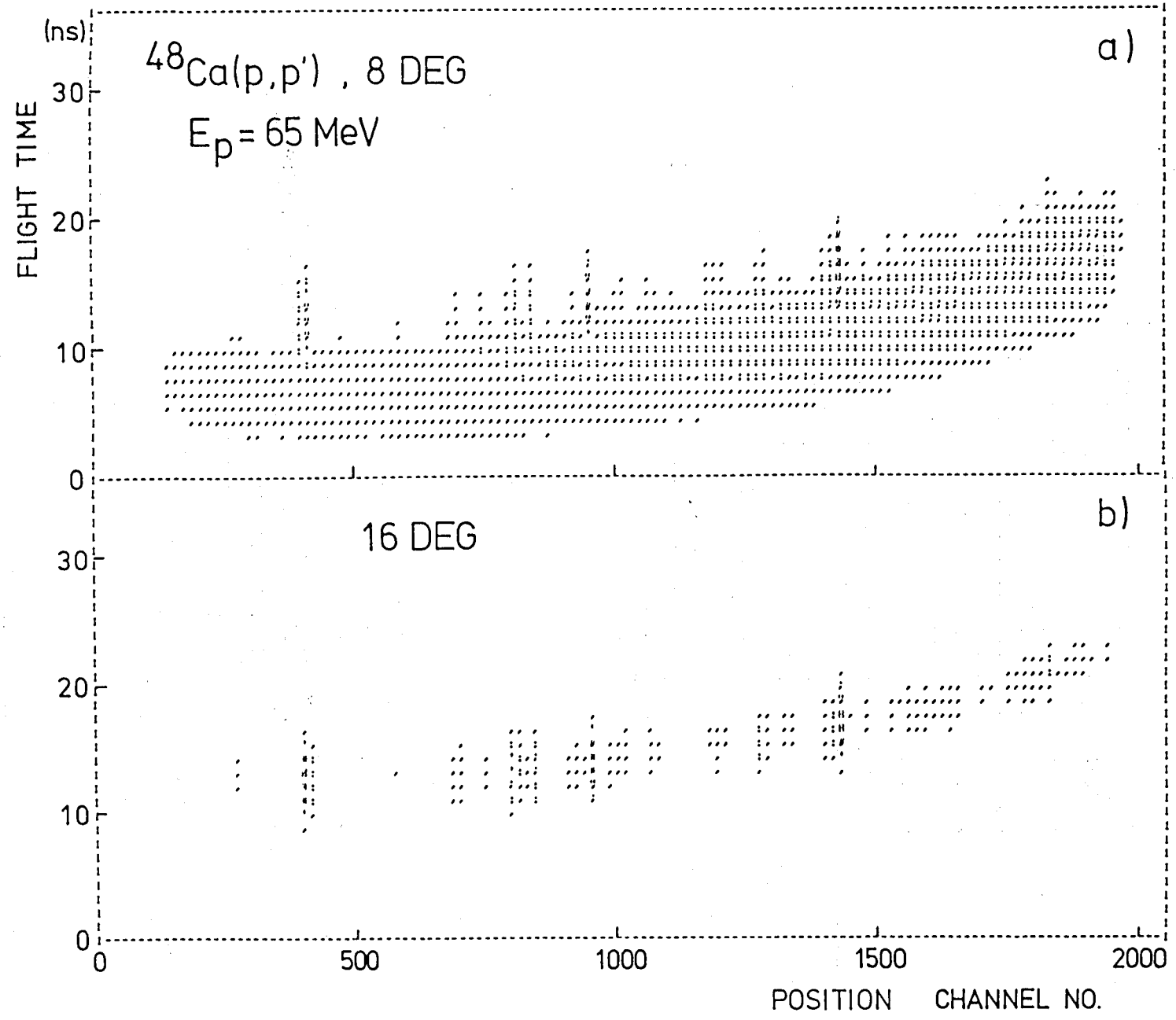
(ns)
FLIGHT TIME
^{48}Ca(p,p') , 8 DEG
E_p = 65 MeV
a)
30
20
10
0
16 DEG
b)
30
20
10
0
0
500
1000
1500
2000
POSITION CHANNEL NO.

Fig. 3-25.

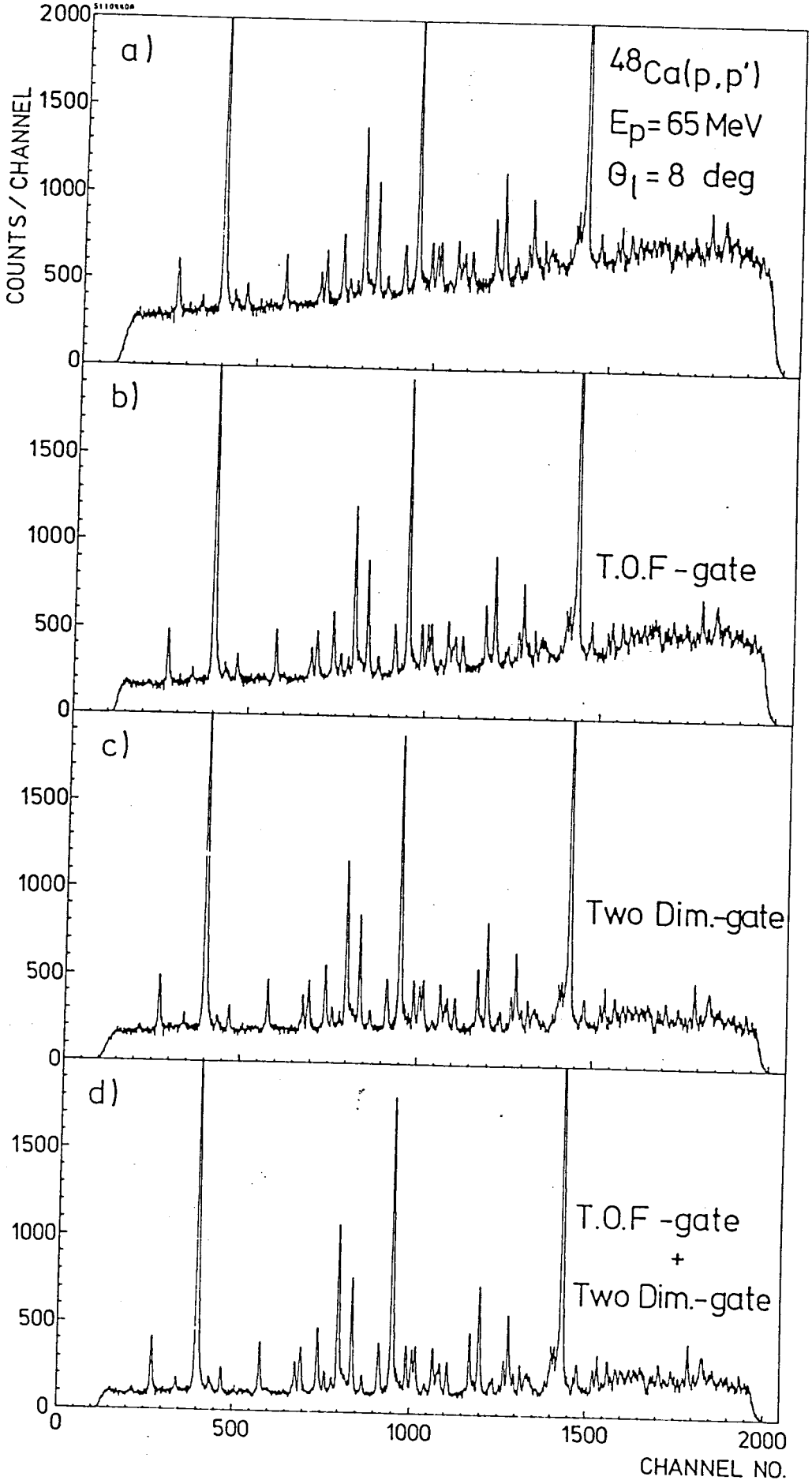
a)
^{48}Ca(p,p')
E_p= 65 MeV
θ_l = 8 deg
b)
T.O.F -gate
c)
Two Dim.-gate
d)
T.O.F -gate
+
Two Dim.-gate
COUNTS / CHANNEL
CHANNEL NO.
0
500
1000
1500
2000

Fig. 3-26.

Chapter 4

Experimental Results Using High Resolution Proton Inelastic Scattering

1. Introduction
2. Hexadecapole strength in the region of the low-energy ocupole resonance in ^{90}Zr
   - 2-1. Motivation for the experiment
   - 2-2. Experimental procedure
   - 2-3. Data reduction
     - 2-3-1. Extraction of differential cross-section
     - 2-3-2. Extraction of excitation energies
   - 2-4. Data analysis
   - 2-5. Results and discussion
3. Observation of 1^+ state in ^{48}Ca by hadron inelastic scattering
   - 3-1. Background for the experiment
   - 3-2. Experimental procedure and data reduction
   - 3-3. Results and discussion
     - 3-3-1. Assignment of spin parity for the 10.218 MeV state
     - 3-3-2. Strength of the 10.218 MeV state
   - 3-4. Summary and further development of the study

Chapter 4

Experimental Results Using High Resolution Proton Inelastic Scattering

Abstract

High resolution inelastic experiments were performed on ^{90}Zr and ^{48}Ca target using the aforementioned operating parameters of the auxiliary magnets in the spectrograph for the kinematic correction and the induction readout counter systems. For the study of ^{90}Zr, 1 m long high resolution counter was used and hexadecapole (L = 4) resonance-like states were clearly analyzed in the energy region of E_x = 4∿9 MeV. For the study of ^{48}Ca, 1.5 m long two dimensional counter was used. The ability of reducing background counts was quite powerful in obtaining reliable data for the unnatural parity 1^+ state even at the very forward scattering angles. The operating parameters for the kinematic correction worked well and high resolution spectra were obtained for the whole range of scattering angles between 6° and 70°.

1. Introduction

The magnetic spectrograph "RAIDEN" has now achieved a large solid angle and good energy resolution. Thus, a weak level of interest hitherto concealed among a large number of strong levels may be searched and identified within a reasonable experimental time. One of the reactions which can fully use above merits of the spectrograph is a proton inelastic scattering to the energy region of highly excited states. As is well known proton inelastic scattering can excite various modes of nuclear excitations. It is, thus, indispensable to perform high resolution experiments to facilitate the selection of jewel levels.

In this chapter two experimental results obtained from proton inelastic scattering is presented. One is the result on ^{90}Zr target. In this study, the level structure of ^{90}Zr was studied in the region of the so called low-energy octupole (L = 3) resonance (E_x = 5-9 MeV) by inelastic scattering of 65 MeV protons. The spectra were found to be highly structured and a previously reported resonance-like bump was resolved into many states with different multi-polarities. Among the levels, a large number of L = 4 states were found exhausting 5.8% of the E4 energy weighted sum rule. In addition to this, detailed structure of the low-energy octupole resonance was clearly revealed.

The other result presented in Section 3 was obtained for ^{48}Ca. Investigating the location and the strength of the unnatural parity 1^+ state has been an important problem

in nuclear physics. However, high level density at excitation energy of around E_x = 10 MeV has prevented to investigate these states clearly. In the present experiment the 10.2 MeV state in ^{48}Ca was confirmed to be $J^\pi = 1^+$ by (p,p'), E = 65 MeV, assisted by (α,α'), E_α= 70 MeV reaction. The state was rather strongly excited by the (p,p') reaction especially at the forward angles. The measured angular distribution of the differential cross sections of the state is compared with a microscopic distorted-wave Born approximation calculation based on a pure shell model.

By the identification of the 1^+ state in ^{48}Ca, the shape standard for the angular distribution of the differential cross section was confirmed experimentally at this mass region. Proton inelastic scattering experiments using the same incident energy of E_p = 65 MeV were performed for the N=28 nuclei ^{50}Ti, ^{52}Cr and ^{54}Fe. Many states with similar angular distribution were found in these nuclei.

2. Hexadecapole strength in the region of the Low-Energy Octupole Resonance in ^{90}Zr

2-1. Motivation for the experiment

The existence of electric giant resonances has been experimentally established[4-1] for the isoscalar monopole, isovector dipole, isoscalar quadrupole, and isoscalar low-energy octupole modes. Recently high-energy component of the octupole mode was also found in some of the nuclei[4-2]. As for the isoscalar hexadecapole mode, however, little is known so far about the location and the shape of the resonance.

In the shell model picture giant resonances are described as strongly coherent particle-hole excitations resulting from applying the multipole operator:

$$Q_{LM} = \sum_{i=1}^{n} r_i^L Y_{LM}(\theta_i, \phi_i) \qquad (4\text{-}1)$$

to the ground state of the nucleus[4-3]. Since the operator $r^L Y_{LM}$ can promote a particle at most L shells, the isoscalar hexadecapole resonance (L = 4) is predicted to split into three components at excitation energies of $E_x \sim 0\hbar\omega$, $2\hbar\omega$, and $4\hbar\omega$. The transitions with $0\hbar\omega$ correspond to the low-lying intershell transitions and a negligible amount of strength was predicted from a pure shell model calculation[4-4]. More sophisticated calculations, using random phase approximation (RPA) with large configuration spaces[4-5~7], however, predict that the isoscalar hexadecapole strength in ^{90}Zr is

fragmented over a wide range of energy, and that the low-energy tail of the distribution streaches down to $E_x \approx 5$ MeV.

In the 5-10 MeV region in ^{90}Zr a low-energy octupole resonance (LEOR) with energy center at 7.2 MeV has been observed as a resonance-like bump in α-particle inelastic scattering[4-8] at E_α = 96 MeV. A recent (p,p') experiment[4-9] using polarized proton, however, has suggested that both the differential cross section and the analyzing power for LEOR differ from those for the well established 3^- state and that a unique L = 3 assignment for the "LEOR" was not so clear cut as those derived from the work of Moss et al.[4-8]. But they could not provide more precise information because of the lack of resolution (∿100 keV).

Considering these theoretical and experimental circumstances, it is attractive to investigate whether or not the expected hexadecapole states can be found in the LEOR region of ^{90}Zr by high-resolution proton inelastic scattering. And if they were found, how much would be the strength. Such a study also has the advantage of giving a detailed picture of the strength distribution of the low energy octupole resonance.

2-2. Experimental procedure

The present measurement was performed using a 65 MeV proton beam from the Research Center for Nuclear Physics, variable energy AVF cyclotron at Osaka University. After

passing through a tandem monochromator system, it was focussed on the target and subsequently stopped in a Faraday-cup mounted in the scattering chamber. Beam intensities used ranged from 30 to 100 nA. The ^{90}Zr target was a 492 $\mu g/cm^2$ thick self-supporting metalic foil of 98% isotopic enrichment. The inelastically scattered protons were momentum analyzed with the spectrograph "RAIDEN"[4-10] and detected with the 1 m long IWPC focal plane counter described in detail in Chapter 3. The ΔE counters and a plastic E counter used for the particle identification and the data handling system were also similar to those described in Section 3-1 of Chapter 3.

Spectra were taken at angles from θ_{lab} = 10° to 63° for the range of E_x = 4.0-9.5 MeV with a solid angle of 3.2 msr. The excitation energy range covered was about 3.5 MeV for a setting of the magnetic field strength. Two runs with different excitation of the magnet were combined to cover the full spectrum. The angular distributions for elastic protons and for inelastic protons from the $J^\pi = 3^-$ state at 2.75 MeV were also measured with the same target to calibrate the target thickness and the solid angle of the spectrograph. For the compensation of the kinematic broadening effect, the excitation strengths of the sextupole and the multipole magnet of the spectrograph were adjusted depending on the scattering angle and excitation energy using the parameters determined in Chapter 2. The overall resultion of around 15 keV was obtained for the measurement.

2-3. Data reduction

2-3-1. Extraction of differential cross-section

The upper half of Fig. 4-1 shows the spectrum taken at θ_{lab} = 20°. With the resolution of 15 keV, a previously reported resonance-like bump was resolved into more than one hundred discrete levels. The observed spectra were analyzed between E_x = 4.0 and 8.6 MeV using a peak deconvolution program[4-11]. In this analysis, well separated low-lying levels were used as peak shape standard for unfolding the crowded levels. An example of the fit is shown in Fig. 4-2 for the case of E_x = 7.8∿8.1 MeV, θ_{lab} = 20°. The program was useful for obtaining the accurate integrated counts and peak positions particularly for resolving partially overlapping peaks.

The peaks due to the carbon and oxygen contaminants were subtracted by using the results of the separate measurement with a thin mylar target. The background underlying the peaks was assumed to have a shape as shown in Fig. 4-1 by tracing the lowest valley of the spectrum. Since the nature of the background is not well understood, the uncertainty in subtracting the background may cause ambiguities of about 10% in the cross sections for the relatively weak peaks. However, these ambiguities were found not to affect the L-value determination.

2-3-2. Extraction of excitation energies

Careful attention was paid to the determination of excitation energies with good accuracy. First of all the

relationship between the mean radius of the magnetic spectrometer and the channel number of the focal plane counter was derived using six well established low-lying states of ^{90}Zr. The strength of the main magnet of the spectrograph was adjusted for these peaks of interest to appear on various points of the focal line. Using the obtained peak positions, strength of the magnetic fields, and the results of kinematic calculations, radii were determined at many points of the focal line as a function of channel number and smooth curve was interpolated. The incident energy of the proton was determined from the strength of the analyzing magnet in the beam line. The highest-lying ^{90}Zr state used in this calibration was the 3.843 MeV level. Thus the energies above 3.9 MeV are obtained by extrapolation. Using the relation curve determined above, and knowing the peak positions and the field strength at the time of the measurement, the excitation energies of unknown levels were determined by consulting the kinematic calculations. Slight change of the field distribution[4-12] according to the change of the magnetic field strength was also corrected. The uncertainty in excitation energy is estimated to be 5 keV which includes the ambiguities due to a variety of sources such as uncertainties in the centroid determination, target energy loss and beam energy.

2-4. Data analysis

In order to determine the L-value and to obtain a fraction of energy weighted sum rule (EWSR) limit for each of

the deconvoluted levels, distorted wave Born approximation (DWBA) calculation was performed using a computer code DWUCK[4-13] and a collective-model form factor. The optical potential parameters used was determined by Sakaguchi et al.[4-14], which were determined to fit the angular distributions of differential cross section and analyzing power for the elastic scattering of 65 MeV protons. The calculation was found to reproduce the inelastic scattering data equally well for L = 2, 3, 4 and 5 as shown in Fig. 4-3. In the energy region analyzed in the present work, angular distributions of as many as 25 levels were found to be in good agreement with the L = 4 DWBA calculation and 34 levels with L = 3. There were only five L = 2 states and about twenty levels had $L \geq 5$. In Fig. 4-1, those levels which is identified to have L = 2, 3, 4, 5 and 6 are coloured with brown, green, red, yellow and blue, respectively. Among the strong colour-less levels, some are identified to have unnatural parity[4-15] and three levels are known to have $J^{\pi} = 1^{-}$. For the remaining weak levels we could not determine definite L-values.

All of the strong states with L = 4 character were also observed in a recent $^{90}Zr(\alpha,\alpha')$ experiment[4-16]. This leads to the rather natural assumption that the L = 4 states of the present work have $J^{\pi} = 4^{+}$. Therefore we proceed the analysis according to the assumption that all the L = 3 states have $J^{\pi} = 3^{-}$ and all the L = 4 states have $J^{\pi} = 4^{+}$.

The application of the collective-model DWBA analysis to giant resonances has been described in detail by

Satchler[4-17]. An isoscalar excitation of multipolarity L ($L \geq 2$) located at an excitation energy E, which completely exhausts the EWSR, has a deformation length

$$(\beta_L R)^2 = L(2L+1)(\hbar^2/2mE)(4\pi/3A). \quad (4-2)$$

Using the DWBA calculation described above, the deformation parameter β_L for the individual level was derived by the relation

$$\beta_L^2 = \sigma_{exp}/\sigma_{DWBA}. \quad (4-3)$$

The equilibrium radius R was assumed to be $R = R_0 A^{1/3}$, where R_0 was taken to have 1.229 according to the parameter[4-14] of DWBA calculation. The obtained deformation lengths and the EWSR percentages for the 3^- and 4^+ states in the energy region between 4.0 and 8.6 MeV are shown in Table 4-1 and the distribution of the EWSR percentages are shown in Fig. 4-4.

2-5. Results and discussion

The EWSR fraction found in this energy region is 5.8% for the 4^+ states and 10.8% for the 3^- states. The distribution of the 3^- state is on the whole in good agreement with the reported shape of LEOR[4-8,9,16,18]. However, the above EWSR fraction only amounts to about one half of the previous values of around 20%, while for the 2.75 MeV, $J^\pi = 3^-$ level, a EWSR fraction of 8.5% (βR = 0.79 fm) is obtained which agrees with previous values of around 7%. A lowering of the background level, and taking into account the remain-

ing strength in the energy region above 8.6 MeV may add another (3-4)% to the present value but a discrepancy of about 6% of the EWSR still remains. Considering the overlapping distributions of the 3^- and 4^+ states (see Fig. 4-4), the 4^+ strength might have been integrated into the octupole fraction in the previous experiments. Indeed, when the strengths of the 4^+ states were added to those of the 3^- states, the octupole EWSR fraction becomes about 20%, which is in agreement with previous values[4-8,9,16,18].

The 4^+ states observed in the present work are interesting in view of the possibility of excitation of the hexadecapole resonance. As was mentioned, according to a simple harmonic oscillator shell model, hexadecapole resonances are predicted to exist at excitations of $0\hbar\omega$, $2\hbar\omega$ and $4\hbar\omega$[4-4]. From the location and the concentration of the strengths, the observed 4^+ states could form the $0\hbar\omega$ hexadecapole resonance. In the $0\hbar\omega$ excitation, one-particle one-hole transitions of $\nu(g_{9/2} \rightarrow d_{5/2})$, $\nu(g_{9/2} \rightarrow s_{1/2})$, $\nu(g_{9/2} \rightarrow g_{7/2})$, and $(g_{9/2} \rightarrow d_{3/2})$ are expected to form 4^+ states in ^{90}Zr, and the sum of these transition strengths was estimated[4-19] to amount to 0.5% of the EWSR. The experimental value, however, accounts for 5.8% of the EWSR, which leads to an enhancement of about 10 for the hexadecapole transition. This fact strongly suggests that there exists a considerable contribution of the strength from the $2\hbar\omega$ and $4\hbar\omega$ "E4 giant resonance" which is expected to exhaust most of the EWSR fraction[4-4,6]. The RPA calcula-

tion by Kishimoto[4-19], which considers the coupling of the $0\hbar\omega$ transition with the $2\hbar\omega$ and $4\hbar\omega$ transitions, supports the possibility of this interpretaion.

In conclusion, we found many 4^+ states in LEOR region in ^{90}Zr showing a resonance-like distribution. The sum of transition strength of these 4^+ states is enhanced by a factor of 10 which might be interpreted by the contribution of high-lying "giant hexadecapole resonances". The observation of fine structure of "LEOR" enabled us to reliably extract the L = 3 strength.

3. Observation of 1^+ state in ^{48}Ca by hadron inelastic scattering

3-1. Background for the experiment

The strength distribution of the spin flip excitation in nucleus, especially the simplest one, i.e. 1^+ strength has been searched for a long time[4-20,21]. Since proton has the spin value of 1/2, excitation of 1^+ state by proton inelastic scattering is expected to be simple and is indispensable in order to obtain better understanding of the spin excitation in nuclei and of the effective spin-spin interaction[4-22,23]. Furthermore, it provides indirect information on the admixture of Δ isobar-nucleon hole excitations in the low-lying excitation spectrum. The excitation of Δ isobar is expected to cause the so called quenching of the M1 transition strength[4-24∿30] and well observed for the case of Gamow-Teller transition[4-31∿33].

According to the shell model, the M1 strength should be concentrated in a single particle-hole state for a closed shell nucleus with spin-unsaturated j-shell closures. Thus ^{48}Ca, ^{90}Zr and ^{208}Pb seem to be the best candidates for studying the spin excitation, and concentration of the M1 strength might be expected in these nuclei. However, the M1 strength in these nuclei has been a long standing problem. In the case of ^{208}Pb, two 1^+ states are expected resulting from the one-particle, one-hole configurations $\nu(i_{13/2}^{-1}, i_{11/2})$ and $\pi(h_{11/2}^{-1}, h_{9/2})$. Recently a 1^+ state with $\pi(h_{11/2}^{-1}, h_{9/2})$ configuration have been established at 5.85

MeV by the nuclear resonance fluorescence experiment[4-34] and also by $^{209}Bi(d,^3He)\ ^{208}Pb$ and $^{208}Pb(p,p')^{208}Pb$ experiments[4-35] but little is known about the states with $\nu(i_{13/2}^{-1}, i_{11/2})$ nature. There were two reports about the M1 states in ^{90}Zr which is expected to have a configuration of $\nu(g_{9/2}^{-1}, g_{7/2})$. One is by Meuer et al.[4-36], who used high resolution inelastic electron scattering. They identified three 1^+ states at 8.233, 9.000 and 9.371 MeV of excitation and suggested seven additional states as probable 1^+ states. The upper limit of the total strength deduced was $1.8\pm0.4\mu_k^2$, which was at most one-third of the prediction of the $\nu(g_{9/2}^{-1}, g_{7/2})$ spin-flip transition[4-36]. The other report is by Anantaraman et al.[4-37], who observed a giant M1 transition in ^{90}Zr by the (p,p') reaction at 200 MeV with the energy resolution of 80 keV. The resonance was located at 8.90±0.15 MeV of excitation with the width of 1.7±0.2 MeV [full width at half maximum (FWHM)] and at least half of the strength predicted by the pure shell model was observed. The differences in shape and yield of the 1^+ states between the two experiments seem to raise questions about the nature of the M1 states in ^{90}Zr.

In order to make the confused situation clearer, we decided to perform proton inelastic scattering experiment on ^{48}Ca which is thought to be more ideal magic nucleus. The $^{48}Ca(d,^3He)^{47}Ca$, proton pick-up reaction[4-38] observed no observable $f_{7/2}$ and $p_{3/2}$ strength. The ground state of ^{48}Ca, therefore, has a fairly well closed proton shell. It is

also known from neutron pick-up reactions[4-39,40] that the spectroscopic factors are around seven, which means that the average number of $f_{7/2}$ neutrons is very close to the independent particle shell model expectation, i.e. 8. Ground-state correlations are therefore fairly small. Consequently, the excited 1^+ state has a dominant $(f_{7/2}^{-1}, f_{5/2})$ neutron particle-hole structure. This is also corroborated by RPA[4-41] and recent shell model calculations in the complete fp model space[4-42].

A strong M1 state was recently identified at 10.227 MeV by steffen et al.[4-43] using the (e,e') reaction. They reported no significant fragmentation of the M1 strength in ^{48}Ca. Another indirect evidence for the strong M1 resonance in ^{48}Ca was obtained from the $^{48}Ca(p,n)^{48}Sc$ reaction by Anderson et al.[4-44]. They found a narrow peak at 16.8 MeV in ^{48}Sc and interpreted it as the analog of the 1^+ state in ^{48}Ca. The ground state analog of ^{48}Ca is at 6.67 MeV, thus their suggestion is consistent with the $^{48}Ca(e,e')$ result from the energy systematics consideration.

In view of these circumstances, the observation of the 1^+ state in ^{48}Ca by the (p,p') reaction is particularly important because this mode of excitation provides direct information about the distribution of spin excitation in nuclei. Futhermore, it is of our great interest to see consistency or difference, if any, between the results from the $^{48}Ca(p,p')$ and the $^{48}Ca(e,e')$ experiment about 1^+ state.

3-2. Experimental procedure and data reduction

The $^{48}Ca(p,p')$ experiment was performed using the 65 MeV proton beam from the RCNP, AVF cyclotron. The ^{48}Ca target was a 1.06 mg/cm^2 thick self-supporting foil with 97.7% isotopic enrichment[4-45]. The inelastically scattered protons were momentum analyzed with the spectrograph and detected with the 1.5 m long two-dimensional position sensitive proportional counter system described in Section 4 of Chapter 3. All the data recorded on the magnetic tape in the event mode was analyzed with a software for correcting the vertical aberration and reducing the abnormally scattered background particles. Experimental difficulties in studying 1^+ states arise from the high level density at excitation energies around E_x = 10 MeV, where these states are expected. Therefore the investigation of 1^+ states with hadrons have to be performed with good energy resolution. The overall resolution of 15 keV was obtained for the acceptance solid angle of 2.4 msr. Here the vertical acceptance angle of the spectrograph was decreased to discriminate background particles by the two dimensional position determination of the particles as described in Section 4 of Chapter 3. This way of position determination and the time-of-flight measurements employed in the experiment were powerful in obtaining reliable data by reducing background counts especially at forward angles.

Spectra of the inelastically scattered protons were taken at angles from θ_{lab} = 6° to 70°. The absolute cross

section was obtained by calibrating the target thickness and the whole detection system so as to get agreement between the measured elastic scattering cross section and the calculated one[4-14]. Here we used the calculation which reproduced the carefully measured cross section at the same incident energy[4-14]. The upper half of Fig. 4-5 shows the spectrum at $\theta_{lab} = 8°$. A prominent peak was observed at 10.218±0.007 MeV. The width of the peak was not wider than the experimental resolution of 15 keV. The excitation energy of this peak corresponded well to the 10.227 MeV, 1^+ state observed in the (e,e') experiment[4-43]. In Fig. 4-6, the measured angular distribution for this state is presented together with that of the first 2^+ state at 3.832 MeV. The peak deconvolution program[4-11] was used to obtain reliable cross sections. In this analysis, well separated low-lying levels were used as peak shape standards for unfolding the crowded levels. The program was useful for obtaining the accurate integrated counts and peak positions particularly for resolving partially overlapping peaks. The absolute errors of the cross sections were estimated to be about 10%. The experimental angular distribution of the 2^+ state shows an oscillating pattern and that of the 10.218 MeV state shows a rather monotonous pattern.

For the purpose of the parity assignment for the 10.218 MeV state, the $^{48}Ca(\alpha,\alpha')$ experiment was performed at E_α = 70 MeV with the same target. The spectra were taken at two angles of θ_{lab} = 13° and 16°. The angles chosen corresponded

to the expected local minimum and second maximum of the angular distribution for the 2^+ state. Measurements at the two angles were also important for discriminating against contaminant peaks. The spectrum obtained at 16° is shown in the lower half of Fig. 4-5, where the height of the 3.832 MeV, 2^+ peak is normalized to that of the (p,p') peak. Though the resolution was rather poor ($\sim$30 keV) in the (α,α') experiment, good overall correspondence of the peaks was observed in the two experiments.

3-3. Results and Discussion

3-3-1. Assignment of spin parity for the 10.218 MeV state

In order to make the spin and parity assignment for the 10.218 MeV state, we first examined the result of the (p,p') reaction. Forward peaking of the angular distribution for this state as shown in Fig. 4-6 rules out the possibility of the 10.218 MeV state being $J \geq 3$, and the possibilities of $J^\pi = 2^+$, 2^- and 1^- still remain. The comparison between the result of (p,p') and (α,α') experiments strongly suggests that the state is an unnatural parity state. As is seen in Fig. 4-5, the 2^+ state at 3.832 MeV was clearly seen in both the spectra. On the other hand, no strong peak was seen in the (α,α') experiment around 10.2 MeV of excitation. As shown in Fig. 4-6, a possibility of this state being 2^- can also be ruled out by comparing the present angular distribution with that of a 2^- state obtained in the ^{40}Ca(p,p')^{40}Ca reaction at the same incident proton energy[4-46]. With the

same reason $J^{\pi} = 1^{-}$ is rejected for the state. Thus we conclude that spin and parity of the 10.218 MeV state are $J^{\pi} = 1^{+}$. No other evident peak with the intensity larger than one tenth of the 10.218 MeV state and showing the similar angular distribution to that of 10.218 MeV state was observed in the energy region around 10.2 MeV. However a small peak with an intensity of one ninth of that of 10.218 MeV peak was observed at 9.0 MeV. It is interesting to note that we obtained a good agreement between the (p,p') and (e,e') experiments in contrast to the case of ^{90}Zr. The observation of two 1^{+} states is consistent with a recent shell model calculation[4-42] though they expected only 0.2 MeV energy difference for the two 1^{+} states.

3-3-2. Strength of the 10.218 MeV state

Microscopic DWBA calculation was performed for the 1^{+} state at 10.218 MeV. In this analysis we assumed the ground state of ^{48}Ca to be a pure $\nu(f_{7/2})^{8}$ configuration and the 1^{+} state to be a pure $\nu(f_{7/2}^{-1}, f_{5/2})$ configuration. A computer code DWBA74[4-47] which treats knock-on exchange processes exactly was used. Single particle wave functions were calculated in a Woods-Saxon well of radius $R = 1.25\ A^{1/3}$ fm, diffuseness a = 0.6 fm, and a spin-orbit force of 6 MeV. The $1f_{7/2}$ and $1f_{5/2}$ neutrons were assumed to be bound by 9.9 MeV and 1.5 MeV, respectively. The optical-model parameters used were taken from Ref. 4-14, which fitted not only the elastic cross section but also the polarization data. This

set of parameters reproduce well the experimental angular distribution of the 2^+ state at 3.832 MeV in the collective DWBA analysis[4-48] as shown in Fig. 4-6. The effective-two-body interaction used is the M3Y[4-23] which is based on G matrics constructed from realistic interaction potentials.

As shown in Fig. 4-6, the calculation for the 1^+ state reproduces the decreasing pattern of the angular distribution of the 10.218 MeV state quite well. But it overestimates the cross section by a factor of 4. This factor may imply that the 10.2 MeV state exhausts about 25% of the total M1 strength. This is consistent with the result of the $^{48}Ca(p,n)^{48}Sc$ experiment at 160 MeV[4-44], where the GT transition rate has to be reduced by roughly a factor 4 in order to make a RPA calculation[4-41] comparable with the data. When a similar assumption of $f_{7/2} \rightarrow f_{5/2}$ transition was used in the $^{48}Ca(e,e')$ analysis[4-43], they found that the 1^+ state at 10.2 MeV carried roughly one-third of the total M1 strength. Therefore, as for the 1^+ state in ^{48}Ca, the results of three reactions are consistent to each other.

In a recent $^{40}Ca(p,p')^{40}Ca$ experiment[4-46], the 1^+ peak seen in the electron inelastic scattering[4-49] was missing. The distorted wave calculation with a wave function as reproduces the B(M1) value in the electron inelastic scattering overestimated the transition strength of proton inelastic scattering about a factor of twenty[4-46]. This is in contrast with the good agreement obtained for ^{48}Ca between the present experiment and the (e,e') result.

3-4. Summary and further development of the study

Quenching of the M1 strength in medium and heavy nuclei is still a big unsettled problem. A recent theoretical study of the 1^+ state in ^{48}Ca by Härting et al.[4-50] emphasized the role of virtual Δ-hole excitations. They expects that the transition is quenched by about a factor of two with this effect and that the reduced M1 strength at low energy finds its counterpart in the concentration of strong M1 transitions in the Δ resonance region at excitation energies around 300 MeV. However the effects of core polarization on M1 quenching seems not to be ignored as was pointed out by McGrory and Wildenthal[4-42]. The shell model calculations in the complete fp model space predicted that the state $\nu(f_{7/2}^8, J=0)$ to comprise 90% of the ground-state wave function. However the quenching factor of at least 3/4 was expected by a very small degree of configuration mixing in the $J^\pi = 0^+$ ground state.

Considering the situation, the acquisition of good experimental strength distributions of 1^+ states is imperative in order to understand the M1 quenching in medium weight nuclei. Proton inelastic scattering experiments were performed for the N=28 isotones of ^{50}Ti, ^{52}Cr and ^{54}Fe. Since the shape standard for the angular distribution of the differential cross section was confirmed by the 1^+ state in ^{48}Ca, the 1^+ states in these isotones were identified by the similarity of the angular distributions. Some of the examples of the angular distribution are shown in Fig. 4-7, where dotted

lines show the pattern of the 1^+ state in ^{48}Ca. The preliminary result of the strength distribution is shown in Fig. 4-8 and the further analysis is still in progress.

In summary, we confirmed a strong 1^+ state at 10.218 MeV in ^{48}Ca by using (p,p') and (α,α') experiments. The shape of the angular distribution obtained in the (p,p') reaction was well described by the microscopic calculation using the M3Y interaction. But the experimental yield was found to be a quarter of the calculated yield. The result was consistent with the quenching factors obtained in the recent (e,e') (ref. 4-43) and (p,n) (ref. 4-44) experiments. By the identification of the 1^+ state in ^{48}Ca, the shape standard for the angular distribution of the differential cross section was confirmed around this mass region.

References

4-1 Giant Multipole Resonances, edited by F.E. Bertrand (Harwood, New York, 1980).

4-2 T.A. Carey, W.D. Cornelius, N.J. DiGiacomo, J.M. Moss, G.S. Adams, J.B. McClelland, G. Pauletta, C. Whitten, M. Gazzaly, N. Hintz and C. Glashausser, Phys. Rev. Lett. 45 (1980) 239;
T. Yamagata, S. Kishimoto, K. Yuasa, K. Iwamoto, B. Saeki, M. Tanaka, T. Fukuda, I. Miura, M. Inoue and H. Ogata, Phys. Rev. C23 (1981) 937.

4-3 A. Bohr and B.R. Mottelson, Nuclear Structure (Benjamin, Reading, Mass., 1975), Vol. 2.

4-4 I. Hamamoto, Nucl. Phys. A196 (1972) 101.

4-5 G.F. Bertsch and S.F. Tsai, Phys. Rep. 18 (1975) 125.

4-6 K.F. Liu and G.E. Brown, Nucl. Phys. A265 (1976) 385.

4-7 J. Speth, J.S. Dehesa, A. Faessler, V.A. Madsen, G.A. Rinker and J. Wambach, J. Phys. Soc. Japan 44 (1978) 213; and refs. therein.

4-8 J.M. Moss, D.H. Youngblood, C.M. Rozsa, D.R. Brown and J.D. Bronson, Phys. Rev. Lett. 37 (1976) 816; J.M. Moss, D.R. Brown, D.H. Youngblood, C.M. Rozsa and J.D. Bronson, Phys. Rev. C18 (1978) 741.

4-9 P. Martin, Y. Gaillard, P. de Saintignon, G. Perrin, J. Chauvin, G. Duhamel and J.M. Loiseaux, Nucl. Phys. A315 (1979) 291.

4-10 H. Ikegami, S. Morinobu, I. Katayama, M. Fujiwara and S. Yamabe, Nucl. Instr. and Meth. 175 (1980) 335.

4-11 Peak deconvolution program by S. Morinobu, unpublished.

4-12 I. Katayama, S. Morinobu, Y. Fujita, M. Fujiwara, T. Yamazaki and H. Ikegami, Nucl. Instr. and Meth. 171 (1980) 195.

4-13 P.D. Kunz, a DWBA computer program, Univ. of Colorado, unpublished.

4-14 H. Sakaguchi, M. Nakamura, K. Hatanaka, A. Goto, T. Noro, F. Ohtani, H. Sakamoto and S. Kobayashi, Phys. Lett. 89B (1979) 40;
H. Sakaguchi, M. Nakamura, K. Hatanaka, A. Goto, T. Noro, F. Ohtani, H. Sakamoto and S. Kobayashi, RCNP Annual Report, (1978), p. 12.

4-15 M. Fujiwara, Y. Fujita, S. Morinobu, I. Katayama, T. Yamazaki, T. Itahashi and H. Ikegami, Phys. Lett. 106B (1981) 51.

4-16 T. Tohei et al., INS annual report, (1977) 33; and private communication.

4-17 G.R. Satchler, Nucl. Phys. A195 (1972) 1.

4-18 N.J. DiGiacomo and R.J. Peterson, Phys. Rev. C20 (1979) 693.

4-19 T. Kishimoto, private communitation.

4-20 G.F. Bertsch, Nucl. Phys. A354 (1981) 157; and references therein.

4-21 G.E. Brown and S. Raman, Comments Nucl. Part. Phys. 9 (1980) 79.

4-22 W.G. Love and G.R. Satchler, Nucl. Phys. A159 (1970) 1.

4-23 G. Bertsch, J. Borysowicz, H. McManus and W.G. Love,

Nucl. Phys. A284 (1977) 399;
W,G, Love, in The (p,n) Reaction and the Nucleon-Nucleon Force, edited by C.D. Goodman et al. (Plenum, New York, 1980), p. 23.

4-24 M. Ericson, A. Figureau and C. Thevenet, Phys. Lett. 45B (1973) 19.

4-25 M. Rho, Nucl. Phys. A231 (1974) 493.

4-26 K. Ohta and M. Wakamatsu, Nucl. Phys. A234 (1974) 445.

4-27 E. Oset and M. Rho, Phys. Rev. Lett. 42 (1979) 42.

4-28 I.S. Towner and F.C. Khanna, Phys. Rev. Lett. 42 (1979) 51.

4-29 H. Toki and W. Weise, Phys. Lett. 97B (1980) 12.

4-30 A. Bohr and B.R. Mottelson, Phys. Lett. 100B (1981) 10.

4-31 R.R. Doering, A. Galonsky, D.M. Patterson and G.F. Bertsch, Phys. Rev. Lett. 35 (1975) 1691.

4-32 D.E. Bainum, J. Rapaport, C.D. Goodman, D.J. Horen, C.C. Foster, M.B. Greenfield and C.A. Goulding, Phys. Rev. Lett. 44 (1980) 1751.

4-33 C.D. Goodman, C.A. Goulding, M.B. Greenfield, J. Rapaport, D.E. Bainum, C.C. Foster, W.G. Love and F. Petrovich, Phys. Rev. Lett. 44 (1980) 1755.

4-34 K. Wienhard, K. Ackermann, K. Bangert, U.E.P. Berg, C. Bläsing, W. Naatz, A. Ruckelshansen, D. Rück, R.K.M. Schneider and R. Stock, Phys. Rev. Lett. 49 (1982) 18.

4-35 S.I. Hayakawa, M. Fujiwara, S. Imanishi, Y. Fujita, I. Katayama, S. Morinobu, T. Yamazaki, T. Itahashi and H. Ikegami, Phys. Rev. Lett. to be published.

4-36 D. Meuer, R. Frey, D.H.H. Hoffman, A. Richter, E. Spamer, O. Titze and W. Knüpfer, Nucl. Phys. A349 (1980) 309.

4-37 N. Anantaraman, G.M. Crawley, A. Galonsky, C. Djalali, N. Marty, M. Morlet, A. Willis and J.-C. Jourdain, Phys. Rev. Lett. 46 (1981) 1318.

4-38 P. Doll, G.J. Wagner, K.T. Knöpfle and G. Mairle, Nucl. Phys. A263 (1976) 210.

4-39 R.J. Peterson, Phys. Rev. 170 (1968) 1003.

4-40 J.L. Yntema, Phys. Rev. 186 (1969) 1144.

4-41 F. Osterfeld, T. Suzuki and J. Speth, Phys. Lett. 99B (1981) 75.

4-42 J.B. McGrory and B.H. Wildenthal, Phys. Lett. 103B (1981) 173.

4-43 W. Steffen H.-D. Graf, W. Gross, D. Meuer, A. Richter, E. Spamer, O. Titze and W. Knupfer, Phys. Lett. 95B (1981) 23.

4-44 B.D. Anderson, J.N. Knudson, P.C. Tandy, J.W. Watson, R. Madey and C.C. Foster, Phys. Rev. Lett. 45 (1980) 699.

4-45 Made by Mr. I. Sugai at INS, Univ. of Tokyo.

4-46 H. Ejiri, M. Sasao, T. Shibata, H. Ohsumi, Y. Fujita, M. Fujiwara, H. Ikegami, I. Katayama, S. Morinobu and T. Yamazaki, Phys. Rev. C24 (1981) 2001; and private communication.

4-47 J. Raynal and R. Schaeffer (unpublished).

4-48 Code DWUCK-4, P.D. Kunz (unpublished) was used in the analysis.

4-49 W. Gross, D. Meuer, A. Richter, E. Spamer, O. Titze and W. Knüpfer, Phys. Lett. 84B (1979) 296.

4-50 A. Härting, W. Weise, H. Toki and A. Richter, Phys. Lett 104B (1981) 261.

Table 4-1.

SUM RULE FRACTIONS FOR $J^{\pi}= 3^{-}$ STATES

Ex(MeV)	βR(fm)	S(%)	Ex	βR	S
5.122	0.12	0.39	7.250	0.09	0.30
5.636	0.21	1.28	7.278	0.09	0.27
5.673	0.17	0.81	7.417	0.08	0.23
5.785	0.11	0.35	7.438	0.06	0.12
5.946	0.10	0.31	7.476	0.10	0.40
6.305	0.07	0.14	7.629	0.10	0.38
6.415	0.10	0.30	7.648	0.08	0.22
6.494	0.05	0.09	7.737	0.07	0.19
6.724	0.11	0.39	7.765	0.08	0.23
6.757	0.13	0.56	7.917	0.12	0.55
6.882	0.07	0.14	8.138	0.11	0.50
6.989	0.06	0.10	8.183	0.05	0.09
7.017	0.06	0.14	8.291	0.08	0.25
7.062	0.09	0.28	8.427	0.07	0.22
7.104	0.10	0.33	8.445	0.07	0.20
7.135	0.09	0.26	8.530	0.06	0.14
7.215	0.11	0.41	8.554	0.07	0.22
			TOTAL		10.79(%)

SUM RULE FRACTIONS FOR $J^{\pi}=4^{+}$ STATES

Ex(MeV)	βR(fm)	S(%)	Ex	βR	S
4.068	0.14	0.24	6.828	0.08	0.11
4.340	0.29	1.04	6.868	0.08	0.11
4.952	0.19	0.05	6.910	0.09	0.17
5.221	0.12	0.22	7.075	0.09	0.18
5.387	0.19	0.55	7.166	0.08	0.12
5.470	0.17	0.46	7.290	0.06	0.06
5.989	0.09	0.15	7.538	0.11	0.25
6.071	0.11	0.23	7.782	0.04	0.04
6.179	0.12	0.24	7.811	0.09	0.17
6.323	0.12	0.26	7.892	0.10	0.21
6.532	0.07	0.09	7.941	0.10	0.23
6.681	0.12	0.29	7.999	0.05	0.06
6.709	0.11	0.24			
			TOTAL		5.77(%)

Figure captions

Fig. 4-1. Spectra of inelastically scattered protons on ^{90}Zr at E_p = 65 MeV. The vertical scales are normalized so that the 5.39, $J^\pi = 4^+$ state shows the same height in both figures. In the lower figure, the states with $L \leq 3$ are seen to be reduced relative to those with L = 4 due to the difference in angular distributions.

Fig. 4-2. For the analysis of the crowded levels, peak deconvolution program was used to obtain accurate integrated counts and peak positions. Well separated low-lying levels were used as peak shape standard in the process of unfolding.

Fig. 4-3. The angular distributions for some states with $J^\pi = 2^+$, 3^-, 4^+ and 5^-. The DWBA calculations shown by the solid lines are normalized to the data. The optical model parameters were taken from ref. 4-14, where $R = 1.229\ A^{1/3}$ fm was assumed.

Fig. 4-4. The distribution of the EWSR percentages for the octupole and hexadecapole strengths found in the energy region between 4.0 MeV and 8.6 MeV.

Fig. 4-5. Upper half: spectrum of inelastically scattered protons on ^{48}Ca at E_p = 65 MeV, θ_{lab} = 8°. A sharp peak can be seen at 10.2 MeV. Lower half: spectrum of inelastically scattered particles on ^{48}Ca at E_α = 70 MeV, θ_{lab} = 16°. The peak height for the 2^+ state at 3.832 MeV is normalized to that for the same state in the (p,p') spectrum.

Fig. 4-6. Upper half: experimental angular distributions of the $^{48}Ca(p,p')$ reaction leading to the 1^+ and 2^+ states. The dotted line shows the results of the microscopic DWBA calculation for the $J^\pi = 1^+$ state using the M3Y interaction. The calculated absolute cross sections are reduced by a quarter to fit the experimental data. The solid line is the result of the DWBA calculation with a collective form factor. Lower half: angular distributions of the $^{48}Ca(p,p')$ reaction leading to the 1^- and 2^- states. The solid lines are drawn only for the guide of the eye.

Fig. 4-7. Experimental angular distributions of the cross sections of the observed 1^+ states in ^{52}Cr and ^{54}Fe. Dotted lines represent the shape of the angular distribution of the 1^+ state at 10.218 MeV in ^{48}Ca.

Fig. 4-8. Relative strength of the observed 1^+ states.

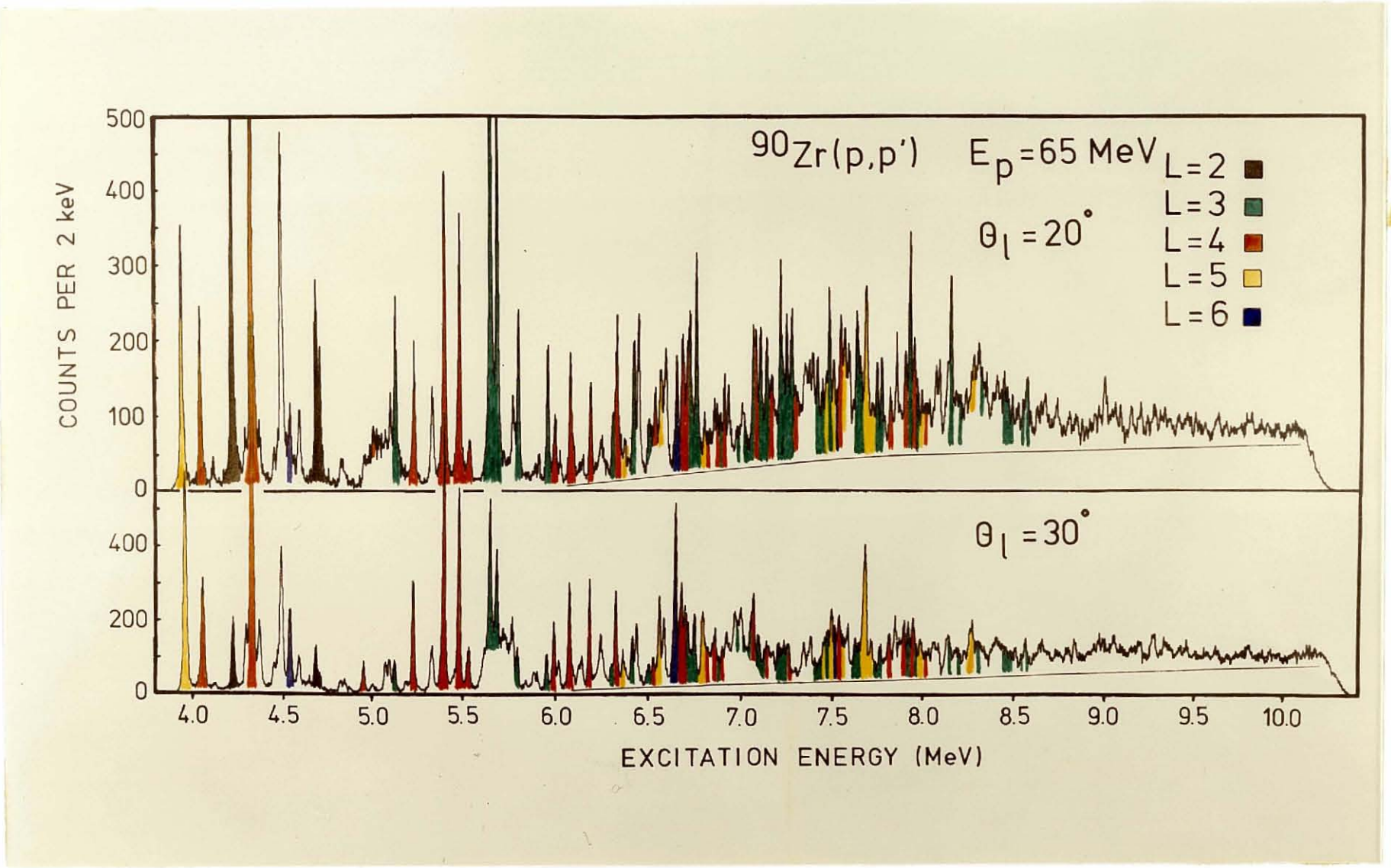
^{90}Zr(p,p') E_p=65 MeV
θ_l = 20°
θ_l = 30°
L=2
L=3
L=4
L=5
L=6
COUNTS PER 2 keV
500
400
300
200
100
0
400
200
0
4.0
4.5
5.0
5.5
6.0
6.5
7.0
7.5
8.0
8.5
9.0
9.5
10.0
EXCITATION ENERGY (MeV)

Fig. 4-1.

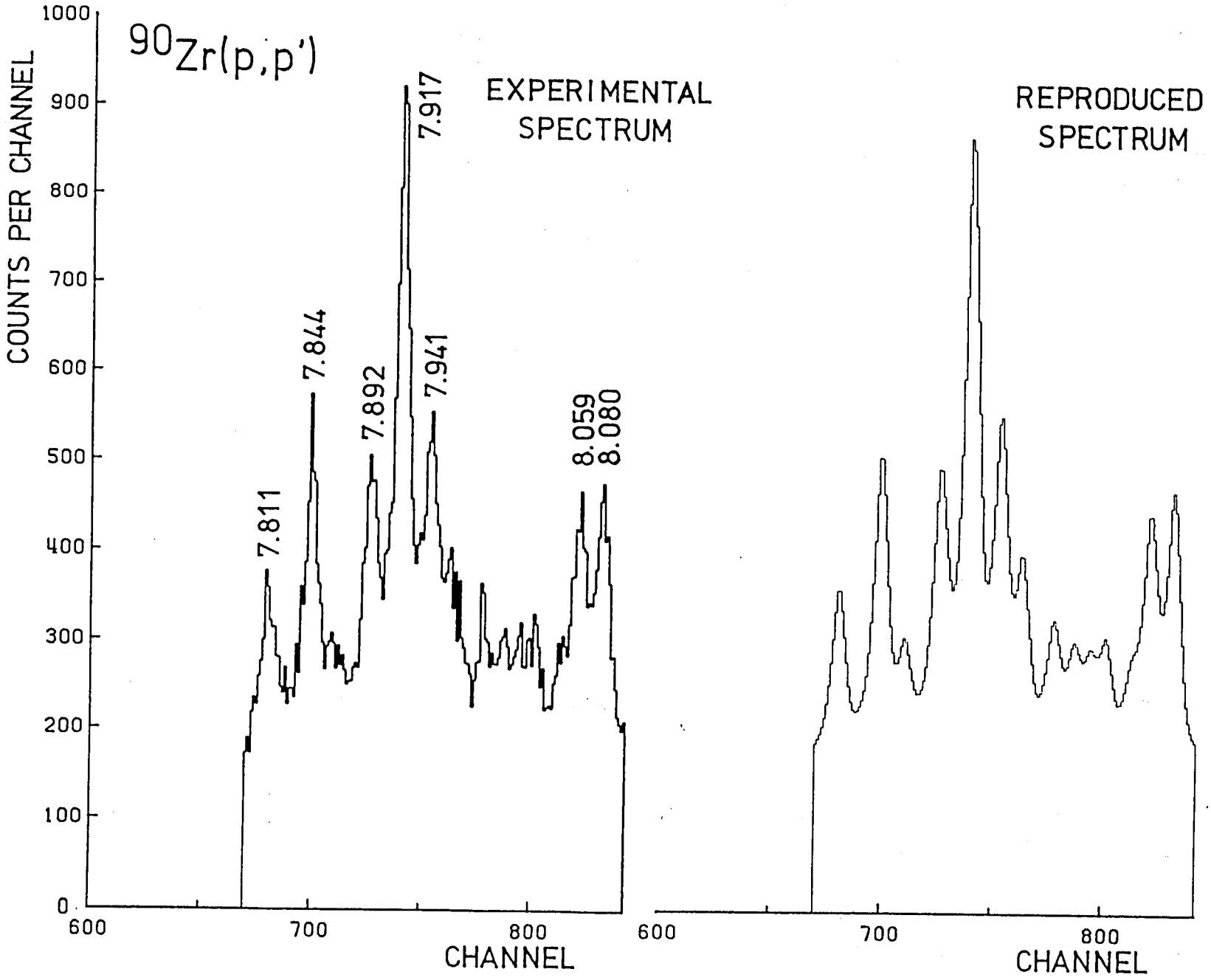
^{90}Zr(p,p')
EXPERIMENTAL SPECTRUM
REPRODUCED SPECTRUM
COUNTS PER CHANNEL
CHANNEL
CHANNEL
7.811
7.844
7.892
7.917
7.941
8.059
8.080
0
100
200
300
400
500
600
700
800
900
1000
600
700
800

Fig. 4-2.

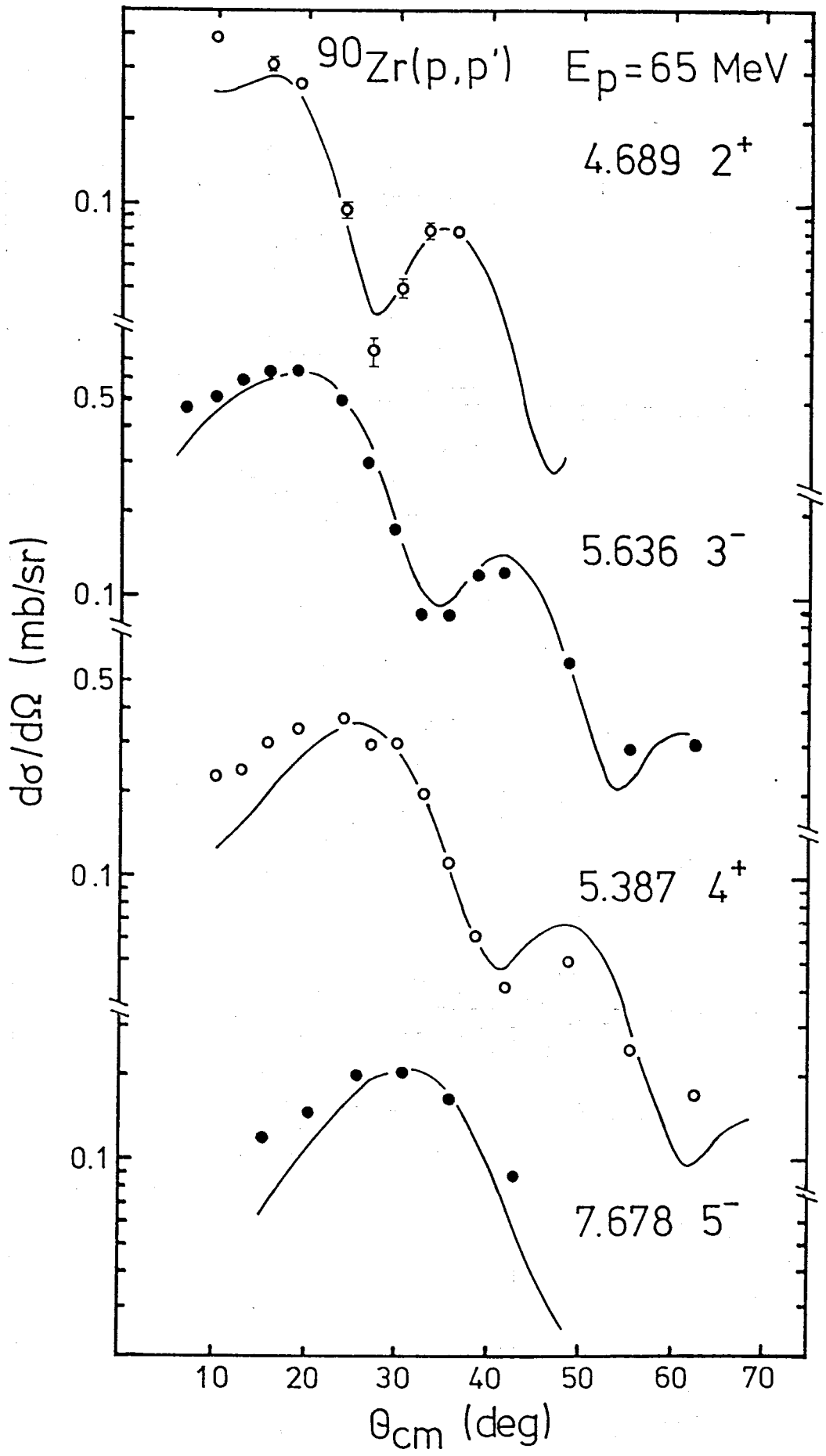
90Zr(p,p') Ep=65 MeV
4.689 2+
5.636 3-
5.387 4+
7.678 5-
dσ/dΩ (mb/sr)
θcm (deg)
0.1
0.5
10
20
30
40
50
60
70

Fig. 4-3.

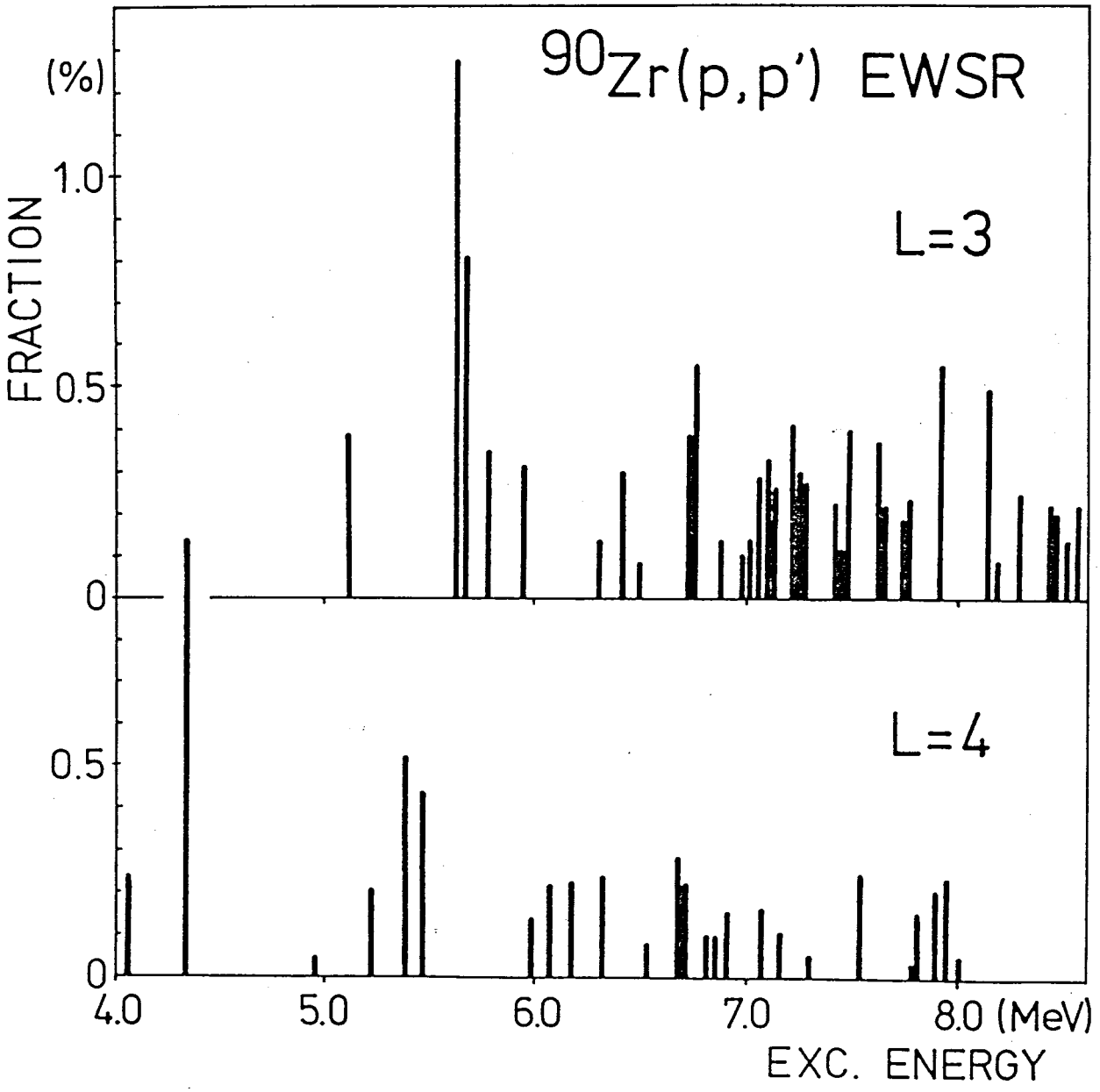
^{90}Zr(p,p') EWSR
(%)
FRACTION
1.0
0.5
0
L=3
L=4
0.5
0
4.0
5.0
6.0
7.0
8.0 (MeV)
EXC. ENERGY

Fig. 4-4.

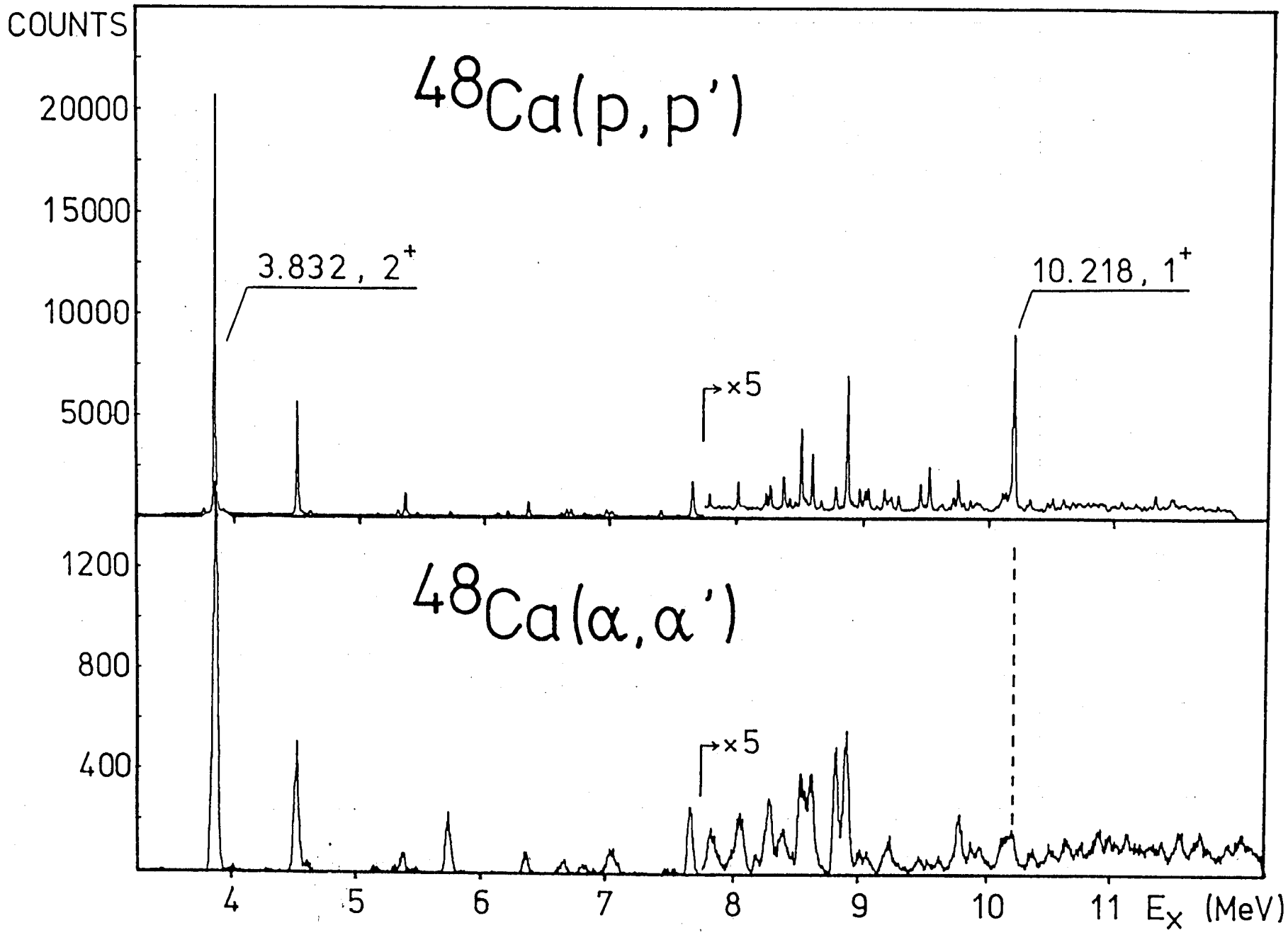
COUNTS
20000
15000
10000
5000
$^{48}Ca(p,p')$
3.832, 2^+
10.218, 1^+
×5
1200
800
400
$^{48}Ca(\alpha,\alpha')$
×5
4
5
6
7
8
9
10
11
E_x (MeV)

Fig. 4-5.

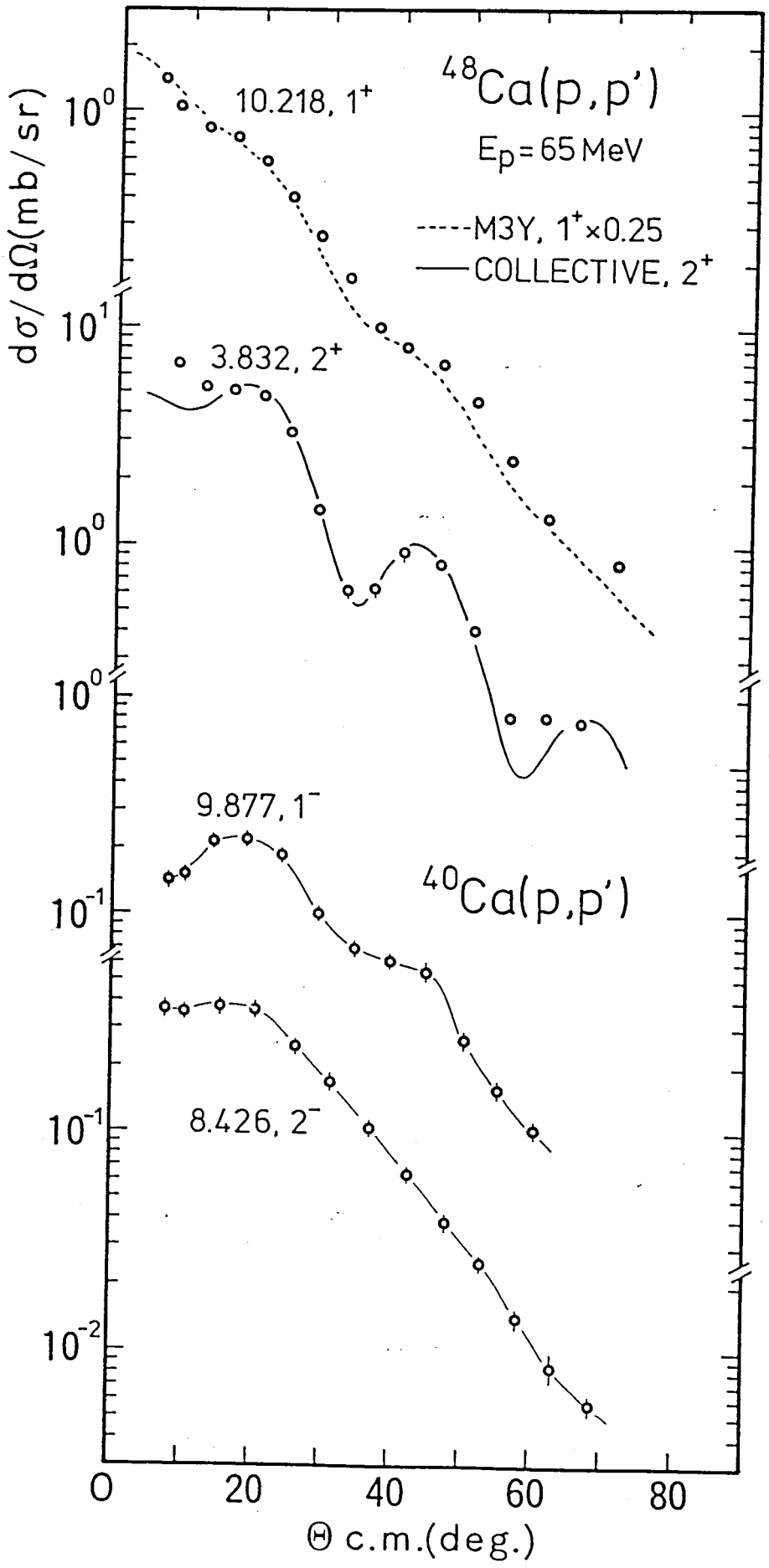
^{48}Ca(p,p')
E_p=65 MeV
10.218, 1$^+$
-----M3Y, 1$^+$×0.25
——COLLECTIVE, 2$^+$
3.832, 2$^+$
9.877, 1$^-$
^{40}Ca(p,p')
8.426, 2$^-$
dσ/dΩ(mb/sr)
Θ c.m.(deg.)

Fig. 4-6.

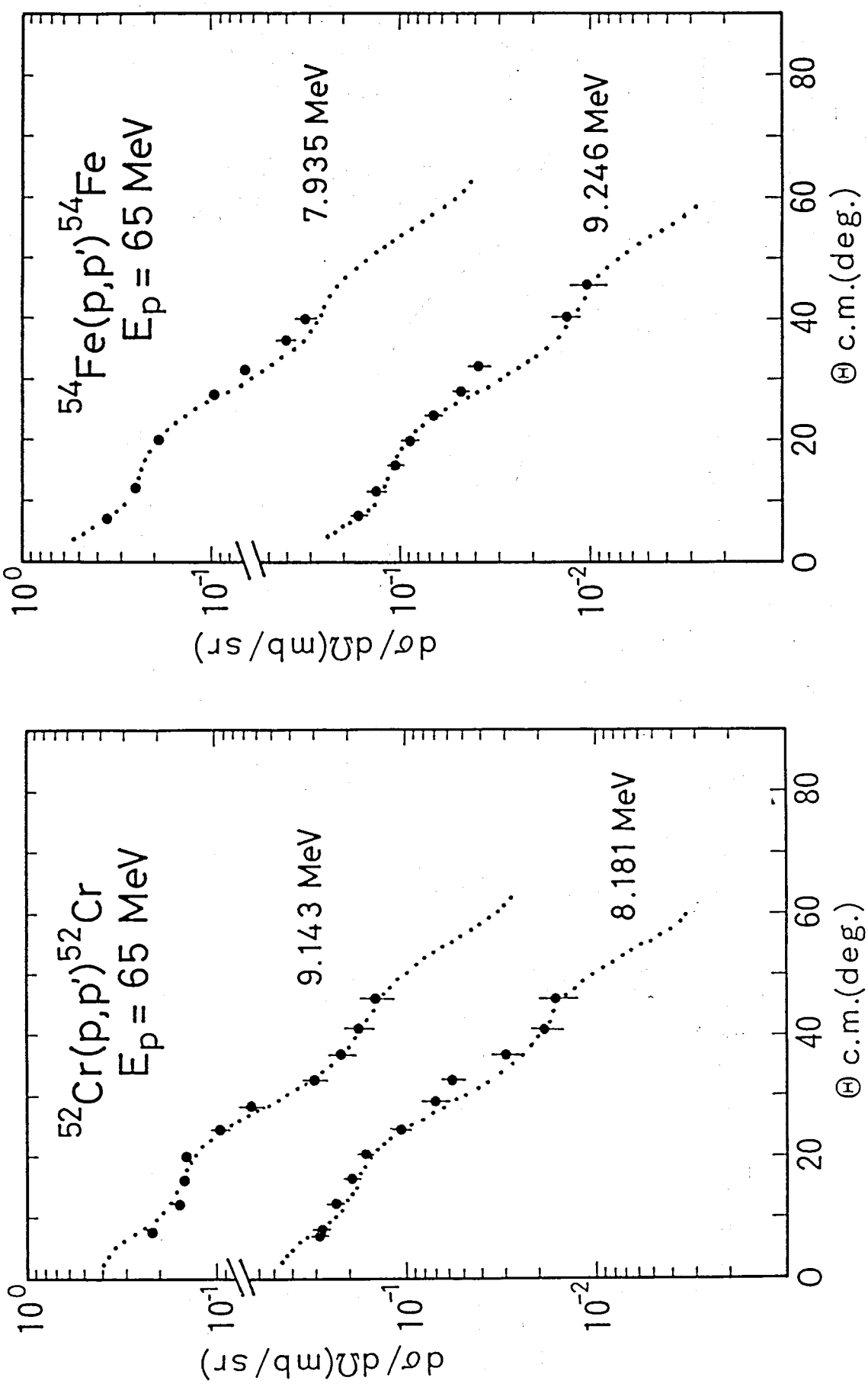
^{54}Fe(p,p')^{54}Fe
E_p = 65 MeV
7.935 MeV
9.246 MeV
^{52}Cr(p,p')^{52}Cr
E_p = 65 MeV
9.143 MeV
8.181 MeV
dσ/dΩ(mb/sr)
Θ c.m.(deg.)

Fig. 4-7.

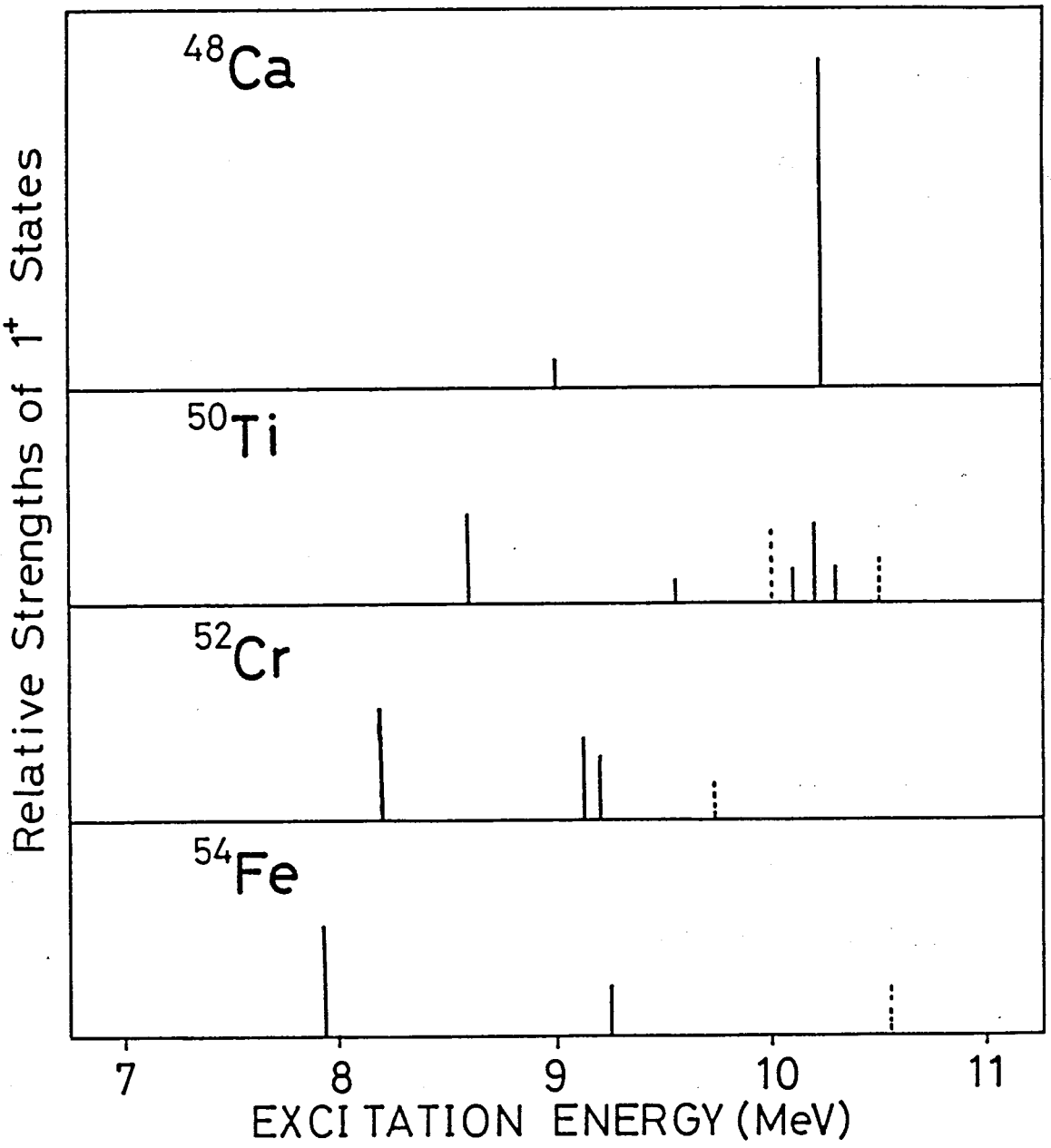
^{48}Ca
^{50}Ti
^{52}Cr
^{54}Fe
Relative Strengths of 1^+ States
7
8
9
10
11
EXCITATION ENERGY (MeV)

Fig. 4-8.

Chapter 5

Summary and Concluding Remarks

As was presented in the previous chapters, the whole system of the spectrograph has now attained the possibility of achieving high resolution nuclear study for various reactions.

Using the operational parameters determined by the experimental ray tracing of Chapter 2, the kinematic broadening effect has been corrected in the range of $0.0 \geq K_1 \geq -0.1$. In order to compensate the kinematic broadening effect, it was necessary to adjust not only the quadrupole component of the multipole magnet for the 1-st order compensation, but also to adjust sextupole and higher order components of the multipole magnet depending on the kinematic condition of the objective reaction. This is especially important for a spectrograph with a large horizontal acceptance angle like our case of spectrograph "RAIDEN". In the region of K_1 value mentioned above, the broadening effects proportional to K_1^2 or K_2^θ were fairly small and changing the strengths of multipole components as a linear function of K_1 was effective for the compensation of the kinematic broadening in the horizontal direction.

On the other hand for the particles with a large vertical inclination angle ϕ, the broadening effect by the vertical kinematic aberration was a serious problem. In the present system it was rather difficult to compensate this

aberration completely by the ion optical way. A practical way for the compensation was to measure the image at the focal plane in two dimensions. Under the condition of non-zero value of vertical convergence coefficient $(y|\phi)$ and/or $(y|\delta\phi)$, the image combined with the vertical aberration proportional to ϕ^2 showed a shape like crescent and this shape could easily be made straight with a software by re-analyzing the two dimensional data of the particles recorded event by event.

In order to put the advantages of the spectrograph to a good use, many properties have been required for the data acquisition system especially for the focal line counter. It should be long enough to cover the long focal line of a large dispersion spectrograph. The resolution should be good enough even for the non-normal incident of the lightly ionizing particles. It should endure the high counting rate and yet the structure and the associated electronics should be simple enough.

As an answer to these requirements, gas proportional counters with induction readout have been constructed. In this type of counters, position informations are obtained by the change division method using induced signals on resistive electrodes palced near anodes. By adjusting the resistivity of the induction electrodes, fast rise time of position information of less than 1 μs has been obtained for the counter of 1 m or more in its length. Fast position counters realized by the induction readout are able to endure the

total counting rate of up to 30 kHz without seriously affected by the pile-up effect. Usual deterioration of resolution for the lightly ionizing particles of non-normal incidence is minimized by the use of multi-anode design. In this structure several anodes are designed to subdivide the depth of the counter volume and as a whole, anodes are expected to work as a stack of thin counters.

In the two dimensional version of the induction readout counter, principle of drift counter has been used for the measurement of vertical incidence positions of particles. Since the non-resistive anodes produce fast signal with rise time of less than 20 ns, sufficiently good resolution of less than 1 mm is obtainable by measuring the time difference between this signal and the fast pulse from plastic E counter. As described in detail the two dimensional determination of position is powerful for the correction of kinematic aberration proportional to ϕ^2, which is quite difficult to compensate completely by the ion optical method alone. It is also powerful for the reduction of background. Since background particles are spreading widely in the two dimensional display, they can be discriminated from the normally scattered particles concentrating around the mediam plane.

Various high resolution experiments have been performed using the spectrograph and one of the attractive reactions is proton inelastic scattering. The reaction performed on ^{90}Zr discovered fairly large amount of hexadecapole strength

in the so called LEOR region and the reaction performed on ^{48}Ca revealed a strong unnatural parity 1^+ state. In both experiments, the high resolution spectra of around 15 keV was quite powerful in obtaining reliable angular distributions of the objective levels even in the region of high level density.

As presented "problems of software" for the better use of the spectrograph "RAIDEN" have been solved fairly well. At the same time, however, new problems became apparent in the process. Most important one is related with the kinematic broadening in vertical direction. In the present system the aberration was compensated using the two dimensional determination of the arrival position of the particles at the focal plane. This aberration, if possible, should better be compensated with an ion optical way. In that case data analysis may be far simplified. Two solutions may be possible. One is to restore a sextupole magnet just after the scattering chamber and seek a good combination of the excitation strengths of the sextupole magnet and the multipole magnet to erase the vertical as well as the horizontal aberration depending on the kinematical condition of the reaction. Since the sextupole magnet affects on both the horizontal and vertical ion optical properties of the spectrograph, best parameters which are determined for the multipole magnet should be modified depending on the kinematic coefficient K_2^{ϕ} . This way of correction, therefore, is very complicated to determine the best parameter.

Another clever way, if possible in the process of planning of a spectrograph, is to make a horizontal focussing point in addition to the vertical focussing point. At this place, ion optical properties in vertical direction is selectively modified and vertical and horizontal kinematic broadening effects may be corrected rather separately.

An improvement of the counter system depends on whether or not it is possible to make a long and high resolution focal plane detector which endures higher counting rate. In the present counter increasing length means increasing counter volume and therefore increasing counting rate. Since the rise time of the position pulse is limited by the property of the resistive electrode in the change division method, it seems to be difficult to make a faster counter system than the present value of around 0.5 μs. One of the good solution is to subdivide the counter volume and the ultimate form of this way of solution is a multi-wire proportional counter. At present, however, multi-wire proportional counter and the associated electronics including data taking system are far more complicated than those of the present counter system and are not reliable enough to cover a long focal line exceeding 1.5 m.

With these in mind better solution should be sought for a better experimental data taking to be accomplished. And I do hope that the answers to the "problems of software" presented here make a first step for the "achievement of high resolution nuclear study using a magnetic spectrograph system".

Acknowledgements

At this plane I would like to thank everybody who has been involved in the work described in this thesis.

The basic design and construction of the spectrograph "RAIDEN" was performed by Prof. H. Ikegami, Prof. S. Morinobu, Dr. I. Katayama and Dr. M. Fujiwara. Tedious and consuming data taking of the experimental ray trace was performed with the co-operation of Prof. H. Ikegami, Prof. T. Yamazaki, Prof. S. Morinobu, Dr. M. Fujiwara, Dr. I. Katayama and Dr. S. Imanishi. About the way of ray trace, discussions with Prof. S. Morinobu, Drs. M. Fujiwara and I. Katayama were quite fruitful. Encouragement of Prof. H. Ikegami is heartly acknowleged.

The focal plane counter system described here was constructed in co-operation with Mr. K. Nagayama who skillfully made the subtle part of the wire counters. Discussions with Dr. K. Iwatani of Hiroshima University, Prof. S. Morinobu and Dr. M. Fujiwara are heartly acknowledged. Beam test of the counter system was performed in co-operation with Profs. H. Ikegami, T. Yamazaki, S. Morinobu, Drs. M. Fujiwara and I. Katayama. The online data taking program for the spectrum was performed by Prof. T. Yamazaki, Dr. I. Katayama and Dr. N. Koori (Kyushu Univ.). In the preparation of data taking program for the two dimensional counter, I would like to thank Mr. M. Noumachi and Prof. H. Ogata for their kind help. Off-line two dimensional data analysis was performed using a program based on that written by Dr. H. Sakai. I should thank him for his offer.

The $^{90}Zr(p,p')$ and $^{48}Ca(p,p')$ experiment was performed with Profs. H. Ikegami, S. Morinobu, T. Yamazaki, Drs. M. Fjuiwara, T. Itahashi, S. Imanishi and Prof. S.I. Hayakawa of Ashikaga Institute of Technology. I am indebted much to Mr. Sugai of the Institute for Nuclear Study, University of Tokyo for preparing the self-supporting ^{48}Ca target. Thanks are extended to research program committee of RCNP, who permitted the use of machine time for these experiments.

Without the joint effort of the cyclotron operation group and the technical staff of RCNP this work would have been impossible. I am grateful for the work done by all these people.

I want to express my sincere thanks to my promoter Prof. H. Ikegami for the suggestions of the topic of this thesis. Encouragement of the late Professor S. Yamabe and director M. Kondo of RCNP is heartly acknowledged. Thanks are extended to Misses. S. Mizushima, M. Tado and K. Nagatani for the elaborate typewriting.

Finally I wish to express my thanks once more, also to all those who have not been explicitly mentioned.

April 1982